

Statistical Atlases of Cardiac Motion and Deformation  
for the Characterization of CRT Responders

Nicolas Duchateau

TESIS DOCTORAL UPF / 2012

Thesis submitted in partial fulfillment of the requirements  
for the degree of Doctor of Philosophy.



Departament de Tecnologies de la Informació i les Comunicacions  
Universitat Pompeu Fabra

Cover design by the author.

ISBN Barcode generated from

[www.terryburton.co.uk/barcodewriter/generator](http://www.terryburton.co.uk/barcodewriter/generator)

Statistical Atlases of Cardiac Motion and Deformation for the Characterization of CRT  
Responders

ISBN: 978-84-615-5596-3

Copyright ©2012 Nicolas Duchateau, Barcelona, Spain.

All rights reserved. No part of this publication may be reproduced or transmitted in any form or by any means, electronic or mechanical, including photocopying, recording, or any information storage and retrieval system, without permission in writing from the copyright owner.

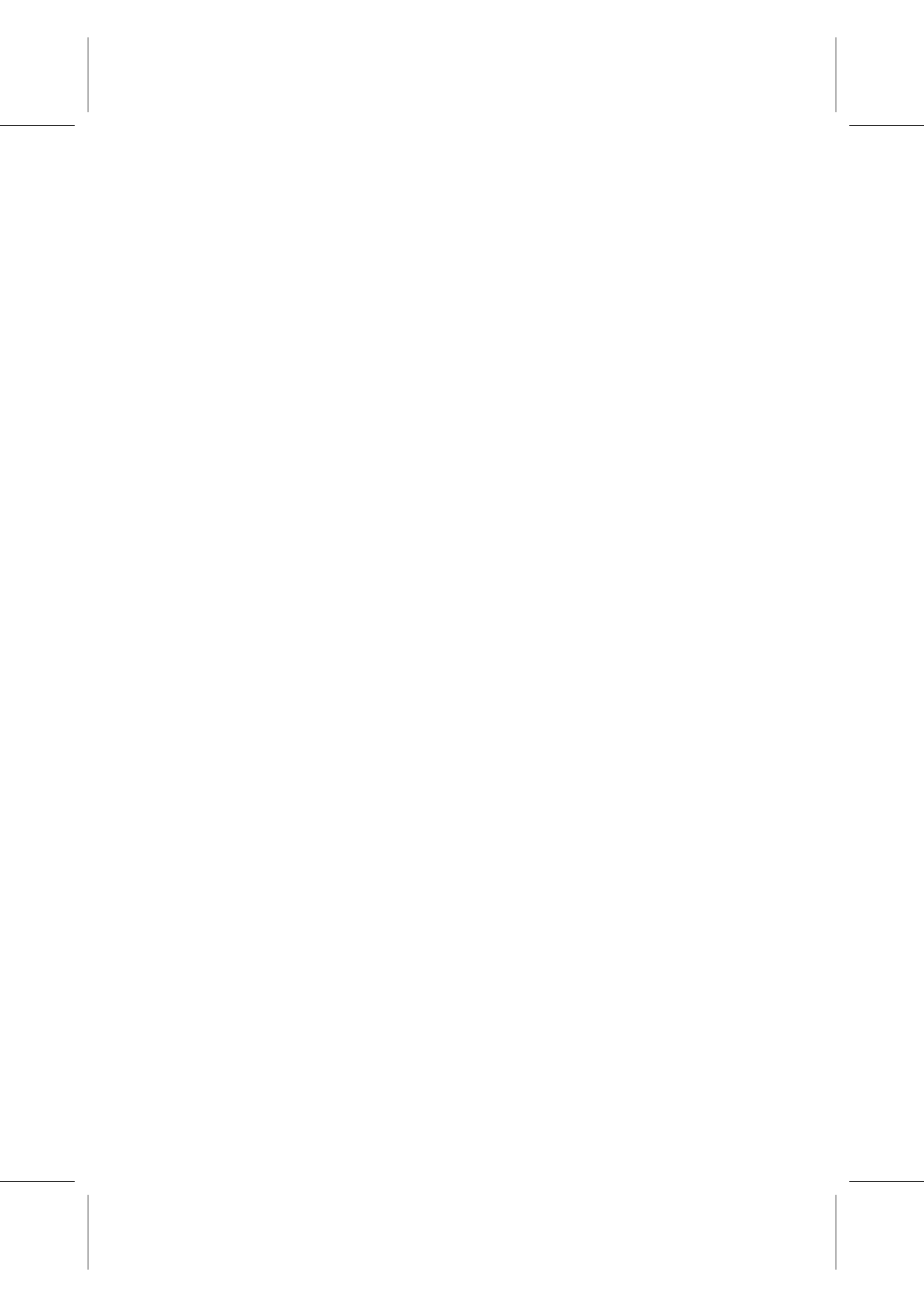
Director  
Prof. Alejandro F. Frangi    Associate Professor  
  Universitat Pompeu Fabra, Barcelona, Spain  
  Professor of Biomedical Image Computing  
  University of Sheffield, Sheffield, UK

Co-director  
Dr. Mathieu De Craene    Profesor Lector  
  Universitat Pompeu Fabra, Barcelona, Spain  
  Research Engineer  
  Philips Research, Medisys, Suresnes, France

Review Committee (Main):  
Prof. Xavier Pennec    INRIA Asclepios, Sophia Antipolis, France  
Prof. Vicent Caselles Costa    Universitat Pompeu Fabra, Barcelona, Spain  
Dr. Lluís Mont Girbau    Hospital Clínic, Universitat de Barcelona, Spain

Review Committee (Reserve):  
Prof. Philippe Salembier    Universitat Politècnica de Catalunya, Barcelona, Spain  
Dr. Josep Brugada Terradellas    Hospital Clínic, Universitat de Barcelona, Spain

This work was carried out in the Center for Computational Imaging and Simulation Technologies in Biomedicine (CISTIB), at the Departament de Tecnologies de la Informació i les Comunicacions at the Universitat Pompeu Fabra, Barcelona, Spain. This work was supported by the Spanish Industrial and Technological Development Center (cvREMOD CEN-20091044), the Spanish Ministry of Science and Innovation, Plan E and ERDF (STIMATH TIN2009-14536-C02-01), and the European Commission's Seventh Framework Program (euHeart FP7-ICT-224495).



*Aux gérards et aux gérardes.*



---

## Abstract / Resumen

*Abstract.* The definition of optimal selection criteria for maximizing the response rate to Cardiac Resynchronization Therapy (CRT) is still an issue under active debate. Recent clinical approaches propose a classification of patients into classes of mechanisms that could lead to heart failure and study their response to the therapy. In this line of research, the computation of a metric between the motion and deformation patterns of a given subject and well identified classes of CRT responders is considered in this thesis, as the basis of a new strategy to compute patient selection indexes. The thesis proposes first an improved design for the construction of statistical atlases of myocardial motion and deformation, and applies it to the characterization of populations of patients involved in CRT. The added-value of our approach is highlighted in a clinical study, applying the methodology to a large population of patients with a given pattern of dyssynchrony (septal flash) and understanding the link between its correction and CRT response. Finally, we propose a method to extend the analysis to the comparison of individuals to reference populations, either healthy or pathological, using manifold learning techniques to model a disease as progressive deviations from normality along a manifold structure, and demonstrate the potential of our method for inter-subject comparison in CRT patients.

*Resumen.* La definición de un criterio óptimo para mejorar la respuesta a la Terapia de Resincronización Cardíaca (TRC) sigue siendo un debate abierto. Estudios clínicos recientemente publicados proponen clasificar pacientes según diversos mecanismos patofisiológicos que pueden inducir insuficiencia cardíaca y estudian su respuesta a la terapia. Siguiendo esta línea de investigación, esta tesis considera el cálculo de una distancia entre los patrones de movimiento y deformación de un individuo y las clases de respondedores a la TRC, siendo la base de una nueva estrategia para calcular índices para seleccionar pacientes. Esta tesis presenta primero un método para construir un atlas estadístico de movimiento y deformación miocárdica, y su aplicación posterior a la caracterización de poblaciones de potenciales candidatos a la TRC. El valor añadido de nuestro método se enfatiza en un estudio clínico, en el cual se aplica la metodología a una gran población de pacientes con un patrón específico de disincronía cardíaca (llamado septal flash), y se relaciona su corrección y la respuesta a la TRC. Finalmente, se extiende el método para comparar individuos a una población de referencia, sana o patológica, usando técnicas de manifold learning para representar una patología como una desviación progresiva de la normalidad, con una estructura no lineal específica, y se demuestra el potencial de nuestro método para comparar entre si candidatos a la TRC.





---

# Contents

<b>Abstract / Resumen</b>	<b>i</b>
<b>Preface</b>	<b>xi</b>
<b>1 Introduction</b>	<b>1</b>
1.1 Preamble	1
1.1.1 Clinical context	1
1.1.2 Algorithmic implementation	1
1.1.3 Clinical application	2
1.2 Objectives of this thesis	3
1.3 Contributions of this thesis	3
1.4 Overview of this thesis	3
<b>2 State-of-the-art</b>	<b>5</b>
2.1 Looking for CRT responders	5
2.1.1 Cardiac dyssynchrony in the context of CRT	5
2.1.2 Understanding the mechanisms leading to cardiac dyssynchrony	6
2.2 Imaging strategies for analyzing myocardial dynamics	7
2.2.1 Myocardial imaging modalities	7
2.2.2 Image-based tracking	7
2.3 Statistical tools for inter-subject comparison	12
2.3.1 Computing statistics on motion and deformation fields	12
2.3.2 Where to compute statistics?	13
2.3.3 Which statistics? Local vs. global analysis	14
<b>3 A spatiotemporal statistical atlas of motion for the quantification of abnormalities in myocardial tissue velocities</b>	<b>17</b>
3.1 Introduction	18
3.1.1 Patient selection for CRT	18
3.1.2 Quantifying abnormality in cardiac motion	18
3.1.3 Proposed approach	19
3.2 Computation of myocardial velocities	20
3.2.1 Intra-series registration	20
3.2.2 Small displacement hypothesis and definition of velocities	20
3.2.3 Verifying the small displacements hypothesis on 2D US sequences	21
3.3 Construction of the Atlas	22
3.3.1 Temporal synchronization	22
3.3.2 Spatial normalization	23

3.3.3	Statistics on velocities . . . . .	25
3.4	Validation on 2D US image sequences . . . . .	26
3.4.1	Patient population and data acquisition . . . . .	27
3.4.2	Tools for visualizing spatiotemporal abnormalities . . . . .	28
3.4.3	Relevance of the atlas population . . . . .	28
3.4.4	Validation of the atlas construction steps . . . . .	30
3.5	Application to the analysis of the CRT population . . . . .	32
3.5.1	Localization of motion abnormalities . . . . .	34
3.5.2	Accuracy in the quantification of abnormalities . . . . .	36
3.5.3	How to differentiate between patterns? Added-value of spatiotemporal maps of motion abnormalities . . . . .	37
3.6	Discussion . . . . .	38
3.7	Conclusion . . . . .	39
<b>4</b>	<b>Atlas-based Quantification of Myocardial Motion Abnormalities: added-value for Understanding the effect of Cardiac Resynchronization Therapy</b>	<b>41</b>
4.1	Introduction . . . . .	42
4.2	Methods . . . . .	42
4.2.1	Patient population . . . . .	42
4.2.2	Definition of response . . . . .	43
4.2.3	Echocardiographic acquisition . . . . .	43
4.2.4	Automatic quantification of myocardial motion abnormalities . . . . .	43
4.2.5	Statistical analysis . . . . .	44
4.3	Results . . . . .	44
4.3.1	Patterns of motion abnormality at baseline . . . . .	44
4.3.2	Importance of the atlas spatiotemporal alignment . . . . .	45
4.3.3	Response to CRT . . . . .	46
4.3.4	Overall effects of CRT . . . . .	46
4.4	Discussion . . . . .	47
4.4.1	Abnormal patterns of septal motion and cardiac dyssynchrony . . . . .	47
4.4.2	Conventional methods for dyssynchrony assessment . . . . .	48
4.4.3	Added-value of atlas-based quantification of motion abnormalities . . . . .	48
4.4.4	Changes in LV dyssynchrony induced by CRT . . . . .	48
4.4.5	Other potential clinical applications of statistical atlases of motion to cardiac imaging . . . . .	49
4.5	Conclusion . . . . .	50
<b>5</b>	<b>Constrained manifold learning for the characterization of pathological deviations from normality</b>	<b>51</b>
5.1	Introduction . . . . .	52
5.1.1	Patient selection for CRT . . . . .	52
5.1.2	Robust comparison through statistical atlases . . . . .	52
5.1.3	Comparison to a given population . . . . .	53
5.1.4	Proposed approach . . . . .	54
5.2	Methods . . . . .	54
5.2.1	Atlas-based computation of myocardial motion abnormalities . . . . .	54
5.2.2	Definition of variables . . . . .	57
5.2.3	Manifold learning through Isomap . . . . .	58
5.2.4	Mapping new patients: from $\mathcal{A}$ to $\mathcal{C}$ . . . . .	58
5.2.5	Mapping new patients: from $\mathcal{C}$ to $\mathcal{A}$ . . . . .	61

5.2.6	Distance computation . . . . .	61
5.2.7	Additional metrics . . . . .	61
5.3	Experiments . . . . .	63
5.3.1	Parameter tuning - Synthetic data . . . . .	63
5.3.2	Parameter tuning - CRT data . . . . .	67
5.3.3	Patient analysis - CRT data . . . . .	74
5.3.4	Total distance to normality . . . . .	76
5.4	Discussion . . . . .	76
5.5	Conclusion . . . . .	78
<b>6</b>	<b>Conclusions</b>	<b>83</b>
6.1	Overview . . . . .	83
6.2	Outlook and future work . . . . .	83
	<b>Institutional context</b>	<b>xiii</b>
	<b>Publications</b>	<b>xv</b>
	<b>Curriculum Vitae</b>	<b>xvii</b>



---

## List of Figures

1.1	Research lines for this thesis . . . . .	4
2.1	Illustration of folding artifacts on large transforms . . . . .	10
2.2	Artifacts due to a non-diffeomorphic temporal image registration scheme . . . . .	12
2.3	Propagation of a synthetic grid using the TDFFD tracking . . . . .	13
2.4	Statistical artifacts for the group of 2D rotations . . . . .	14
3.1	Distribution of the dissimilarity measure $d_{small}$ . . . . .	21
3.2	Temporal synchronization of two patients . . . . .	22
3.3	Illustration of the spatial reorientation at time $t$ . . . . .	23
3.4	Illustration of the drift correction on one cycle . . . . .	24
3.5	Illustration of the push-forward action on velocity fields . . . . .	25
3.6	Velocity field $\mathbf{v}^k$ over the anatomy of subject $k$ and after reorientation to the anatomy of subject $ref$ . . . . .	26
3.7	Local septal coordinates and septal segments . . . . .	27
3.8	Abnormality evolution against the size of the atlas population . . . . .	29
3.9	Effect of a lower frame rate on the $p$ -value maps . . . . .	31
3.10	Influence of the reference choice on the $p$ -value maps . . . . .	33
3.11	Repeatability in the normalization of velocities from four different acquisitions of the same subject . . . . .	34
3.12	Comparison of two CRT candidates with SF with respect to the atlas . . . . .	35
3.13	Comparison between regional $p$ -values and clinical diagnosis . . . . .	36
3.14	Motion abnormality maps and radial velocities for the set of CRT candidates . . . . .	37
3.15	Motion abnormality maps for the set of volunteers . . . . .	38
4.1	Pipeline for the atlas-based quantification of septal motion abnormalities . . . . .	44
4.2	Variety of the patterns observed on the motion abnormality maps . . . . .	45
4.3	Motion abnormality map without and with the atlas spatiotemporal synchronization . . . . .	45
4.4	Average abnormality map for responders and non-responders, at baseline and follow-up . . . . .	46
5.1	Illustration of the mean computation with respect to the manifold . . . . .	53
5.2	Comparison of diffeomorphic pairwise FFD and TDFFD . . . . .	55
5.3	Map of septal motion abnormalities during systole, for one CRT candidate with SF . . . . .	56
5.4	Abnormality maps for four different subjects . . . . .	56
5.5	Pipeline for the method presented in this paper . . . . .	57

5.6	Interpolation of a 1D synthetic dataset using inexact matching without and with constraint for the origin . . . . .	60
5.7	3D swiss roll and 2D random distribution of points used as 2D parametrization for its construction . . . . .	63
5.8	Influence of the number of $k$ -NN on the isomap output, for the 3D swiss roll data . . . . .	64
5.9	Influence of the number of $k$ -NN on the isomap output, for the 3D swiss roll data . . . . .	65
5.10	Influence of the number of $k$ -NN on the node flow, for the 3D swiss roll data . . . . .	65
5.11	Comparison of locally adjustable kernel and fixed bandwidth kernels in terms of interpolation error . . . . .	66
5.12	Histogram of the distribution of neighbourhood sizes for the 3D swiss roll dataset . . . . .	67
5.13	Evolution of the node flow distribution with the number of $k$ -NN . . . . .	68
5.14	Evolution of the isomap error with the dimensionality and the number of $k$ -NN, for the training set of CRT candidates with SF . . . . .	68
5.15	2D embedding of the manifold of SF $p$ -value maps according to its two first dimensions . . . . .	69
5.16	Histogram of the distribution of neighbourhood sizes for the training set of CRT candidates with SF . . . . .	70
5.17	Generalization ability in function of the weighting terms $\gamma_f$ and $\gamma_g$ . . . . .	71
5.18	Reconstruction of five patients from the training set of CRT candidates with SF . . . . .	71
5.19	Comparison between non-linear (ML) and linear (PCA) dimensionality reduction techniques . . . . .	72
5.20	Influence of the removal of one sample on the ability of the model to reconstruct the training set . . . . .	73
5.21	Comparison of three points generated from the model coordinates to the training set . . . . .	73
5.22	Progressive deviations from the map used as origin for normality along the two first principal directions of the manifold dataset . . . . .	74
5.23	Evolution of the distances $d_M$ and $d_P$ versus the size of the training population . . . . .	75
5.24	Subject ordering using $d_M$ and $d_P$ , or $d_M^*$ and $d_P^*$ . . . . .	76
5.25	Subject ordering according to the amount of total abnormality contained in each map and the total distance to normality . . . . .	80
5.26	Relationship between the total abnormality contained in each map and the proposed distances . . . . .	81
5.27	Example of two patients having the same amount of total abnormality but different patterns . . . . .	82

---

## List of Tables

3.1	Intra- and inter-sequence registration accuracy against the variability in manual delineation of the endocardial border . . . . .	29
3.2	Shapiro-Wilk and Lilliefors tests for the distribution of myocardial velocities .	30
4.1	Baseline characteristics of volunteers and CRT candidates . . . . .	43
4.2	Baseline characteristics of CRT candidates according to the response at follow-up . . . . .	47
4.3	Abnormality reduction according to the response at follow-up . . . . .	47





---

## Preface

These years as a PhD student would not have been achieved the same way without the support and the contribution of several people.

First, I would like to thank Alejandro Frangi, who made this research environment possible and advised me on a regular basis along the whole process of the PhD. Mathieu De Craene, apart from being a music fellow, supervised my day-to-day work from its early beginning. His commitment to my project and his research philosophy were fundamental, and I wish him good luck in his new adventure. I am also extremely grateful to my colleague Gemma Piella for having also *les mains dans le cambouis*, to my co-authors Etel Silva, Ada Doltra, Marta Sitges from the Hospital Clínic for their closeness, and to Bart Bijnens for his guidance within the world of CRT.

I am also very thankful to Prof. Xavier Pennec, Prof. Vicent Caselles, Dr. Lluís Mont, Prof. Philippe Salembier and Dr. Josep Brugada, who accepted to be members of the jury for this thesis despite their respective commitments.

Then to all my past and present colleagues at CISTIB, with who I had the chance to work with and who contributed to create a very friendly atmosphere, particularly in our office, or maybe it was just the air-conditioning. *Ánimo* to all the other students, who can see there is a light at the end of the tunnel.

Special thanks to all my friends, in Barcelona and some other places, for keeping my enthusiasm intact and sharing the fact there is a life after work. *Véri* special thanks to the Gérards, in particular Papa, Juanitos et Gérard, to which I should dedicate a song. *Chiara aussi qui comprendra tout ça*.

Finally, I am kindly thankful to Celeste, for thinking I am not so crazy, and to my parents who supported and encouraged me, not just through full bags of homegrown vegetables.



---

# Introduction

## 1.1 Preamble

Starting from (1) a concrete clinical problem, this thesis aimed at (2) designing novel algorithmic tools to understand this problem, and (3) showing these tools are clinically applicable on large datasets.

### 1.1.1 Clinical context

This thesis was oriented towards the implementation of computational tools to study cardiac dyssynchrony, facing the current limitations of Cardiac Resynchronization Therapy (CRT) [1] studies. As briefly reviewed in Sec. 2.1.1, the main current clinical challenge behind CRT is certainly the improvement of the patient selection process. Recent editorials and studies have debated on the importance of primarily understanding the physiological mechanisms of cardiac dyssynchrony, and as a first step, their quantification [2] [3] [4] (Sec. 2.1.2).

In this context, the design of quantitative tools for characterizing these mechanisms of cardiac dyssynchrony stood as one of the initial targets of this thesis. Section 2.2 reviews the literature about myocardial motion and deformation estimation, while Sec. 2.3 gives an overview of the different options available to perform intra- and inter-subject statistical comparison.

### 1.1.2 Algorithmic implementation

Motion and deformation were quantified in this thesis using dense registration algorithms. These algorithms were made compliant with specific constraints associated to the processing of cardiac sequences (preservation of the topology and orientation of the registered anatomical structures, spatiotemporal smoothness and regularization of the estimated transformations, Sec. 2.2.2).

Besides being able to measure myocardial motion and deformation in a similar manner, most CRT studies still lack of a clear system of coordinates to perform relevant inter-subject comparison. This point is relatively paradoxical, as one would expect a relevant quantitative comparison for any information extracted in a quantitative manner. In such studies, spatial synchronization of the data is limited to the definition specific observation points, which



are generally a limited set of observer-defined landmarks, or the cardiac segments defined according to the NYHA convention [5]. The definition of these points is highly subjective and patient-dependent, and therefore a potential factor of bias in the analysis. Temporal synchronization of the whole data is avoided in a large number of CRT studies by computing few representative values for the whole sequence (average value within a specific time interval, or single values such as time-to-peak or -onset measurements, all of them being highly controversial [6] [7]).

Thus, the core of this thesis was the design of a robust framework to perform subject comparison at a population scale and proposing technical solutions for the above-mentioned synchronization issues. Depending on the population of subject considered in the analysis, different solutions were found:

- We first proposed a complete pipeline for the construction of a statistical atlas of motion built from a healthy population, allowing the local quantification of myocardial motion abnormalities. In the context of CRT, we demonstrated the potential of this approach for the characterization of specific patterns of mechanical dyssynchrony, at baseline (Chap. 3); and as a first step towards the understanding of the link between these mechanisms and CRT response, looking at the evolution of these abnormalities with the therapy (Chap. 4).

- The tools used for statistically modelling the variability of healthy subjects may not be adequate if the strategy is extended to build an atlas for a population of patients with a specific pattern of dyssynchrony. Spatiotemporal variations of the studied pattern may bias the estimation of the local variability for this population, despite its synchronization to a common system of spatiotemporal coordinates. Thus, a second part of the thesis was centered on the inclusion of more complex statistics (manifold-learning techniques) to achieve the comparison of individuals to a population with a specific pattern, taking into account the topology of this pattern (Chap. 5).

### 1.1.3 Clinical application

In a clinical perspective, part of the thesis work focused on the value of our approach for the characterization of CRT responders. The use of image registration, statistical atlases and manifold learning may appear as a complex machinery, the utility of which should be clearly demonstrated. We therefore intended to demonstrate the usefulness of the proposed quantification and statistical characterization of motion and deformation abnormalities in its application to a large database of patients.

The first expected output from the implantation of a CRT device on one patient (getting closer to a synchronous contraction, Sec. 2.1.1) is easily transposable at the atlas output level (reducing the observed abnormalities). Part of the work performed in this thesis was centered on the analysis of these abnormalities. The analysis can be performed either locally, at each instant of the cardiac cycle and each location of the myocardial wall (Chap. 3 and 4), or globally, therefore focusing on the whole patterns of abnormality observed, when present (Chap. 5).

As suggested by the findings of [8], and encouraged by recent editorials [2] [3] [4], we centered our clinical analysis on specific patterns of dyssynchrony that may condition CRT response. Encouraging results confirmed the relevance of an atlas-based approach to quantify the effect of CRT on such abnormal patterns (Chap. 4). These observations encouraged the design of the latest part of the thesis work, which consisted in implementing manifold-learning techniques to represent a pathological pattern and perform population-wise comparison (Chap. 5).

## 1.2 Objectives of this thesis

The overall aim of this thesis was to propose technical solutions for the characterization of motion and deformation abnormalities. On the clinical side, the underlying objective was to apply these tools in the context of CRT, and demonstrate their added-value. Main requirements were:

- the **quantification** of motion and deformation for any subject.
- the definition of **statistical indexes** to characterize the degree of abnormality of each subject and its location.
- the design of statistical tools for the **analysis of patterns** of dyssynchrony, using the information provided by the estimated abnormalities indexes.

## 1.3 Contributions of this thesis

- One of the main contributions of this work consists in the computation of statistical indexes for the quantification of motion and deformation abnormalities (Chap. 3). The novelty of such indexes is that they intrinsically perform a comparison to normality. This concept is analogue to the learning process made by a clinical observer, namely characterizing pathological motion and deformation patterns in a patient using learnt patterns from healthy and pathological sequences as reference. In our case, the analysis is completely quantitative, as recommended by recent statements about the study of cardiac dyssynchrony [3] [4].

- With the use of statistical atlases to analyze populations, patient data is normalized to a common anatomical reference. The computation of statistical indexes is therefore automatic and more accurate than methods requiring input from clinical observers (Chap. 3).

- On a clinical side, the recognition of specific motion and deformation patterns may have better predicting capability of CRT response than the classical indexes of dyssynchrony used for CRT. This work attempted to demonstrate the added-value of the proposed statistical atlases tools for the understanding the effect of CRT on such abnormal patterns (Chap. 4).

- The atlas framework proposed in this thesis allows the representation of any subject by a map of local abnormalities. One part of this thesis focused on the advanced analysis of these maps, using manifold-learning techniques to represent a pathological pattern as a deviation from normality along a smooth manifold, and then comparing individuals to this pattern (Chap. 5). This concept is a first step towards the reproducible comparison of a new candidate to specific patterns of mechanical dyssynchrony that actively condition CRT response.

## 1.4 Overview of this thesis

The whole structure of the thesis is articulated around atlas-based techniques for inter-subject comparison, from the construction of a statistical atlas to the extension of its output under a manifold-learning perspective, and its application to the study of CRT response (Fig. 1.1). The core contents of this thesis are articulated in four chapters.

**Chapter 2** presents a review of the state-of-the-art for the most of the concepts studied in this thesis, therefore situating each specific part of the thesis within either the clinical or image analysis communities (or both).

**Chapter 3** describes a complete pipeline for the construction of a statistical atlas of motion built from a healthy population. The atlas is built in a three steps process: motion

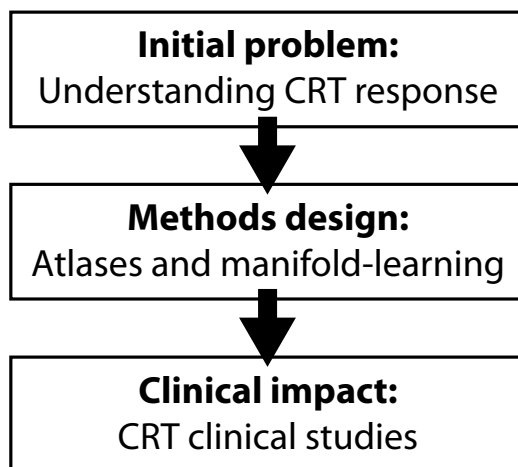


**Figure 1.1:** Research lines for this thesis.

extraction from cardiac sequences using image registration techniques, normalizing the different sequences to a spatiotemporal reference anatomy, and computing local statistics on motion fields. The atlas is then used for the comparison of individuals to a healthy population, both represented by myocardial velocities, using abnormality indexes available at any spatiotemporal location. The method is applied to the analysis of a population of CRT candidates with left ventricular dyssynchrony, looking for the presence of a specific pattern of intra-ventricular dyssynchrony called septal flash (SF).

**Chapter 4** consists in a clinical study to demonstrate the value of the proposed approach for the understanding the effect of CRT on patterns of abnormal motion. The method is applied to the computation of motion abnormalities in a large dataset of 88 CRT candidates before and after the therapy. The study focuses on the usefulness of the atlas-based tools to quantify motion abnormalities. The study highlights the importance of statistical indexes that intrinsically embed the notion of “normality”, to characterize patterns of mechanical dyssynchrony and their evolution with the therapy.

**Chapter 5** presents a new method for representing a pathological pattern as a deviation from normality along a smooth manifold, and comparing individuals to the population for which the manifold structure is estimated. Each subject is represented by a 2D map of local motion abnormalities, obtained from its comparison to a statistical atlas of motion constructed for a healthy population following the pipeline introduced in Chap. 3. The algorithm estimates a manifold from a set of patients with varying degrees of the same disease, and compares individuals to the training population using a mapping to the manifold and a distance to normality along the manifold. The method is applied in the context of CRT, comparing both healthy subjects and patients to a population with SF [8].

Each chapter is self-contained, and corresponds to a peer-reviewed journal article, published or under review. Some concepts may therefore be repeated, sometimes including some improvements introduced along the thesis progression.

---

## State-of-the-art

### 2.1 Looking for CRT responders

#### 2.1.1 Cardiac dyssynchrony in the context of CRT

The role of CRT [1] in improving both clinical condition and cardiac function of heart failure patients has been now clearly demonstrated [9] [10] [11].

In this therapy, a biventricular pacing device is positioned on the myocardium of the treated patients, to pace both the septal and lateral wall of the left ventricle (LV), and compensates deficiencies in the heart conduction system. The primary objective of CRT is to recover a synchronous contraction of the cardiac chambers. With optimized resynchronization, cardiac function is expected to improve, leading to notable improvements in patient condition (clinical response) and allowing reverse remodelling of the LV (volume or echocardiographic response) [12] [13].

Current CRT devices have two or three leads, depending on the pacing strategy. The septum is activated through a lead positioned in the right ventricle, while the lateral wall is paced at the coronary sinus level. A third lead may be placed in the right atrium to optimize the atrio-ventricular contraction. The accuracy of the pacing site and its influence on CRT response is discussed in [14] [1].

#### Importance of the patient selection process

Between 25 and 50 % of heart failure patients (at least 15 million people in Europe [15] [16]) may be candidates for CRT based on the current guidelines [16]. This high potential societal impact, combined to the high cost of the pacing device and the whole cardiac care cycle, makes the definition of relevant patient selection criteria a priority [17] [18] [13] [19].

Established international guidelines for the selection of patients currently select subjects with symptomatic heart failure, electrical abnormalities and decreased LV function (ejection fraction  $< 35\%$ , QRS duration  $> 120\text{ms}$ , and NYHA classification  $\geq 3$  despite optimal medical treatment) [20] [15].

However, with such selection criteria, the therapy fails to “improve enough” (Sec. 2.1.1) patient condition for approximately 30% of the subjects, and reverse remodelling for 50% of the patients [21]. The guidelines were softened according to these observations and clinical



practice [13], but making the patient selection more efficient remains an open issue. In a research perspective, improving patient selection supposes reaching a clear understanding of the physiological factors (both electrical and mechanical) that condition positive or negative response.

### Definition of CRT response

There is currently no consensus about the definition of CRT response [22] [7], even between two different papers from the same authors published in the same issue of the same journal [8] [23]. Studies generally define volume response by measuring reverse remodelling (reduction of LV end-systolic volume in a majority of studies), while clinical response is set by estimating the improvement of the patient condition (6 minutes walking test, NYHA functional class reduction, peak-oxygen consumption, etc.). The relevance of interpretations based on the clinical response may be discussed, due to non-negligible placebo effects [24].

In any case, the criteria for CRT response should be considered carefully [4] [21]. Indeed, the use of fixed thresholds for defining response is certainly a limitation to a clear understanding of CRT response, in comparison with the use of a spectrum of responses, involving additional measures of CRT outcome, as recently suggested [25] [18].

### 2.1.2 Understanding the mechanisms leading to cardiac dyssynchrony

There is still a huge paradox about CRT studies: CRT targets the correction of the dyssynchrony in the motion of the cardiac chambers, but the patient selection process still discards dyssynchrony (both electrical and mechanical [22]) as a selection criteria. The duration of the QRS complex is the only exception to this, but the guidelines have been revised to make its influence lower [13].

Regarding mechanical dyssynchrony, there is currently no consensus for its accurate characterization and its link with CRT response, therefore bringing no conclusions about the way to include it within the patient selection process [3] [4] [26] [27]. This low enthusiasm is reinforced by the abundance of publications about mechanical dyssynchrony measurements, including promising and extensively advertised, but deceiving, large-scale multi-center studies [28] [29] [30] [24].

The indexes proposed in the literature are mostly based on the direct comparisons of temporal measurements (QRS duration and time-to-peak or time-to-onset measures), which remain highly suboptimal [6] [7] and still discard the complexity of the etiologies of cardiac dyssynchrony. The combination of these single parameters into a multi-parametric analysis did neither bring any clear conclusions [31] [32] [33] for similar reasons.

Recent editorials encouraged rather different strategies, which privileged a mechanistic approach for the understanding of CRT response, rather than looking for a single or multiple phenomenologically predictive indexes [2] [3] [4]. The high predictive value associated to the correction of specific abnormal mechanisms, each one amenable to a certain type of dyssynchrony, was discussed in [8]. This study proposed a separation of patients according to specific groups of mechanical dyssynchrony (inter-, intra- and atrio-ventricular dyssynchrony), each of these groups being associated to one specific pathological pattern of myocardial motion and deformation, with different grades of abnormality with respect to a healthy cardiac function. Posterior works also considering similar patterns of mechanical dyssynchrony supported such a strategy [34] [35] [23].

According to this specific line of research, a straightforward improvement of the patient selection process for CRT could integrate the recognition of such patterns in new candidates,



under the condition that the response rate of each of these patterns is roughly known.

The algorithm for improving patient selection proposed in [8] is however an algorithmic model, the limitations of which should be carefully considered before adapting it. We summarized some of these points in Sec. 6.2, complemented by the critical view we gained about this strategy during the realization of this thesis.

## 2.2 Imaging strategies for analyzing myocardial dynamics

### 2.2.1 Myocardial imaging modalities

A large amount of imaging techniques are used in the clinical practice to analyze the dynamics of the myocardial wall, such as magnetic resonance imaging (MRI), tagged MRI (t-MRI), computed tomography (CT) and 2D/3D ultrasound (US), and techniques derived from US properties such as tissue doppler (TDI) and strain rate imaging (SRI). In MRI, t-MRI, CT and standard US imaging, wall motion and deformation can be obtained by using segmentation, tracking or registration techniques on image sequences. MRI and CT provide a better spatial resolution but a reduced temporal one compared to US imaging, which is in addition of easier access in hospitals, with less expensive and constraining devices (MRI for example cannot be used for patients equipped with pacemakers, due to the use of a high magnetic field). US and t-MRI allow a more accurate estimation of myocardial deformation due to the presence of local features on the myocardial wall (speckles [Sec. 2.2.2] or tags).

TDI and SRI provide complementary analyzing tools [36] [37]. Both use the Doppler effect on US signals to provide information regarding velocities (TDI, [38]) and strain (SRI, [39] [40]) along the myocardial wall. An up-to-date review on US-based techniques can be found in [36].

In this thesis, we tried to keep the formulation of the algorithms irrespective of the input imaging modality. We preferred to apply image processing techniques on standard sequences of images where the gray-level is directly related to the anatomy, rather than using functional images. Indeed, TDI only provides a 1D measurement (the projection of the velocity vector along the observation beam), namely limited information, and is highly dependent of the insonation angle [36]. SRI is still under development and needs to be improved for a completely reliable clinical use.

### 2.2.2 Image-based tracking

Recovering myocardial motion and strain has been targeted by a large number of computer-assisted techniques, which can be separated in three main trends: identifying anatomical features of the myocardial wall (using landmark extraction or image segmentation, based on Active Shape [41] and Appearance [42] [43] Models) (1) along the whole sequence, or on one frame of the sequence and propagate this information using (2) feature-tracking or (3) motion and deformation estimation directly from the image sequences, which is the strategy chosen for this thesis.

Image-based tracking techniques are not specific to a given imaging modality, but some popular exceptions were specifically designed for t-MRI and US, as reviewed in the following paragraphs.



## Frequency-based tracking of t-MRI sequences

Frequency-based methods can be used to track the information contained in t-MRI sequences, the main ones being HARP [44] [45], SinMod [46] and Gabor filter methods [47] [48]. All techniques are based on the principle that the phase of a material point is constant along the cardiac cycle. HARP works in the frequency domain to process phase information, phase shifts being associated to motion. SinMod improves the HARP technique by allowing the recovery of the both local spatial phase shift and spatial frequency of the tagged images, and not only local spatial phase. Gabor filters also allow tracking the anatomy from the phase response to the filter. A detailed review of these techniques can be found in [49].

## Speckle-tracking

Speckle tracking is a rather recent technique which uses block-matching algorithms to track local speckle patterns along US sequences. Speckle is a random interference pattern of US imaging which is mainly visible on the myocardial wall, and is conserved over “large enough” temporal neighborhoods of frames. Thus, tracking the local speckles allows tracking the myocardial wall along the whole sequence. In this sense, the concept of speckle tracking is very similar to the tracking achieved through image registration along cardiac sequences, with the specificity of computing image similarities locally. A majority of speckle tracking applications in clinical practice process 2D US [36] [50], but its extensions to 3D start gaining popularity as they do not suffer from out-of-plane motion artifacts [51] [52] [53] [54] [55] [56].

## Pairwise image registration

Basic registration takes as input two objects and computes an optimal transformation that matches one of these two objects to the second one. In our case the input objects are cardiac images and the expected outputs are displacement fields, reflecting inter-subject changes (in case the processed images come from two different subjects at the same phase of the cardiac cycle) or intra-subject changes, namely motion along the sequence. Due to the complexity of the way the heart moves and deforms, the computed transformations are required to be non-rigid.

Among the large variety of non-rigid registration techniques that have been developed, two can be said of very common use: demons algorithm, which is non-parametric [57], and Free Form Deformation (FFD) [58], which displaces a set of control points and therefore is parametric. For both techniques, matching mainly consists in the minimization of an energy including a similarity term between the images to match, and a constraint term on the transformation to control its smoothness.

Demons algorithm considers non-rigid registration as a diffusion process. It performs successive updates of a displacement field by adding a small vector field to it, whose expression is derived from optical flow equations. Smoothing by a Gaussian kernel serves as regularization technique. Detailed attempts to find a unified theory for demons-based algorithms can be found in [59] [60] [61] [62].

FFD settles a set of control points over the object to deform and moves them iteratively according to the optimization scheme. A major characteristic of this registration technique is that a whole continuous transformation can be characterized by a small number of parameters (the control points positions). The transform is then obtained over the whole image domain by interpolation on a B-spline basis [63] [64].

## Diffeomorphic registration

Tracking the anatomy implies imposing strong constraints on the estimated transformations: the topology and the orientation of anatomical structures should be preserved by the registration scheme. Indeed, in case of large displacements, simple registration schemes are likely to present folding artifacts [65], where image structures could overlap, appear or disappear, which is completely unrealistic in terms of anatomy. The previous registration schemes can therefore be adapted to provide diffeomorphic transformations (invertible, smooth and with smooth inverse) [66] [65].

*Intuitive construction of diffeomorphic transformations.* During the last decade, specific works took advantage of the definition of diffeomorphisms to provide optimal trajectories between two images parameterized by flows of velocities. We refer to these techniques as the Large Deformation Diffeomorphic Metric Mapping framework (LDDMM), initiated by the works of [67] and [68].

The intuition behind these works is directly linked to the group structure of the space of diffeomorphic transformation, the group operator being the composition operator [69]. A large diffeomorphic transformation is built as the composition of small transformations, computed during an iterative process. A parametrization of this composition process is generally defined as a time scale between times 0 and 1, which correspond to the fixed and moving images, respectively. For numerical solvers, the problem is formulated using a discretized time scale denoted  $\{t_i\}_{i \in [0, N]}$ , with  $t_0 = 0$  and  $t_N = 1$ . Thus, the composition process can be intuitively expressed as:

$$\varphi(\cdot, 1) = \circlearrowleft_{i=0}^{N-1} (\mathbf{Id} + \mathbf{v}(\cdot, t_i) \Delta t_i), \quad (2.1)$$

where each  $\mathbf{v}(\cdot, t_i)$  is a “smooth enough” vector field,  $\mathbf{Id}$  being the identity transformation,  $\Delta t_i = t_{i+1} - t_i$  is a “small enough” time interval, and  $\varphi(\cdot, t_i)$  is the diffeomorphic transformation built until time  $t_i$ , initialized with  $\varphi(\cdot, 0) = \mathbf{Id}$ .

The composition of the small transformations  $\{\mathbf{Id} + \mathbf{v}(\cdot, t_i) \Delta t_i\}_{i \in [0, N-1]}$  is more commonly written in an additive way, directly operating on the “small enough” vector fields  $\{\mathbf{v}(\cdot, t_i)\}_{i \in [0, N-1]}$ :

$$\varphi(\cdot, 1) = \varphi(\cdot, 0) + \sum_{i=0}^{N-1} \mathbf{v}(\varphi(\cdot, t_i), t_i) \Delta t_i, \quad (2.2)$$

The notion of “smooth enough” conditions the space in which the transformations are optimized, and should be defined before any computation. In practice, most of LDDMM algorithms reformulate the registration problem using reproducible kernel Hilbert spaces [70] [71] [69], which allow controlling the type of desired smoothness depending on the kernel expression and width [72].

The notion of “small enough” is related to the discretization of the time scale, as conditions the accuracy of replacing the composition of transforms (Eq. 2.1) by the addition of vector fields (Eq. 2.2). This last notion is easier to understand using a continuous formulation, as follows:

$$\varphi(\cdot, 1) = \varphi(\cdot, 0) + \int_0^1 \mathbf{v}(\varphi(\cdot, t), t) dt, \quad (2.3)$$

or its differential version:

$$\frac{\partial \varphi}{\partial t} \Big|_{(t=\tau)} = \mathbf{v}(\varphi(\cdot, \tau), \tau). \quad (2.4)$$

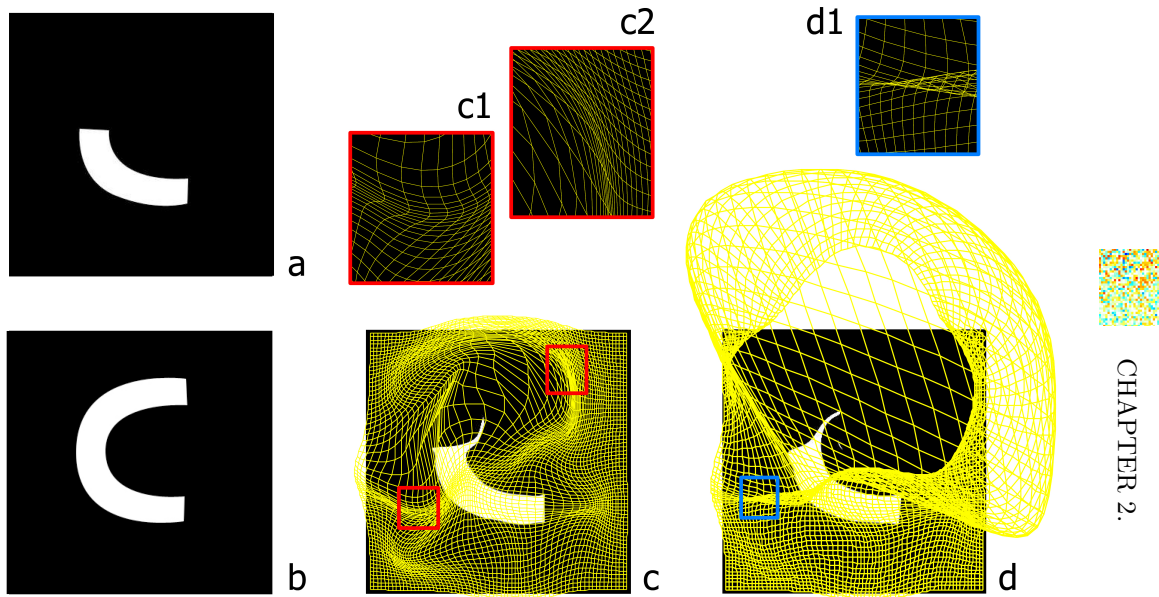


**Figure 2.1:** Illustration of folding artifacts on large transforms, with FFD as registration method. (a) fixed image, (b) moving image, (c) diffeomorphic transform, and (d) non-diffeomorphic transform.

The last formulation of Eq. 2.4 highlights the fact that  $\mathbf{v}(\varphi(\cdot, \tau), \tau)$  corresponds to the tangent of the trajectory at time  $\tau$ ,  $dt$  being an infinitesimal interval of the temporal scale. The discretized formulation of Eq. 2.2 is therefore valid only if the  $\{\Delta t_i\}_{i \in [0, N-1]}$  are “small enough”. Some considerations about the choice of the discretization interval can be found in [73].

The above-mentioned formulations underline the fact that the group of diffeomorphisms is of infinite dimension, as there is an infinity of velocity fields  $\mathbf{v}$  to define a path going from time 0 to time 1. Some variants of this problem have been proposed in the literature, restraining the search to a one-parameter subgroup of the group of diffeomorphisms by the use of stationary velocity fields [74] [75] [76] (Younes et al., 2009). This computational option may reduce the computational cost associated to the image registration process, but may present some limitations when the LDDMM framework is extended to perform image registration along temporal sequences (Sec. 2.2.2).

*Adapting classic registration algorithms to the diffeomorphic framework.* Aside the registration algorithms purely based on the LDDMM framework, the algorithms described in Sec. 2.2.2 were adapted to be diffeomorphic.

Diffeomorphic demons algorithm used a smoothing of the displacement field at each iteration to make the transformation invertible [77] [62].

In the FFD method, the displacement of control points is kept within a sphere of influence to prevent from folding artifacts [78]. An illustration of non-diffeomorphic and diffeomorphic FFD outputs is shown in Fig. 2.1.

### Anatomically consistent refinements of the registration scheme

Higher performance of the registration can be achieved through the addition of anatomically consistent constraints.

Increased flexibility and accuracy are obtained by making the registration multi-scale or a locally consistent definition of its parameters (adaptation of the FFD grid to the anatomical structures, as targeted in Thin-Plate Splines approaches [79] [80]). Multi-scale demons adapt the size of the smoothing kernel in the regularization process [81] [82], while in FFD the grid spacing is progressively reduced [83] [73]. Most of the algorithms derived from the LDDMM framework redefine the registration problem using reproducible kernel Hilbert spaces to reach smooth transformations and fast computations, which can therefore be made multi-scale by changing the kernel width, as discussed in [69] [84].

A second point would rather impose physically-consistent constraints on the computed transformations, as attempted for example in some works on incompressibility [85] [86] [87] [88] [89] [90] [91] [92] [73]. There is some controversy in the literature concerning the fully incompressible nature of the myocardial tissue, some elements being detailed in [73].

### Registration along temporal sequences

Image registration algorithms are generally pairwise. Their extension to align simultaneously all the images contained in one sequence allows the estimation of cardiac motion, as initiated in [93], and improved in [94] [95].

The formulation of the LDDMM registration between two images (Eq. 2.2 and 2.3) can be also slightly adapted to make the tracking along temporal image sequences diffeomorphic. First formulations only adapted the formulation of the image similarity to include the temporal dimension in the registration algorithm [96] [97] [98]. Temporal continuity of the trajectories is guaranteed, but the whole transformation is only piecewise diffeomorphic (between all instants at which image data exists). This means that the temporal continuity of the recovered velocities is not necessarily guaranteed, which could be a strong limitation to the construction of a statistical atlas of motion, where the velocity data is required at each instant of the continuous timescale.

Recently proposed methods solve this problem, using trajectory interpolation in a second-order scheme [99] [100], or simply formulating the registration as a full 4D diffeomorphic problem [101] [73] [102] [103].

*Formulation.* In the following we denote  $\{t_i\}_{i \in [0, N]}$  the temporal instants at which image data is available,  $t_0$  and  $t_N$  being the beginning and the end of the image sequence.

The transformation from time  $t_0$  to time  $t_n$  can be therefore be written using a continuous time scale:

$$\forall n \in [0, N], \quad \varphi(\cdot, t_n) = \varphi(\cdot, t_0) + \int_{t_0}^{t_n} \mathbf{v}(\varphi(\cdot, t), t) dt, \quad (2.5)$$

or a discretized time scale:

$$\forall n \in [0, N], \quad \varphi(\cdot, t_n) = \varphi(\cdot, t_0) + \sum_{i=0}^{N-1} \mathbf{v}(\varphi(\cdot, t_i), t_i) \Delta t_i. \quad (2.6)$$

*Sequential or non-sequential similarity metric?* The choice of the image correspondence to include in the registration scheme highly conditions the registration performance, as discussed in [104]. The image similarity can be computed between pairs of consecutive images (with the risk of presenting drift artifacts when chaining all the transformations along the sequence) [83], between each frame and one relevant reference chosen within the sequence [101] [73] [102] [103], or a combination of both [104] (Fig. 2.3).

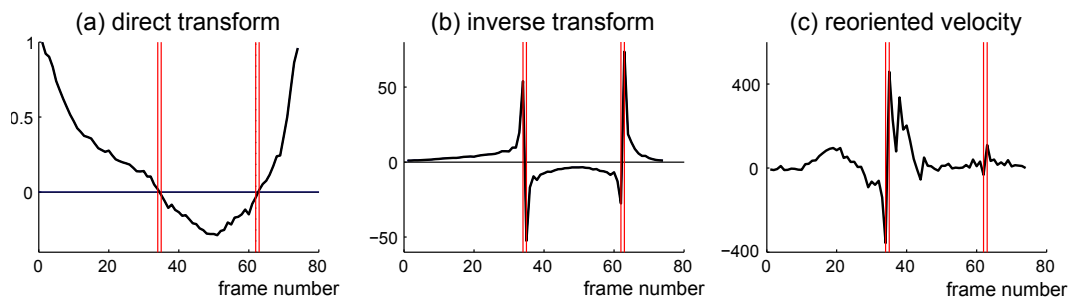


**Figure 2.2:** Artifacts due to a non-diffeomorphic temporal image registration scheme. (a) Determinant of the jacobian of the mapping from time  $t_0$  to time  $t_n$ ,  $n \in [0, N]$ . (b) Determinant of its inverse, which is involved in reorienting features to a reference anatomy. (c) Longitudinal component of the velocity, after reorientation to the reference anatomy. Artifacts are present when the jacobian is no longer invertible (vertical red lines).

*Computation of velocities.* The computation of velocities is not straightforward for the registration schemes not issued from the LDDMM framework. They often require the additional assumptions such as the stationarity of the velocities between each pair of consecutive frames [83], or advanced interpolation techniques to guarantee the velocities are differentiable [99] [100].

In contrast, the formulation derived from the LDDMM framework immediately provides an exact expression for the velocities by Eq. 2.4.

## 2.3 Statistical tools for inter-subject comparison

Methods derived from recent advances in computational anatomy [105] [106] [107], computational functional anatomy [108], and statistical atlases [109] [110], are particularly of interest for performing inter-subject comparison in our application. The data of each subject (shape or information defined at each point of this shape) is synchronized to a common anatomical reference, so that there is no need to define specific comparison points between patients. It consists in a robust alternative to the methods used in current clinical studies, which suffer of low reproducibility, as discussed in [3] [4].

Issues related to the integration of the temporal dimension contained in the cardiac sequences should be integrated in our analysis. This mainly differs from neuroimaging applications, which represent a majority of the computational anatomy applications. For these studies, temporal dimension of the data stands for longitudinal studies, making the challenges related to its integration different from cardiac studies: focus on growth processes, with few temporal samples for each subject, while studying cardiac function supposes looking at cyclic information with much more temporal samples for each subject (from 20 to 60 images per cycle in US sequences). Note that longitudinal studies also exist in cardiac applications, when looking at the evolution of the cardiac function of one subject before and after the therapy.

### 2.3.1 Computing statistics on motion and deformation fields

A majority of computational anatomy approaches directly compute statistics on shape, which has the advantage of allowing the use of Riemannian metrics. In the scope of this thesis, we aim at characterizing specific aspects of the cardiac function, namely motion and

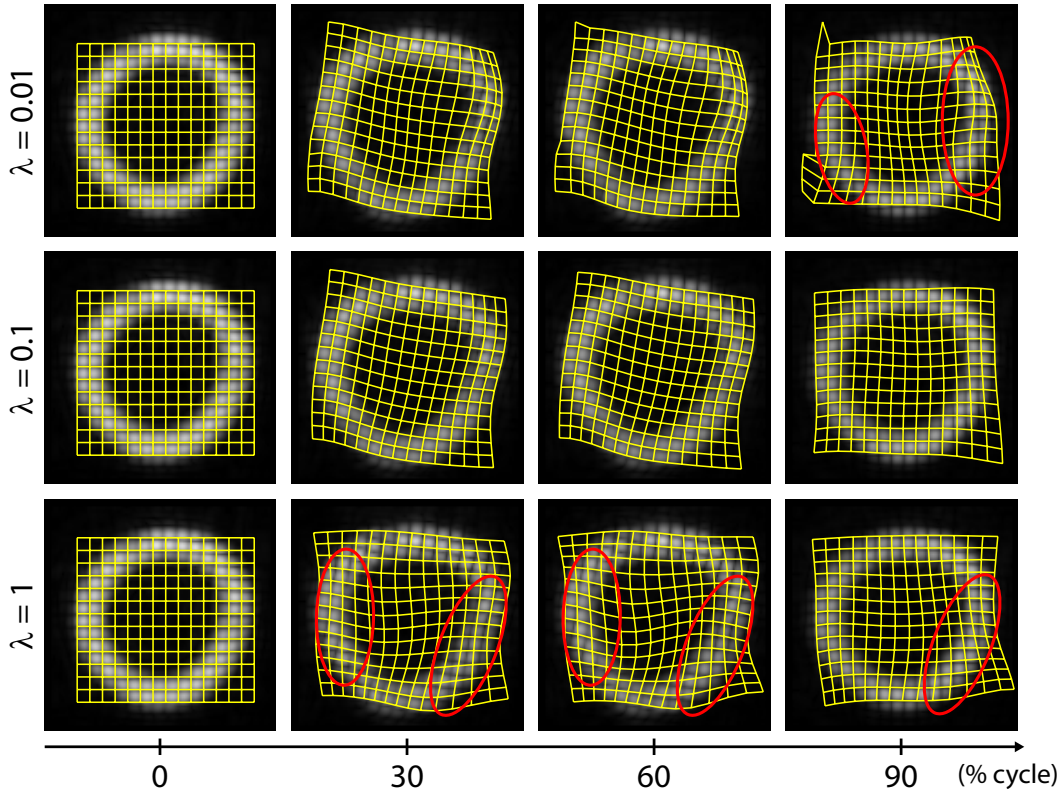


**Figure 2.3:** Propagation of a synthetic grid using the TDDFD tracking. Results for three different weights  $\lambda$  of the image similarity metrics (comparison frame-to-frame and to the reference image). Drift errors (top row) and tag jumps (bottom row) are pointed out by the red ellipses. Image taken from [104] with the permission of the authors.

deformation along the cardiac cycle, and we therefore process velocity and strain information, which is attached to the cardiac shape, therefore entering the field of computational functional anatomy [108]. In comparison with statistical atlases of shape, few works did the statistical analysis of the velocity and strain information attached to the myocardial shape [111] [112] [113], initiating the efforts on the statistical analysis of this information, and the preliminary steps to achieve it (transportation and reorientation).

In particular, the computation of statistics on diffeomorphic transformations, deformation fields or tensor fields requires some specific precautions, due to the fact that the space of diffeomorphisms only has a group structure for the composition operator [69], as illustrated in Fig. 2.4. Statistics compliant with the group of diffeomorphisms should be computed within its tangent space, as commented in [114] [74] [115] [116] [117].

### 2.3.2 Where to compute statistics?

The statistical analysis of velocity fields and strain fields can be performed either at each temporal instant, or at the time-point initiating the sequence. Both strategies have been adopted in the literature about statistical atlases built for longitudinal or temporal data, and correspond to the Eulerian or Lagrangian frameworks, respectively. Computations in an Eulerian system of coordinates [118] [98] [119] [120] raised the issue of estimating the

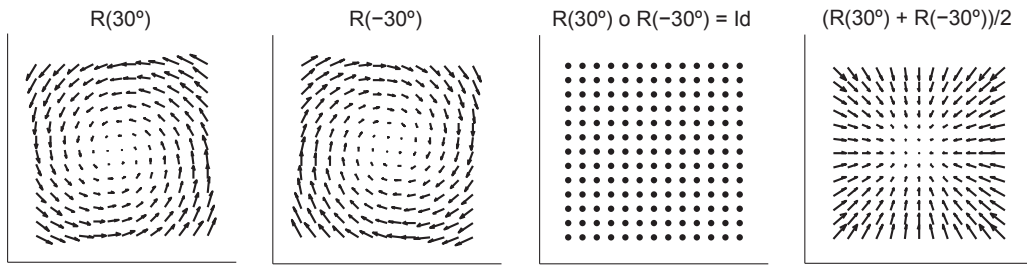


**Figure 2.4:** Statistical artifacts for the group of 2D rotations. From left to right: rotation of 30, -30, composition and sum of the related displacement fields. As for diffeomorphisms, these transformations belong to a group structure with the composition law as group action. Hence, classical statistics cannot be done directly on displacement fields but within the algebraic structure of the corresponding tangent space.



information at each desired temporal instant, using temporal neighborhoods or interpolation techniques, while computations in a Lagrangian system of coordinates [121] [97] [122] [123] [124] [125] suppose being able to transport the information along each sequence to have its definition at the reference time at which statistics are computed.

### 2.3.3 Which statistics? Local vs. global analysis

#### Statistical parametric mapping

The popularity of voxel-based image analysis methods has increased in the recent years for analyzing group-wise and inter-groups differences, and are generally referred to as statistical parametric mapping (SPM) techniques [126] [127] [128] [129] [130] [131] [132] [133]. When constructing a SPM, the information attached to the anatomy of each subject is mapped to a common template and voxel-wise statistics are used to compute local indexes characterizing the studied populations [134] [135] [136]. This means that the statistical analysis is performed locally, each voxel being considered independently from the others. This strategy is distinct from more conventional atlas studies, based on a global statistical analysis (such as principal component analysis [PCA]) or using localized kernels such as kernel-PCA or independent component analysis (ICA).

According to the objectives of this thesis, namely characterizing patterns of mechanical dyssynchrony, a global approach may discard the local aspect of the studied patterns, despite some efforts realized to highlight local information within a global analysis, as discussed in Sec. 2.3.3. For this reason, we initially used in this thesis SPM tools to perform the analysis (Chap. 3), which were adapted to handle multivariate data such as velocity and strain fields, similarly to the works that have been proposed for diffusion tensor fields [137] [138]. The limitations of local models are discussed in [139] [140] [141].

In these works and Chap. 3, the regional link between pixels was not taken into account. This link may come from to the input data (mechanical properties of the studied anatomy, regional noise patterns such as speckle) or algorithmic issues (image smoothing or spatiotemporal smoothness of the computed velocity and strain fields inherent to the registration algorithms used). Keeping a SPM approach, a regional correction could be used to compensate this voxel-wise dependence, as proposed in multiple comparison correction strategies. Voxel-wise observations can be considered as independent [142] [143] (the limitations of such a model being discussed in [144]), or dependent on a local neighborhood [126] [127] [128] [129] [130] [131] [132] [133].



## Advanced pattern analysis techniques

Specific dimensionality reduction techniques can be used to perform inter-subject comparison taking into account local spatiotemporal patterns that may present on each subject, and therefore overcoming some limitations of both voxel-based and basic global analysis.

The common link between these methods is the search for an optimal space to perform inter-subject comparison, in function of a primarily set criteria.

Characterizing the variability within a population can be achieved by multivariate techniques such as PCA, Canonical Correlation Analysis (CCA) and Multivariate Analysis of Variance (MANOVA), based on functional [145] [132] [146] and structural [147] data. Improvements of these techniques made the analysis more local (ICA [148] [149] [150] [151]), or respectful of the global structure of the data (non-linear methods such as kernel-PCA [152], principal geodesic analysis (PGA) [115], or manifold-learning techniques, initiated by the algorithms of [153] [154], which optimize geodesic distances along the manifold [Isomap [153]] or the local planarity of the estimated manifold [Laplacian eigenmaps [154]], respectively).

A well-documented review on multivariate techniques to find the optimal discrimination between groups of subjects was made by [155]. Classical multivariate analysis of data is achieved by linear discriminant analysis (LDA) [156], a special case of Canonical Correlation Analysis [157]. An article unifying the theory of multivariate analysis can be found in [158].

Advanced classification of subjects is achieved by pattern-recognition techniques [159] [160] [161] [162], support-vector machine (SVM) [163] [164] [165], Non-linear pattern classifiers [166] [167], and pattern-based morphometry [168], this non-exhaustive list being complemented in [155].

For the characterization of patterns of mechanical dyssynchrony, as targeted in this thesis, we decided to rely on non-linear techniques to overcome the limitation of a voxel-wise analysis, looking for adaptations of manifold-learning techniques to our problem. This allows subject comparison to a specific population, while modeling the non-linear structure of this reference population (Chap. 5).



CHAPTER 2.

---

## A spatiotemporal statistical atlas of motion for the quantification of abnormalities in myocardial tissue velocities

This chapter presents a new method for the automatic comparison of myocardial motion patterns and the characterization of their degree of abnormality, based on a statistical atlas of motion built from a reference healthy population. Our main contribution is the computation of atlas-based indexes that quantify the abnormality in the motion of a given subject against a reference population, at every location in time and space. The critical computational cost inherent to the construction of an atlas is highly reduced by the definition of myocardial velocities under a small displacements hypothesis. The indexes we propose are of notable interest for the assessment of anomalies in cardiac mobility and synchronicity when applied, for instance, to candidate selection for cardiac resynchronization therapy (CRT). We built an atlas of normality using 2D ultrasound cardiac sequences from 21 healthy volunteers, to which we compared 14 CRT candidates with left ventricular dyssynchrony (LVDYS). We illustrate the potential of our approach in characterizing septal flash, a specific motion pattern related to LVDYS and recently introduced as a very good predictor of response to CRT.

The content of this chapter is adapted from the following publication:

N. Duchateau, M. De Craene, G. Piella, E. Silva, A. Doltra, M. Sitges, B.H. Bijnens, and A.F. Frangi. A spatiotemporal statistical atlas of motion for the quantification of abnormal myocardial tissue velocities. *Medical Image Analysis*, 15:316-328, 2011.



## 3.1 Introduction

### 3.1.1 Patient selection for CRT

Cardiac resynchronization therapy (CRT) has proved its benefits over the last few years for the treatment of patients with heart failure and evidence of ventricular conduction delays [11]. The objective of CRT is to restore the coordination in the motion of the cardiac chambers, leading to notable improvements in cardiac function and reverse remodeling [12]. However, with current selection criteria, the therapy fails to improve patient condition for approximately 30% of the subjects [169]. The main current clinical challenge behind CRT is therefore the understanding of the physiological mechanisms conditioning positive or negative response.

In recent years, a large number of studies focused on the computation of quantitative indexes for cardiac dyssynchrony, with the underlying objective of predicting CRT response [22]. The indexes proposed in the literature are mostly based on direct comparisons of temporal measurements (QRS duration and “time-to-peak” measures) [170], but they remain suboptimal as discussed in [2] and [3] (poor reproducibility and over simplification of the complex mechanisms involved in CRT response to single observations of dyssynchrony). The lack of consensus about indexes able to accurately predict CRT response proves that generic indexes that try to capture dyssynchrony with limited reference to pathophysiology fail in the CRT context [3]. To fundamentally improve the prognostic value of novel indexes it is crucial that they are inspired in a deep understanding of the pathophysiological mechanisms involved in electrical and mechanical dyssynchrony. Recently, [8] proposed a classification of patients into specific etiologies of heart failure, and evaluated the response of each of these groups. Using this classification, one group showing a specific left ventricle (LV) dyssynchrony pattern called septal flash (SF) [23] demonstrated a very high response rate to CRT [8].

### 3.1.2 Quantifying abnormality in cardiac motion

The SF pattern has been characterized in [8] [23], using M-mode echocardiography. The protocol presented allows quantitative assessment of the SF (presence, timing and maximal excursion). More automatic methods focusing on abnormal patterns associated with dyssynchrony have also been proposed, using speckle tracking strain analysis from 2D ultrasound (2D US) [171], volume curves analysis from 3D US [172], and circumferential shortening indexes from tagged magnetic resonance (t-MRI) images [173]. However, for such methods, the analysis is only performed in a limited set of points that are observer-defined or only representative of specific heart segments. The definition of these points is therefore highly subjective and patient-dependent. Thus, the variability in their localization limits the relevance of defining statistical indexes at such locations. In methods derived from recent advances in computational anatomy [105], and particularly when using statistical atlases [110], patient data is normalized to a common anatomical reference, so that there is no need to define specific comparison points between patients. Such methods represent a promising alternative to compute relevant statistical indexes for the whole cardiac anatomy.

In our study, we aim at characterizing one aspect of the cardiac function, namely, motion throughout the heart cycle. Hence we rely on dynamic atlases, taking advantage of previous works on statistical atlases of motion and deformation initiated in [112], [111] and [113]. We can distinguish three steps in the process of building such a statistical atlas:

*Extracting motion from cardiac sequences.* [93] [174] [175]. In [96] and [176] [101] the tracking along longitudinal datasets is combined with the diffeomorphic framework [66], particularly suitable when handling cardiac sequences, since it preserves the topology and the orientation of anatomical structures.

*Normalizing the different sequences to a reference anatomy.* A pipeline adapted to cardiac studies was used in [177] and [178]. In [97] and [98], the synchronization of longitudinal datasets is combined with the use of diffeomorphic paths to compare the evolution of shapes along different sequences. These approaches still need to prove their feasibility (e.g. in terms of robustness and computational cost) when applied to real data, especially when the topology of the structure of interest is not preserved along the sequence, due to the presence of image artifacts, noise or the motion itself.

*Computing statistics on motion fields.* To preserve the diffeomorphic properties of the computed vector fields, the use of log-Euclidean metrics is recommended when computing statistics, as summarized in [117]. Abnormality assessment at every desired point of the anatomy requires the use of voxel-based morphometry tools (VBM) [135], for which an overview of some applications in brain morphometry can be found in [136]. Extending VBM tools to multivariate statistics [158] allows to handle statistics on vector fields, similarly to the works that have been proposed for tensor fields [137] [138].

### 3.1.3 Proposed approach

In this paper, we propose a complete and flexible pipeline for the construction of an atlas of motion based on these three construction steps, which were kept as simple as possible to minimize the computational burden. Thus, each of these steps can further be improved using a more elaborated technique, provided this guarantees a noticeable improvement in the identification of abnormal motion patterns.

Cardiac anatomy is tracked using the chaining of diffeomorphic paths between pairs of consecutive frames. We take advantage of the high temporal resolution of 2D US to work under a small displacements hypothesis. The use of small displacements reduces the computational complexity of estimating velocities over the whole continuous timescale, and allows direct computation of classical statistics on the velocity fields without the need of the log-Euclidean framework.

The atlas is then used for the comparison of individuals to a healthy population, both represented by myocardial velocities, using abnormality indexes available at any location  $(\mathbf{x}, t)$ . One interesting feature of such indexes is that they intrinsically perform a comparison to normality. This contrasts with the indexes generally used for CRT, which usually measure one clinical parameter, and subsequently compare the ranges obtained for populations of healthy and diseased subjects to define an optimal separation threshold.

The method is applied to the analysis of a population of CRT candidates with left ventricular dyssynchrony, looking for the presence of SF. A first preliminary version of this work was presented in [179], in which we illustrated the feasibility of such an approach for assessing abnormality on a reduced number of patients.



## 3.2 Computation of myocardial velocities

### 3.2.1 Intra-series registration

In the following sections we will denote  $\mathcal{S} = \{\mathbf{S}(t_0), \dots, \mathbf{S}(t_i), \dots, \mathbf{S}(t_{N-1})\}$  the temporal series of 2D images for one given patient, which contains  $N$  images taken at time-points  $t_i$ . To track the anatomy along cardiac cycles, pairwise registration between consecutive frames provides a sequence of transformations  $\varphi_{t_i, t_{i+1}} : \mathbf{x} \mapsto \mathbf{x}'$  for each series, which map any point  $\mathbf{x}$  of image  $\mathbf{S}(t_i)$  to its corresponding point  $\mathbf{x}'$  in the following frame  $\mathbf{S}(t_{i+1})$ . Our non-rigid registration uses the diffeomorphic free-form deformation (FFD) method [78], which is made multi-resolution to improve its robustness to the position and spacing of control points. We used spacings of 64, 32 and 16 mm, and mutual information as matching term. The L-BFGS-B algorithm [180] was chosen as optimizer for the registration procedure.

### 3.2.2 Small displacement hypothesis and definition of velocities

As explained in [74], a diffeomorphism can be represented as the flow of a stationary velocity field uniquely defined by its logarithm. In compliance with the registration scheme we use, velocities can be written as piecewise stationary, using:

$$\mathbf{v}(\varphi_{t_i, t}(\mathbf{x}), t) = \mathbf{v}(\mathbf{x}, t_i), \quad (3.1)$$

where  $t_i$  is the closest time-point that precedes  $t$  at which the series  $\mathcal{S}$  is defined, and  $\varphi_{t_i, t}(\mathbf{x})$  is the estimated position at time  $t$  of the anatomical point that was at  $\mathbf{x}$  at time  $t_i$ .

If the displacements are small, the logarithm of a transformation  $\log(\varphi_{t_i, t_{i+1}})$  can be approximated at the first order by its corresponding displacement field  $\varphi_{t_i, t_{i+1}} - \mathbf{I}$  (where  $\mathbf{I}$  is the identity). Velocities are directly obtained at the discrete time-points  $t_i$  where the data is defined using:

$$(t_{i+1} - t_i) \cdot \mathbf{v}(\cdot, t_i) = \log(\varphi_{t_i, t_{i+1}}) \quad (3.2)$$

$$\approx \varphi_{t_i, t_{i+1}} - \mathbf{I}. \quad (3.3)$$

These equations are coherent with the classical definition of velocities in mechanics, that is to say a displacement normalized by time.

The use of small displacements allows some additional simplifications in the computation of velocities at every time  $t$ , initially based on Eq. 3.1. First,  $\varphi_{t_i, t}$  can be estimated from  $\varphi_{t_i, t_{i+1}}$  using:

$$\varphi_{t_i, t} - \mathbf{I} \approx \frac{t - t_i}{t_{i+1} - t_i} \cdot (\varphi_{t_i, t_{i+1}} - \mathbf{I}). \quad (3.4)$$

In a similar way, its inverse can be written as:

$$\varphi_{t_i, t}^{-1} = \varphi_{t, t_i} \approx -\varphi_{t_i, t}. \quad (3.5)$$

This leads to the following simplified expressions for the velocities:

$$\mathbf{v}(\cdot, t) \approx \begin{cases} (\varphi_{t_i, t_{i+1}} - \mathbf{I}) / (t_{i+1} - t_i) & \text{if } t = t_i, \\ \mathbf{v}(-\varphi_{t_i, t}(\cdot), t_i) & \text{otherwise.} \end{cases} \quad (3.6)$$

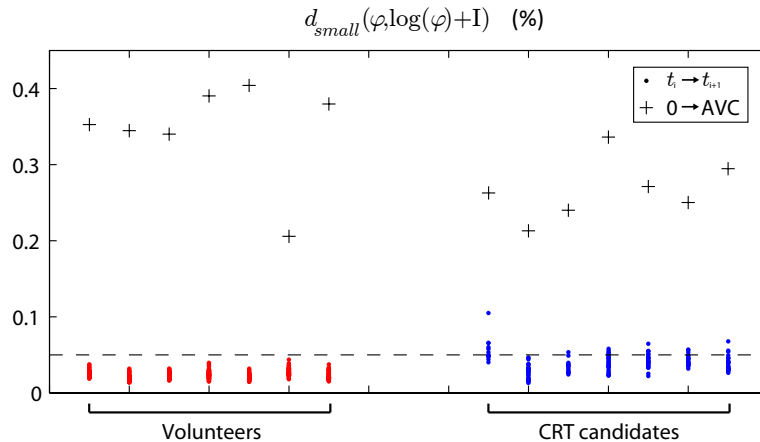


**Figure 3.1:** Distribution of the dissimilarity measure  $d_{small}$  for all the mappings between consecutive frames of seven volunteers and seven CRT candidates with SF (blue and red dots). The same distance was computed for the mapping between the initial frame in the cycle and the frame at aortic valve closure (AVC), which produces larger displacements (crosses).

### 3.2.3 Verifying the small displacements hypothesis on 2D US sequences

We can reasonably assume that the displacements between consecutive frames are small. Such a choice is justified by the good temporal resolution of 2D US imaging (around 60 frames/s [fps] for the healthy subjects and 30 fps for the CRT ones, details are in Sec. 3.4.1). We demonstrated the validity of this assumption by comparing the computed displacement fields to the logarithm of their relative transformations. We used

$$d_{small}(\varphi_1, \varphi_2) = \frac{1}{card(\Omega)} \cdot \sum_{\mathbf{x} \in \Omega} \frac{|\varphi_2 \circ \varphi_1^{-1} - \mathbf{I}|}{|\varphi_1 - \mathbf{I}|}(\mathbf{x})$$

as normalized dissimilarity measure between two transformations  $\varphi_1$  and  $\varphi_2$ , where  $\Omega$  is the image domain. Details about the computation of the logarithm and the inverse of the transformations  $\varphi_{t_i, t_{i+1}}$  are given in [74].

This comparison is illustrated in Fig. 3.1 for seven healthy volunteers and seven CRT candidates with SF. The computation involved all the frames contained into one cardiac cycle. The distance is computed for the mappings between consecutive frames (dots), showing there is on average less than 5% difference between the computed displacement fields and the logarithm of their relative transformations. This confirms that the displacements can be considered small, and that the velocities can therefore be computed using the simplified expression of Eq. 3.6. For comparison purposes, this computation was also carried out for the transformation mapping the initial frame in the cycle and the frame at end-systole (aortic valve closure event, defined in Sec. 3.3.1), resulting in larger displacements (crosses), and a distance  $d_{small}$  between 20 and 40%.

#### Small displacements and computational speed-up

The use of the small displacements hypothesis and the simplifications from Eq. 3.3, 3.4, and 3.5 allow much faster computations, which are particularly recommended in the context of building an atlas involving a large amount of data. Without the use of small displacements,

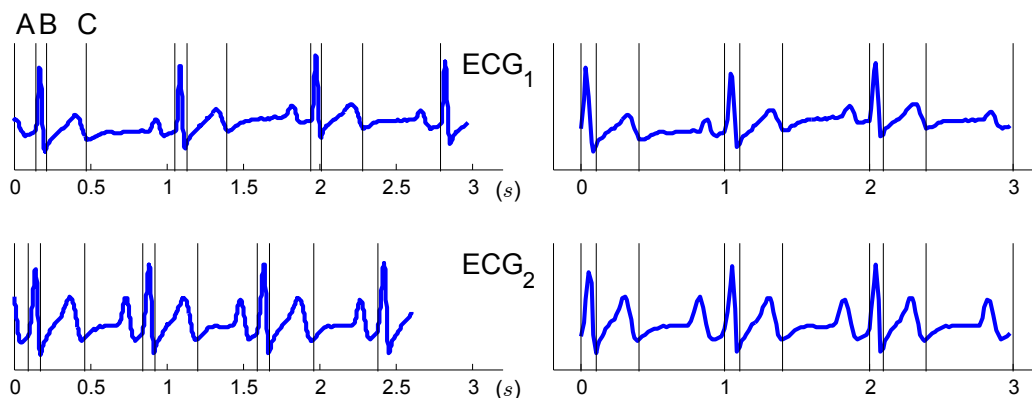


**Figure 3.2:** Temporal synchronization of two patients with different heart rates (71 bpm and 80 bpm, respectively), and different dynamics within their cardiac cycles (A: onset of QRS, B: aortic valve opening, C: aortic valve closure). Left: non-synchronized ECG, in seconds. Right: synchronized ECG, normalized timescale.

computing velocities at times  $t_i$  (Eq. 3.2) and  $t$  (Eq. 3.1) requires 50 and 15 seconds respectively, using a Intel Core i7 920 (2.66 GHz CPU, 6 GB RAM) computer. In comparison, the computational time is negligible when using the simplified expressions summarized in Eq. 3.6, since no logarithm nor inverse computation is required.

### 3.3 Construction of the Atlas

The registration steps previously explained provide velocity fields defined in the anatomy of each patient. Building an atlas requires bringing these fields to a common spatiotemporal coordinate system, so that a statistical representation of the data can be provided at every desired location  $(\mathbf{x}, t)$ .

In the following, we use  $k$  to refer to the  $k$ -th sample patient, and we index variable names accordingly.

#### 3.3.1 Temporal synchronization

The heart rate variability across patients changes the length of their respective cardiac cycles, as well as the synchronization of the different phases composing each cycle. Sequences may also differ in terms of trigger time and frame rate. Temporal synchronization will therefore consist in establishing correspondences between the cardiac events of the considered sequences and in bringing them to a normalized timescale.

Landmark-based piecewise linear warping is applied to the electrocardiogram (ECG) signals to map the sequences to a normalized timescale, as illustrated in Fig. 3.2. We use the following three landmarks:

- The *onset of the QRS complex*, which is located on the ECG using tools from the EchoPac software (GE Vingmed Ultrasound A.S., Horten, Norway).
- The *aortic valve opening (AVO)* and *closure (AVC)*, which are determined using continuous wave Doppler imaging on the aortic valve. AVO serves as a marker for the identification of the end of the isovolumic contraction (IVC) period, where SF is expected to be over.



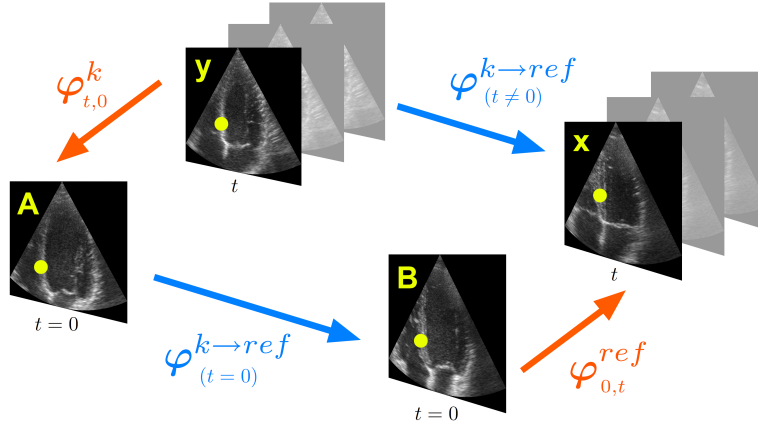


**Figure 3.3:** Illustration of the spatial reorientation at time  $t$ .

We used the absolute timing of ECG events proposed in the EchoPac software to locate these two events on the ECG associated to the studied sequence. This is done under the assumption that the timing between these events does not change between the sequences. This assumption is valid because the sequences have close heart rates, as they belong to the same session of acquisitions. In addition, in case of changes in heart rates, the diastolic period is mainly affected, while the timing of the events we chose is preserved as they belong to the systolic period.

Similar synchronization methods [177] identified a set of control points over sequences from MRI, but used image similarity. We preferred to rely on physiological information, as for US images the identification of these points using image data can be biased by respiratory or probe motion. In addition, the use of physiological events as temporal landmarks is believed to be more robust to pathology, as commented in [178].

### 3.3.2 Spatial normalization

Spatial normalization consists in reorienting the computed velocity fields  $\mathbf{v}^k(\mathbf{x}, t)$ , initially defined according to the anatomy of patient  $k$ , to a reference anatomy used for local statistical comparison. We chose a simple strategy for spatial reorientation, which is illustrated in Fig. 3.3. It consists of four consecutive stages: defining a reference anatomy for the atlas, estimating mappings between every patient and the atlas at time  $t = 0$  (by convention, time  $t = 0$  was defined as the onset of the QRS complex), chaining paths to compute these mappings at time  $t$ , and reorienting the velocity fields  $\mathbf{v}^k$  to the atlas anatomy at every time  $t$  using these inter-series mappings.

*Definition of a reference anatomy.* The importance of using an average anatomy as reference to limit statistical bias has been commented in some publications about atlas construction [181] [182] [183]. In the case of atlases of shape, the distance between the compared shapes is defined from the mappings between the patients and the atlas. In our case, these mappings only serve for reorientation purposes, and do not directly intervene in the computation of a distance between patients. We therefore preferred to choose one series as reference for the sake of simplicity.

The choice of a reference among the set of healthy volunteers was addressed using the group-wise normalized mutual information metric (GWNMI) proposed in [184], and criteria

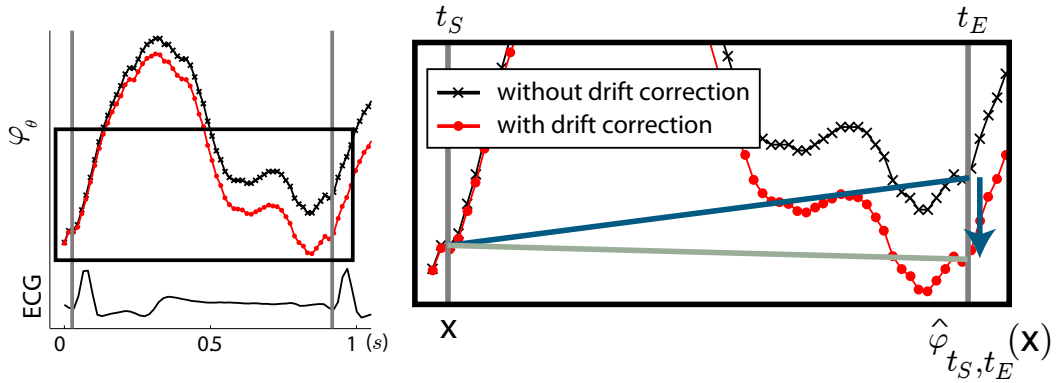


**Figure 3.4:** Illustration of the drift correction on one cycle. Black: tracking along the longitudinal direction without drift correction. Red: idem with drift correction.



based on image quality (LV fully visible along the whole sequence, and low heart rate to achieve a higher temporal resolution of the atlas). The influence of such a reference choice is discussed in Sec. 3.4.4, showing that the statistical bias it may introduce on the abnormality indexes remains small.

*Mapping patients to the atlas at  $t = 0$ .* For every patient  $k$ , we compute the transformation  $\varphi^{k \rightarrow \text{ref}}(0)$ , which maps the initial frame of this patient to the reference at time  $t = 0$ . This mapping is estimated using diffeomorphic FFDs as in Sec. 3.2.1.

Aside from speckle noise, the visible anatomy differs in each sequence because of intrinsic characteristics of each patient (heart size and shape) and extrinsic parameters due to the US acquisition (probe orientation and US window size adapted to see the whole LV). As a consequence, we made the FFD registration start from a bulk affine transform. This step models rough differences common to the whole sequence, namely the ones due to US acquisition parameters and heart size.

*Tracking the anatomy along sequences.* Chaining the pairwise transformations defined in Sec. 3.2.1 allows to track the anatomy of each patient along the sequence. We obtain the transformations  $\varphi_{0,t}^k$ , which map the anatomy between times  $t = 0$  and  $t$ .

When chaining transformations resulting from registrations of consecutive frames, small errors accumulate, manifesting themselves as net drifts observed in the final myocardial point positions when computing full trajectories. These artifacts can be removed by applying to each point of the trajectory a correction ensuring that:

$$\bigcirc_{t_S \leq t_i < t_E} \varphi_{t_i, t_{i+1}} = \hat{\varphi}_{t_S, t_E}.$$

Here,  $\bigcirc$  denotes the composition operator,  $t_S$  and  $t_E$  are the time-points starting two consecutive cardiac cycles, and  $\hat{\varphi}_{t_S, t_E}$  is the estimated transformation mapping frames at these time-points.

This correction is illustrated in Fig. 3.4. The transformation  $\hat{\varphi}_{t_S, t_E}$  is estimated using diffeomorphic FFDs as in Sec. 3.2.1, preceded by an affine registration step. It aims at taking into account probe motion during the acquisition, and adds robustness toward out-of-plane motion and filling variations between the different cardiac cycles, as the assumption

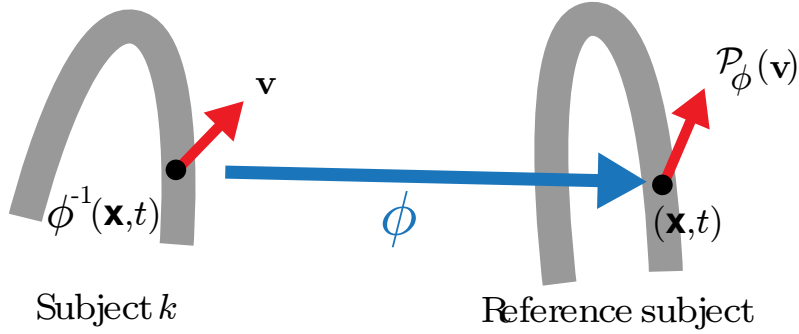


**Figure 3.5:** Illustration of the push-forward action on velocity fields at each location  $(\mathbf{x}, t)$

$\widehat{\varphi}_{t_S, t_E} = \mathbf{I}$  generally made in other works [93] does not hold true in our database of 2D US sequences.

*Mapping patients to the atlas at every time  $t$ .* We estimate the transformations  $\varphi^{k \rightarrow ref}$  at time  $t$  using the following chaining of transformations, which is illustrated in Fig. 3.3:

$$\varphi^{k \rightarrow ref}(t) = \varphi_{0,t}^{ref} \circ \varphi^{k \rightarrow ref}(0) \circ \varphi_{t,0}^k. \quad (3.7)$$

This strategy could later on be improved using the tools presented in [178], in terms of robustness in the estimation of  $\varphi^{k \rightarrow ref}$  at every time  $t$ .

*Reorientation to the reference.* Reorientation of the velocity fields  $\mathbf{v}^k$  is achieved at every point  $(\mathbf{x}, t)$  using a push-forward action on vector fields [185]:

$$\mathcal{P}_\phi(\mathbf{v}) = (\mathbf{D}\phi \circ \phi^{-1}) \cdot (\mathbf{v} \circ \phi^{-1}), \quad (3.8)$$

where  $\mathbf{v} = \mathbf{v}^k$ ,  $\phi = \varphi^{k \rightarrow ref}$  and  $\mathbf{D}$  is the Jacobian operator. In Eq. 3.8,  $\mathbf{D}\phi \circ \phi^{-1}$  represents the reorienting action on the vector fields moved to the new anatomical location by  $\mathbf{v} \circ \phi^{-1}$ .

Reorientation of vector fields is illustrated in Fig. 3.5 and Fig. 3.6, which display the velocity field of one healthy subject before reorientation, i.e. directly over the anatomy of this subject, and after reorientation to the reference anatomy.

### 3.3.3 Statistics on velocities

Velocities as defined in Sec. 3.2.2 belong to the tangent space of the group of diffeomorphisms. It means that because of the algebraic structure of the tangent space, classical statistics can be computed directly on the spatiotemporally normalized velocity fields, without the need of the log-Euclidean metrics described in [117].

We first compute their average and covariance to characterize the atlas population. Given  $K$  different sample series  $\{\mathcal{S}^k \mid k = 1 \dots K\}$ , we obtain at any desired point  $(\mathbf{x}, t)$  the average  $\bar{\mathbf{v}}$  and the covariance matrix  $\Sigma_{\mathbf{v}}$  from the set of velocities  $\mathbf{v}^k$ , defined as:

$$\bar{\mathbf{v}} = \frac{1}{K} \sum_{k=1}^K \mathbf{v}^k \quad \text{and} \quad \Sigma_{\mathbf{v}} = \frac{1}{K-1} \mathbf{V}^t \cdot \mathbf{V}$$

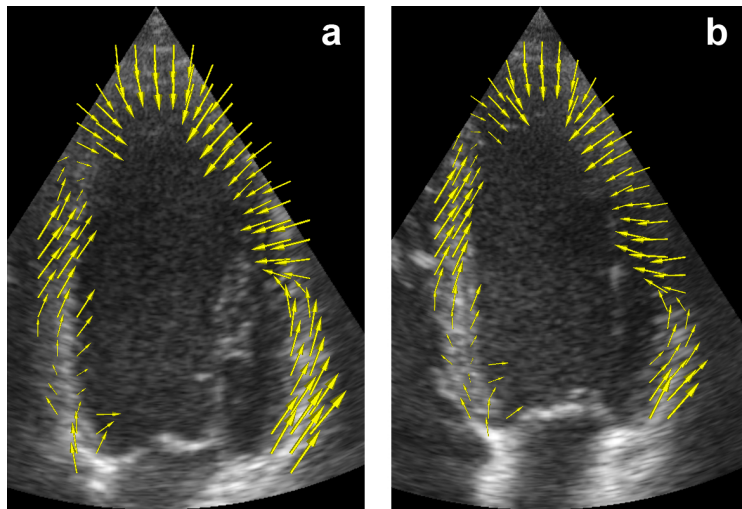


**Figure 3.6:** Velocity field  $\mathbf{v}^k$  over the anatomy of subject  $k$  (a) and after reorientation to the anatomy of subject  $ref$  (b). Images correspond to the LV region during systole. Arrows have been scaled for optimal visibility.

Here  $\mathbf{V}^t = [(\mathbf{v}^1 - \bar{\mathbf{v}}) | \dots | (\mathbf{v}^K - \bar{\mathbf{v}})]$  is the  $M \times K$  matrix whose columns are the centered velocity samples at  $(\mathbf{x}, t)$  and  $M$  is the dimensionality of the data. In our case,  $M = 2$  (2D US).

Then, we use the atlas for the comparison of the velocities of a given patient to the population used for its construction. We chose Hotelling's  $T$ -square statistic [186] to perform abnormality tests on multivariate data, which is equivalent to the Mahalanobis distance in the particular case where a single sample is compared to a population:

$$\tau^2 = \alpha (\mathbf{v} - \bar{\mathbf{v}})^t \cdot \Sigma_{\mathbf{v}}^{-1} \cdot (\mathbf{v} - \bar{\mathbf{v}}), \quad (3.9)$$

where  $\alpha = K/(K + 1)$ ,  $\mathbf{v}$  is the velocity to compare to the atlas, and  $\bar{\mathbf{v}}$  and  $\Sigma_{\mathbf{v}}$  are the previously described average and covariance matrix computed for the population atlas.

We use the  $p$ -value obtained from the Hotelling's  $T$ -test as quantitative index assessing abnormality. The  $p$ -value is computed from the cumulative function associated to the studied statistical distribution. This computation is performed under the assumption that the local distribution of myocardial velocities within the atlas population is Gaussian. This assumption is justified in Sec. 3.4.3. Leave-one-out cross-validation is used to compute the  $p$ -values within the atlas population.

In the following sections, we apply the previously described framework to build a statistical atlas of motion from a population of healthy subjects. We then use the atlas for the individual comparison of CRT candidates to the atlas population chosen as reference, using the tools described in Sec. 3.3.3.

### 3.4 Validation on 2D US image sequences

In this section, the atlas construction steps are validated in terms of registration accuracy and reproducibility of the spatiotemporal alignment scheme. Special attention is paid to the

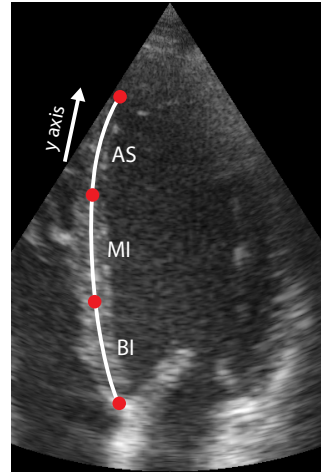
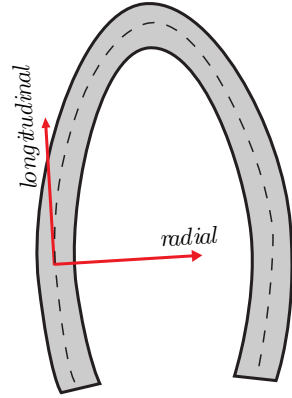


**Figure 3.7:** Left: Local representation of radial and longitudinal, defined as orthogonal and tangential to the septum medial line (dashed line), respectively. Right: Representation of the septal segments visible in the 4-chamber view (basal inferoseptal [BI], mid inferoseptal [MI], and apical septal [AS]) and used as vertical axis in the spatiotemporal maps of abnormality.

quality of the atlas population (number of subjects, statistical distribution, chosen reference, and temporal resolution compared to the population of CRT candidates).

### 3.4.1 Patient population and data acquisition

Two-dimensional echocardiographic image sequences were acquired in an apical 4-chamber view for two populations of subjects, using a GE Vivid 7 echographic system (GE Vingmed Ultrasound A.S., Horten, Norway). The choice of the apical 4-chamber view is led by the fact that it is the one used in clinical routine for the assessment of the fast SF pattern. The atlas of normal velocities was constructed from 21 healthy volunteers (age  $30 \pm 5$  years, 14 male). The patient population studied included 14 patients (age  $67 \pm 8$  years, 8 male) that were candidates for CRT based on current clinical guidelines (symptomatic heart failure with long QRS length and low ejection fraction) and that visually had abnormal septal motion on a transthoracic echocardiographic examination. The study protocol was approved by the Hospital Clínic (Barcelona, Spain) ethics committee and written informed consent was obtained from all patients.

Physiological differences between patients constrain the acquisition parameters, which will differ in terms of temporal resolution and image quality. Images were acquired during breath-hold to minimize the influence of respiratory motion. Resolution was optimized during the acquisition of healthy subjects' sequences, and corresponds to an average frame rate of 60 fps and a pixel size of  $0.24 \times 0.24 \text{ mm}^2$ . The CRT candidates involved in this study have dilated hearts compared to the healthy population. Thus, they require the use of a broader US sector so that the whole LV is still covered by the US beam. The temporal resolution of the sequences is thus lower for these patients due to this constraint (around half the frame rate). Their average pixel size is  $0.29 \times 0.29 \text{ mm}^2$ .



### 3.4.2 Tools for visualizing spatiotemporal abnormalities

The statistical tools described in Sec. 3.3.3 return a  $p$ -value index at every location  $(\mathbf{x}, t)$ , which can be visualized with the following tools, depending on the type of application targeted. Decoupling the spatial and temporal dimensions is particularly adapted for a precise localization of any motion abnormality (Sec. 3.5.1). In the following sections, another convenient mode of representation is used to visualize abnormalities in both spatiotemporal dimensions at the same time. In such maps, the horizontal axis represents time and the position in the septum (basal inferoseptal [BI], mid inferoseptal [MI], and apical septal [AS]) is used as vertical axis (right part of Fig. 3.7). The representation of the  $p$ -value in this space is similar to anatomical M-mode echocardiographic images, classically used to visualize wall motion over time. To highlight the inward and outward events of SF, in comparison with other patterns of abnormal motion of the septum (Sec. 3.5.3), the color-code used in these maps encodes the  $p$ -value in a logarithmic scale, multiplied by the sign of the radial velocity. Blue color represents highly abnormal inward motion of the septum, red color representing highly abnormal outward motion. The definition of local longitudinal and radial directions is illustrated in the left part of Fig. 3.7.

### 3.4.3 Relevance of the atlas population

The computation of a distance to normality assumes that the atlas population is representative of normality. In this study, the atlas population has non-dilated hearts, no cardiac dysfunction, and its baseline characteristics (QRS width, LV volumes and ejection fraction) match with the values found in the literature for a population of patients with normal cardiac function [187].

*Number of subjects.* To justify that the statistics are not biased due to the number of subjects in the atlas population ( $K = 21$ ), we computed the evolution of the motion abnormality index ( $p$ -value) for an atlas population made of  $K_s < K$  subjects. This experiment is summarized in Fig. 3.8, in which the indexes were computed for a reduced set of 14 CRT candidates at each spatiotemporal location  $(\mathbf{x}, t)$ . These values were normalized towards the value obtained for the largest atlas population, so that the evolution is represented in the same magnitude scale (%). The plot on the top represents this evolution for the three septal segments of one CRT candidate. For each value of  $K_s < K$ , the experiment was repeated for 100 random combinations of  $K_s$  subjects (vertical error bars). In each spatiotemporal region, the number of subjects above which this evolution stabilizes to its final value  $\pm 5\%$  is summarized in the table of Fig. 3.8 (average  $\pm$  standard deviation over the set of 14 CRT candidates). Based on these values, we can reasonably trust an atlas built with all the available healthy volunteers (21 subjects).

*Statistical distribution assumptions.* We computed the Shapiro-Wilk and the Lilliefors tests [188] [189] at each location  $(\mathbf{x}, t)$  to check the gaussianity of the local distribution of the atlas velocities, as assumed for the computation of local  $p$ -values. The results are summarized in Tab. 3.2, which shows the average values and standard deviation of these tests over the three septal segments, along each eigendirection of the velocity distribution, independently. The last line presents the values of these tests for the generation of 21 normally distributed random numbers, repeated 10000 times. Based on these values, we can reasonably consider that the distribution of velocities is Gaussian at each point  $(\mathbf{x}, t)$ .

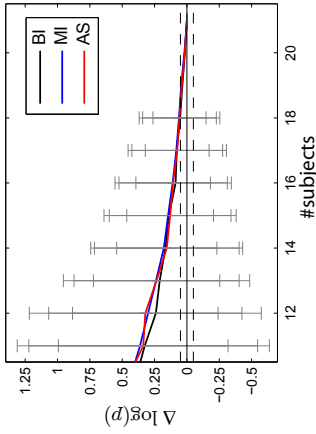


**Figure 3.8:** Left: Normalized evolution of the motion abnormality indexes of one CRT candidate, versus the size of the atlas population. Average over the cardiac cycle and the septal segments (basal inferoseptal [BI], mid inferoseptal [MI], and apical septal [AS]). Error bars represent the standard deviation over 100 random combinations of  $K_s < K$  subjects. These error bars are not displayed for  $K_s \geq 19$  as the number of random combinations (100) is of the same order of magnitude than the number of possible combinations between the atlas subjects. Right: Values above which this evolution stabilizes to its final value  $\pm 5\%$  (dashed line), per cardiac segment and temporal window of the cardiac cycle. Average  $\pm$  standard deviation values over the set of 14 CRT candidates.

Segment	IVC*	Systole\IVC†	Diastole
BI	$17.0 \pm 1.6$	$16.8 \pm 1.2$	$17.9 \pm 1.3$
MI	$16.7 \pm 1.0$	$17.1 \pm 1.5$	$18.0 \pm 1.1$
AS	$17.9 \pm 1.5$	$19.3 \pm 1.5$	$19.4 \pm 1.6$

\* Isovolumic contraction  
† Systole excluding the IVC period

Units (pixels)	Intra-sequence			Inter-sequence			Observers	
	AVO	VOL AVC	Q	AVO	VOL AVC	Q	$\delta_{intra}$	$\delta_{inter}$
BI	$5.7 \pm 1.8$	$10.9 \pm 5.4$	$5.0 \pm 3.5$	$5.1 \pm 1.9$	$7.2 \pm 3.6$	$5.6 \pm 2.8$	$2.7^*$	$6.9 \pm 3.0$
MI	$4.3 \pm 1.4$	$8.3 \pm 3.4$	$4.3 \pm 3.0$	$5.6 \pm 2.9$	$4.9 \pm 2.4$	$4.5 \pm 1.6$	$2.2^*$	$5.5 \pm 2.2$
AS	$6.7 \pm 3.6$	$9.1 \pm 3.9$	$5.4 \pm 2.8$	$7.0 \pm 3.1$	$7.4 \pm 3.2$	$6.6 \pm 3.1$	$2.9^*$	$8.5 \pm 4.2$

\* Carried out on one subject only

**Table 3.1:** Comparison of intra- and inter-sequence registration accuracy to the variability in manual delineation of the endocardial border. Intra-sequence: distance between shapes manually delineated at three instants of the cardiac cycle (AVO, AVC and onset of QRS for the subsequent cycle), and the shape delineated at the beginning of the cycle, propagated using the registration-based tracking along the sequence. Inter-sequence: distance between the shapes delineated at the onset of QRS of the studied cycle in each subject's anatomy, which were mapped to the reference, and the shape delineated in the reference anatomy. Results indicate the average  $\pm$  standard deviation in pixels over the whole set of volunteers and the whole set of CRT candidates, respectively. To get a range of comparison, the septum width at mid-inferoseptal level for the atlas reference anatomy is around 35 pixels.



(%)	Segment	SW	LF
$\mathbf{v}_1$	BI	$93.5 \pm 4.2$	$14.4 \pm 4.0$
	MI	$92.8 \pm 4.7$	$15.0 \pm 3.8$
	AS	$92.9 \pm 4.9$	$14.7 \pm 4.0$
$\mathbf{v}_2$	BI	$88.7 \pm 8.3$	$17.7 \pm 5.0$
	MI	$89.6 \pm 7.7$	$17.1 \pm 5.4$
	AS	$86.9 \pm 10.1$	$18.6 \pm 6.0$
randn(21, 10000)		$95.2 \pm 0.3$	$13.1 \pm 3.1$

**Table 3.2:** Shapiro-Wilk (SW) and Lilliefors (LF) tests for the distribution of myocardial velocities from 21 healthy volunteers, at each septal segment. The components of velocities along each eigendirection ( $\mathbf{v}_1$  and  $\mathbf{v}_2$ ) were treated independently. Bottom line: generation of 21 normally distributed random numbers, repeated 10000 times.

### 3.4.4 Validation of the atlas construction steps

#### Intra-sequence registration accuracy

We first evaluated the quality of our intra-sequence registration by comparing it to manual landmarking. Three observers manually segmented the endocardium border of the septal wall for the whole set of subjects (21 volunteers and 14 CRT candidates), at four temporal instants: onset of QRS, AVO, AVC and onset of QRS for the subsequent cycle. For each observer, the shape delineated at the first of these instants was then propagated along the whole cycle using the displacement fields computed by our registration algorithm. Finally, its position at the three remaining instants was compared to the delineation made by the observer at these instants. Intra- and inter-operator variability ( $\delta_{intra}$  and  $\delta_{inter}$ ) were computed at each of the four instants listed above. For the intra-operator variability, each observer repeated the manual delineation ten times for one healthy volunteer, while inter-operator variability was obtained by comparing the delineations made by the three observers, for the whole set of subjects. We used a point-to-line distance for the comparison of the delineated curves and the propagated ones (average over the points of each septal segment). Table 3.1 presents the distance between the automatically propagated shapes and the delineation made by the observers, and compares it to the intra- and inter-observer variability. The intra-sequence tracking showed a precision comparable to the observers variability for all the instants. Lower accuracy is observed near the apex, due to the lower quality of the US images in this region, as commented in the discussion section of this paper.

#### Inter-sequence registration accuracy

The accuracy of the inter-sequence registration was evaluated in a similar way to the experiment described in Sec. 3.4.4 for the intra-sequence registration. For each subject, the shape delineated in the initial frame of the cycle was mapped to the reference anatomy using the transformation estimated by the inter-sequence registration. Then, the distance between the mapped shape and the shape delineated in the reference anatomy was used as an estimator of the inter-sequence registration accuracy. The experiment showed that inter-sequence registration accuracy is comparable to the observers variability.

#### Influence of the temporal resolution

In principle, differences in the temporal resolution of the atlas population and the set of CRT candidates could introduce bias on the abnormality measured. The two following experiments illustrate the influence of different frame rates on the computation of the  $p$ -value maps.



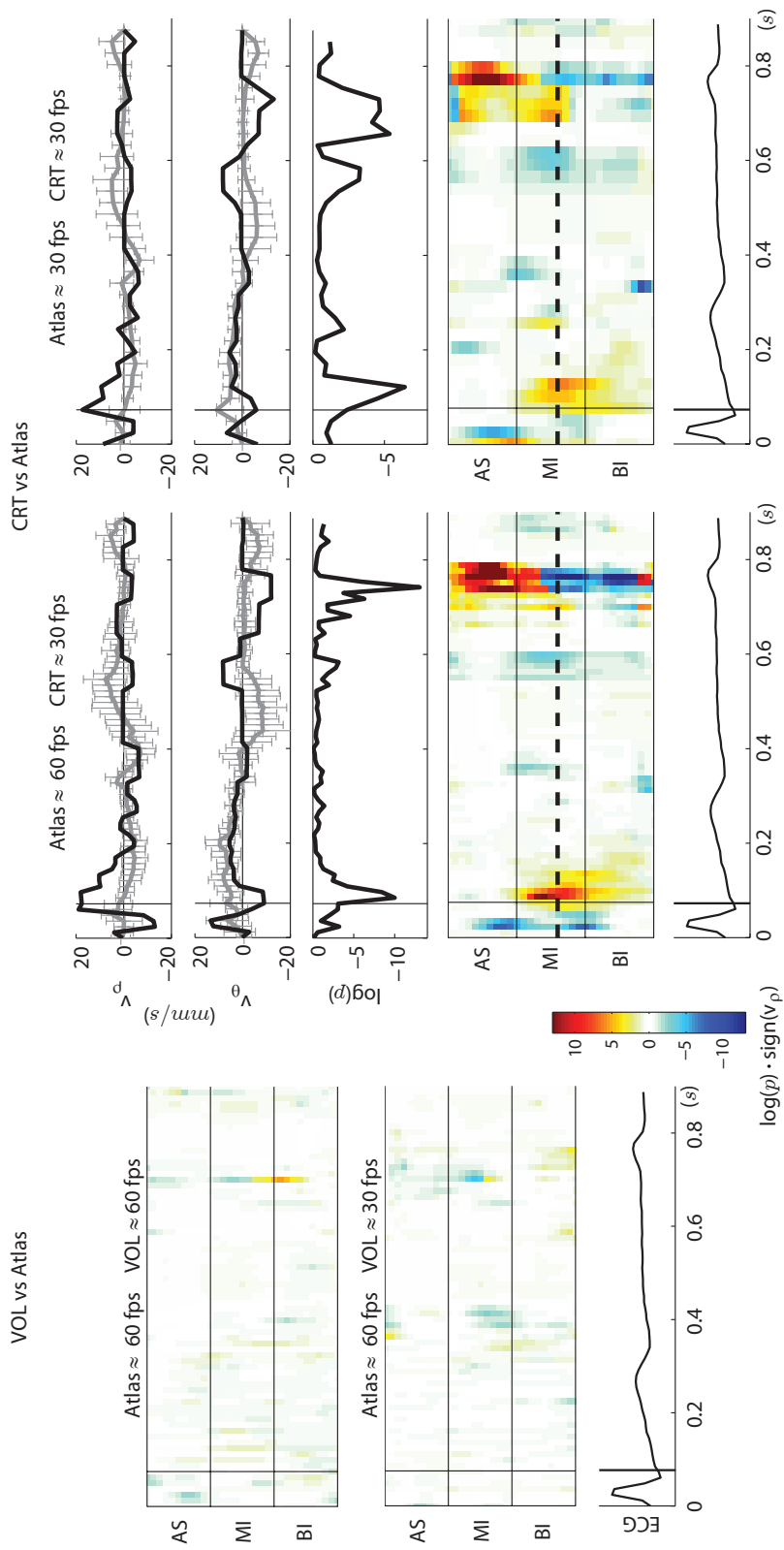


**Figure 3.9:** Left: Effect of a lower frame rate (volunteer to compare) on the  $p$ -value maps. Top: original frame rate (atlas ≈ 60 fps, volunteer to compare ≈ 60 fps). Bottom: lower volunteer frame rate (≈ 30 fps). Right: Effect of a lower frame rate (atlas population) on the  $p$ -value maps. First column: original frame rate (atlas ≈ 60 fps, CRT candidates ≈ 30 fps). Second column: lower atlas frame rate (atlas and CRT candidates ≈ 30 fps). Vertical line indicates the end of the IVC period.



In the first experiment (left part of Fig. 3.9), a volunteer was compared to the atlas (using leave-one-out cross-correlation) at its original frame rate (around 60 fps) and at a reduced frame rate, obtained by using one frame out of every two in the volunteer’s sequence. As can be inferred from Fig. 3.9, the two abnormality maps are very consistent with each other in spite of their large frame-rate differences: the pattern in both maps indicates low statistical support for abnormal motion. This confirms that the spots of motion abnormality observed on the  $p$ -value maps of the CRT candidates cannot just originate from the lower frame rate of these patients, compared to the atlas frame rate.

The second experiment illustrates the effect of a lower temporal resolution for the whole atlas population on the  $p$ -value maps. In the right part of Fig. 3.9, a CRT candidate with SF is compared to the atlas built with its original temporal resolution (around 60 fps, left column) and at a lower frame rate (around 30 fps, right column). The figure shows that the localization of motion abnormalities is still feasible with an atlas built at a lower frame rate, but with seemingly less contrast and less resolution along the timescale.

### Influence of the reference choice

To understand the effects of the reference choice on the  $p$ -value maps, we repeated the atlas construction using different subjects as reference. We chose the subjects with the three best GWNMI scores (VOL #15, which is the one used in the rest of the paper, #6 and #1), and the two worst ones (VOL #13 and #21). Few influence is observed on the  $p$ -value maps, as shown in Fig. 3.10 for CRT candidate #6. This confirms the assumption introduced in Sec. 3.3.2, namely that the bias on the abnormality indexes introduced by the use of another reference anatomy remains small.

### Overall synchronization

To evaluate the quality of the spatiotemporal synchronization described in Sec. 3.3, we acquired four sequences for the same subject and checked that the estimated velocities overlapped after the synchronization to the reference spatiotemporal system of coordinates. A bad overlap would directly reflect artifacts introduced by the spatiotemporal synchronization. These sequences differ in terms of probe orientation and zoom of the US window, which were changed intentionally between the different acquisitions. They also differ in terms of heart rate, and have therefore different numbers of frames (56, 59, 62 and 64 frames for one cardiac cycle, respectively). In that way, the variability in the acquisition parameters is comparable to the one reached for the acquisition of different patients. Figure 3.11 illustrates the overlap between the velocities at four levels of the septum. The dispersion of the reoriented velocities (vertical bars) is measured in each direction from the corresponding diagonal coefficient of the covariance matrix  $\Sigma_{\mathbf{v}}$ , defined in Sec. 3.3.3. This dispersion reflects the accuracy of the spatiotemporal synchronization scheme, but may also result from differences in the myocardial velocities and the speckle patterns of the four acquisitions, which could not be quantified with the imaging tools available for this study.

## 3.5 Application to the analysis of the CRT population

The experiments described in this section demonstrate the performance of the proposed method for the accurate characterization of septal motion abnormalities, with particular attention paid to the SF mechanism. This characterization comprises a two-stage analysis: first, the localization of abnormal motion patterns in time and space (Sec. 3.5.1), then the

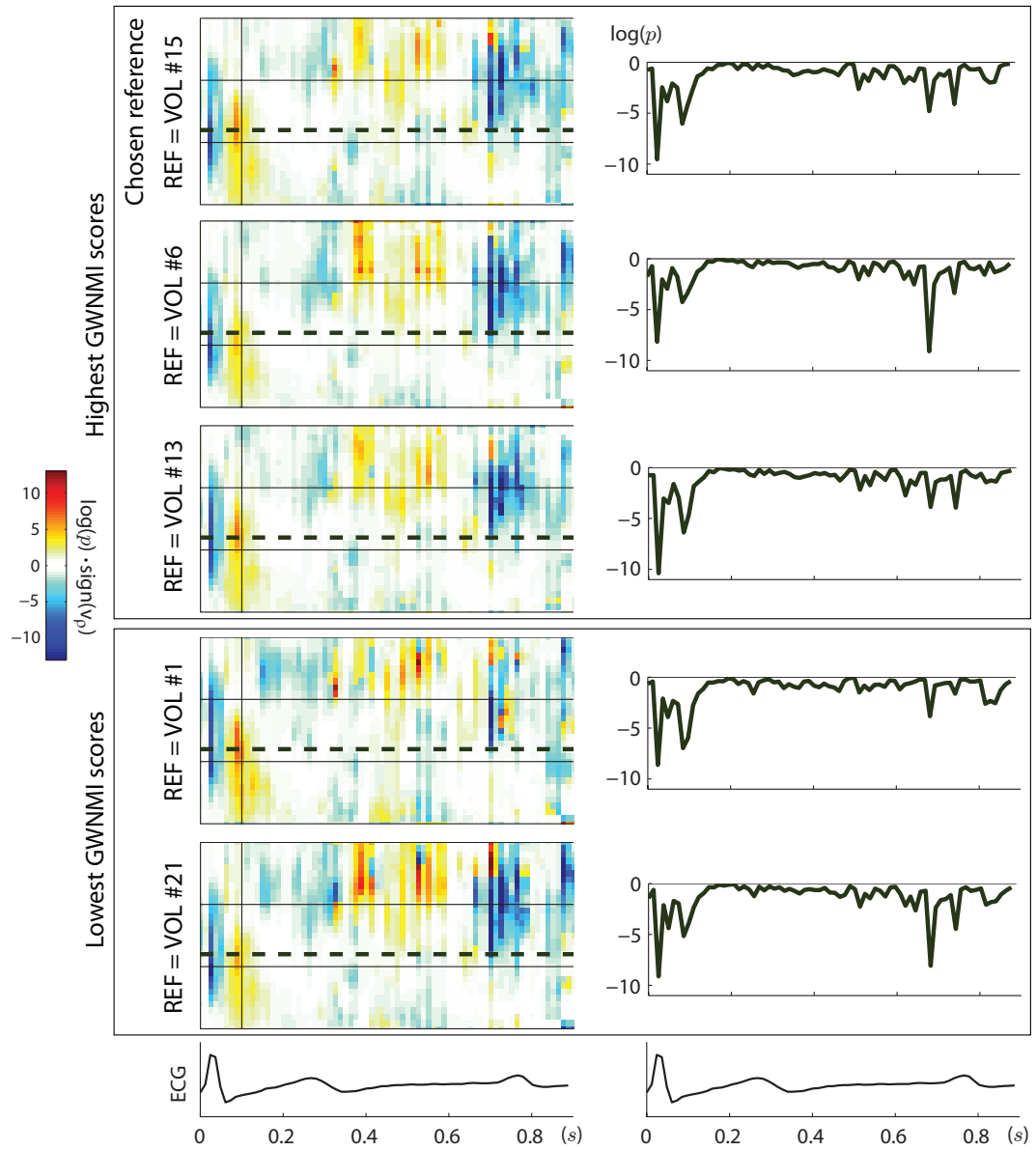


**Figure 3.10:** Influence of the reference choice on the  $p$ -value maps. VOL #15 is the reference used in the rest of the paper, VOL #6 and #1 are the subjects with the two other best GWNMI scores, and VOL #13 and #21 the subjects with the two worst ones.

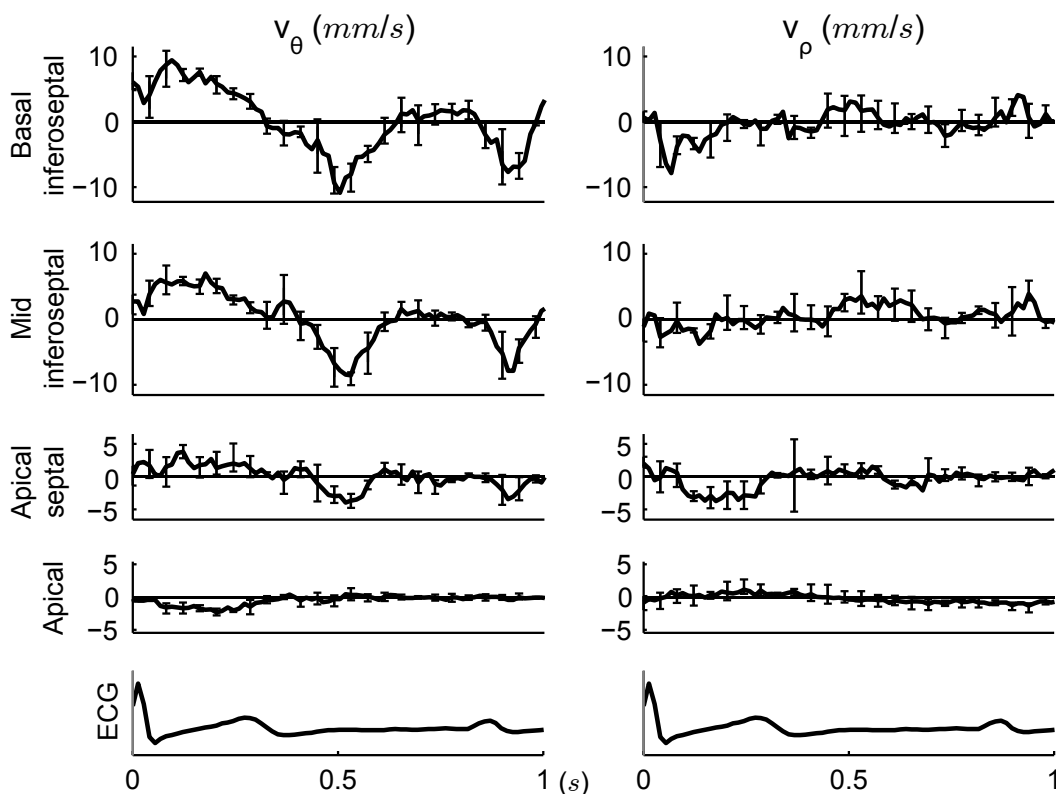


**Figure 3.11:** Repeatability in the normalization of velocities from four different acquisitions of the same subject, at four levels of the septum. Left: longitudinal velocities after reorientation; average  $\pm 1$  standard deviation in the longitudinal direction. Right: idem with radial velocities. We only display one bar plot out of every three temporal instants for the sake of clarity.

interpretation of the observed patterns, which is done regionally focusing on the magnitude of the observed abnormalities (Sec. 3.5.2), and locally on  $p$ -value maps coupling the temporal and spatial dimensions (Sec. 3.5.3). The underlying objective of this section is to check whether the abnormality information obtained by our method is in agreement with the observations made by clinicians.

### 3.5.1 Localization of motion abnormalities

*Temporal localization of septal flash.* The left part of Fig. 3.12 illustrates the temporal analysis on two CRT candidates presenting SF, at the location of the septum where maximal excursion is observed, including both velocity and  $p$ -value curves along one cardiac cycle. Low  $p$ -value means high degree of abnormality. Both plots exhibit a large abnormal inward velocity when the septum is activated, which is almost immediately followed by a fast outward motion at the time when the infero-lateral wall contracts. This specific fast pattern, when occurring during the IVC period, determines the presence of SF, as described in [190].

*Spatial localization of septal flash.* The  $p$ -value indexes obtained from our method directly allow a quantitative diagnosis at every point in space, as illustrated in the right part of

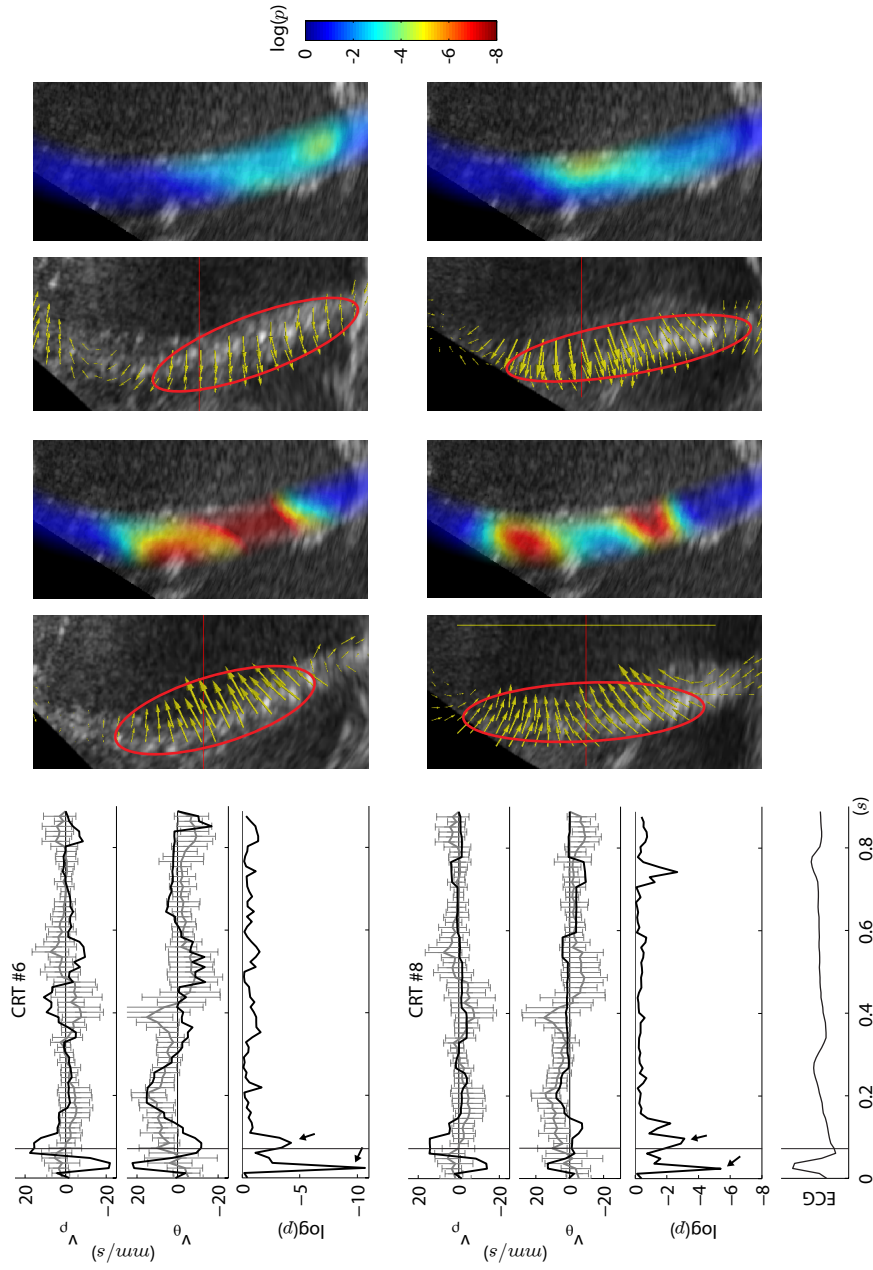


**Figure 3.12:** Comparison of two CRT candidates with SF with respect to the atlas. Left: Temporal localization of the SF phenomenon, at the location where maximum excursion is observed (mid-inferoseptal level for both patients). From top to bottom: Radial velocities (gray: atlas average  $\pm 1$  standard deviation in the radial direction, black: patient with SF), same plot with longitudinal velocities, and  $p$ -value plot along one cycle. Vertical line indicates the end of the IVC period. Arrows point out the inward and outward events. Right: Spatial localization of abnormality along the septum, at inward and outward events. In contrast, the LV of healthy subjects would mainly contract in the longitudinal direction. For each block: velocity field in the anatomy of patient  $k$ , and corresponding  $p$ -value map, defined in the reference anatomy. Arrows have been scaled by a global factor for optimal visibility. Warmer colors on the  $p$ -value maps indicate regions of higher abnormality.

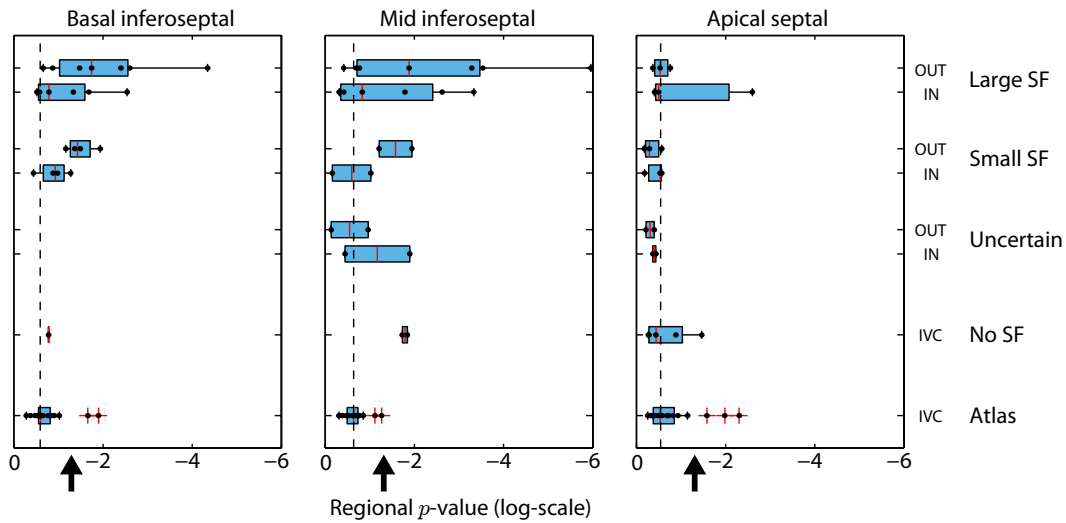


**Figure 3.13:** Comparison between regional  $p$ -values and clinical diagnosis. Arrows on the right represent the value of 0.05 below which abnormality is considered significant. Dashed line indicates the median value of the atlas population.

Fig. 3.12. We display  $p$ -value maps at inward and outward events to analyze the way SF abnormality is distributed along the septum. For each block, we represent the initial velocity field in the anatomy of the studied patient, together with the corresponding  $p$ -value map, defined in the reference anatomy. This mode of representation illustrates the agreement in the location of SF between our abnormality maps (warmer colors) and the existing velocity fields (septum moves inward/outward, faster than the normal [higher magnitude of the velocities]). In contrast, healthy hearts would contract along the longitudinal direction).

### 3.5.2 Accuracy in the quantification of abnormalities

Three experts characterized the whole set of CRT candidates involved in the study, using analysis tools similar to those proposed in [8]. As a precise and objective localization using echographic tools is hard to reproduce, we asked the observers to make their diagnosis for three regions along the septum (basal inferoseptal, mid inferoseptal and apical septal). For each zone, they associated a score to the patient, among four possible values related to the degree of observed abnormality: 1 (no SF), 2 (uncertain), 3 (small SF), and 4 (large SF). For each zone of comparison, an agreement value between the observations from the different experts was obtained from the median value of their respective scores. The observed zone was marked as uncertain if the standard deviation between the different scores exceeded 1.

For each zone, we compared the previous observations to the motion abnormality indexes obtained from our analysis, as summarized in Fig. 3.13. For the patients with SF, the comparison was performed within the temporal window in which the inward and outward events occur, which were defined specifically for each patient, using the information on radial velocity  $\mathbf{v}_\rho$  as follows:

$$\begin{aligned} \mathcal{IN} &= \{t \in IVC \mid \mathbf{v}_\rho(t) < 0\} \\ \mathcal{OUT} &= \{t \in IVC \mid \mathbf{v}_\rho(t) > 0\} \\ \mathcal{IN} &\text{ precedes } \mathcal{OUT} \end{aligned}$$

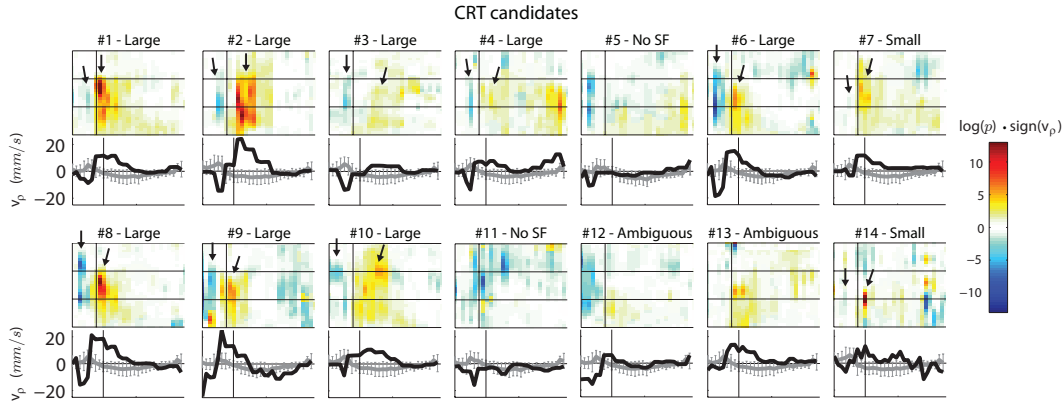


**Figure 3.14:** Motion abnormality maps and radial velocity profiles at the level of the septum with highest abnormality, during systole, for the whole set of CRT candidates. Black arrows point out the inward and outward motion during SF events, when present.

The analysis was carried out on the whole IVC interval for the subjects with normal motion (atlas population) and for the patients without SF.

The diagnosis from the experts is only available regionally in time (within the temporal windows previously described) and space (the three regions along the septum). Thus, the comparison of their observations to the atlas-based quantification of abnormality was also done regionally. As the atlas-based  $p$ -values locally define a distance to normality, a representative  $p$ -value was computed for each region from their median over the spatiotemporal comparison zone.

A range for normality was obtained by including the atlas subjects in the analysis, for which  $p$ -values were obtained using leave-one-out cross-validation on the atlas population.

Figure 3.13 presents the comparison between the atlas-based diagnosis and the experts classification. In this figure, we observe the agreement between the comparison methods at the basal inferoseptal and mid inferoseptal levels. Indeed, each group of patients show lower abnormality than the atlas group, with noticeable differences depending on the grade of SF. This is mainly visible at the mid inferoseptal level, for which the septum has the highest amplitude of motion on the tested patients. In contrast, the whole atlas population lays in the normality range ( $p$ -value  $< 0.05$ ). The different populations remain harder to distinguish at the apical septal level. The quality of the analysis in this region is commented in Sec. 3.6, together with the interpretation of the results for the zones for which the diagnosis was uncertain.

### 3.5.3 How to differentiate between patterns? Added-value of spatiotemporal maps of motion abnormalities

Combining both spatial and temporal quantification of motion abnormalities into a single map, as described in Sec. 3.4.2, facilitates the interpretation of the observed patterns and their comparison across patients. Figure 3.14 represents these abnormality maps for all the 14 CRT candidates, during the systole period. These maps are accompanied with a plot of the radial component of the velocity at the level of the septum with the highest motion abnormality for a better understanding of the observed abnormality patterns. The grade of SF obtained from experienced observers (Sec. 3.5.2) is indicated on the top. In this figure, a clear succession of inward (blue) and outward (red) abnormal motion starting during the

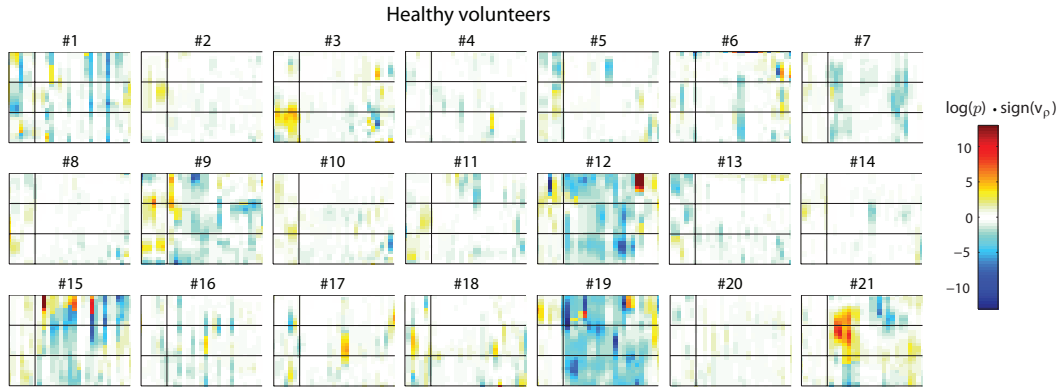


**Figure 3.15:** Motion abnormality maps during systole, for the set of volunteers.

IVC is visible on patients #1, #2, #6, #8, #9 and #10, which were all diagnosed as “large SF” by the observers. Patients #3 and #4 were also diagnosed as “large SF,” but the degree of motion abnormality is lower for both events. The inward motion pattern is almost absent for patient #7, while both events are less visible for patient #14. These two patients were diagnosed as “small SF.” The SF pattern is absent in the remaining patients (#5, #11, #12 and #13), which were all categorized as “ambiguous SF” or “no SF.” Patients #5, #11 and #12 only show inward motion abnormalities. These patterns are interpreted in Sec. 3.6.

As a comparison, Fig. 3.15 represents these abnormality maps for the whole set of volunteers. Almost no abnormality is observed for most of these subjects. Volunteers for which abnormality is visible on these maps generally have higher velocities during the whole sequence, which is particularly noticeable on the radial velocity of #12 and #19. However, all these subjects belong to the atlas population, which means that these deviations from the average velocity profile are part of the atlas variance, and are therefore taken into account in the quantification of abnormalities for the set of CRT candidates.

## 3.6 Discussion

We have described a complete framework for the computation of a statistical atlas of motion, from its construction steps to the comparison of the atlas-based diagnosis to the observations made by experts. Our experiments demonstrate the feasibility of the proposed method on 2D US sequences. We first evaluated the quality of the atlas construction steps, and then demonstrated its applicability for an accurate localization of abnormal motion patterns, focusing on a specific pattern of the septum, namely SF.

The localization and quantification tools illustrated in Fig. 3.12, 3.13, 3.14 and 3.15 shed light on the added value of the proposed indexes for the characterization of cardiac motion, in comparison with the tools currently used in clinical practice. By comparing patients within an atlas framework, we propose a local analysis of motion abnormalities, at every point in time and space (Fig. 3.12, 3.14 and 3.15) of a standardized anatomy. The use of our atlas-based indexes, which intrinsically embed a notion of normality, allows an accurate quantification of abnormality at every desired location. As illustrated in Fig. 3.13, our method agrees with the regional diagnosis performed by experts along the septum. In addition, it refines the information on the degree of abnormality observed and proposes some elements of interpretation for the zones where the diagnosis remained ambiguous.



In the case the subendocardium of the concerned region is infarcted, passive motion of the septal wall is observed when the lateral wall starts contracting and pushes the septum. Septal motion is therefore in the outward direction, but lasts longer than the IVC and is not a flash anymore. These patients are likely to belong to the left-right interaction class pointed out in [8]. In both cases, the observed zone will show lower abnormality (higher  $p$ -value) for the outward event, which is visible in particular in the plot of Fig. 3.13 representing the mid inferoseptal level, and in the maps of Fig. 3.14 for patients #5, #11 and #12. A complementary analysis based on strain may help in discarding the ambiguities between true SF and infarcted zones with passive motion.

For clarity reasons, we preferred to set the focus of this paper on the construction of an atlas based on velocities, and the demonstration of the atlas performance in localizing and quantifying abnormalities in motion. Extension of the present method to strain measurements will be included in further work for a more complete characterization of the cardiac function, as recommended in [191], and the assessment of other cardiac abnormalities.

*Limitations.* We chose to work with 2D US as it is the only modality used in clinical practice with sufficient temporal resolution to accurately identify fast motion patterns such as SF. However, the concepts developed in this paper could readily be applied to 3D US and other imaging modalities once the required temporal resolution is available in standard clinical acquisition protocols. The use of real-time 3D echocardiography [192] [101] is particularly of interest to capture out-of-plane motion, which may increase the accuracy of the proposed analysis, and extend it to specific 3D motion patterns currently not captured by our method, such as torsion.

The quality of US images is however determinant for the relevance of the observations made in this study. Depending on the tissue properties of each patient, the structure of the LV can be masked on some frames, especially at the apical level. Both the tracking accuracy and the clinical observations are affected, making the separation between the different populations less evident in this zone of the septum, as observed in Fig. 3.13.

## 3.7 Conclusion

In this paper, we proposed a new framework for the construction of an atlas that represents motion in a standard spatiotemporal coordinate system, and allows the comparison of patients against the atlas using quantitative indexes of abnormality. We evaluated the quality of the atlas construction steps, and illustrated the accuracy of the proposed indexes by applying the methodology to a population of healthy volunteers and CRT candidates with left ventricular dyssynchrony. Our experimental results demonstrated the ability of the proposed method to quantify motion abnormalities at every location in time and space. The underlying objective was the characterization of the septal flash mechanism, which proved its interest for understanding response to CRT. Our pipeline could easily be extended to the quantification of abnormalities in strain for a more advanced characterization of the mechanisms influencing the response to CRT.



CHAPTER 3.

---

## Atlas-based Quantification of Myocardial Motion Abnormalities: added-value for Understanding the effect of Cardiac Resynchronization Therapy

In this chapter, we take advantage of the atlas-based indexes introduced in Chap. 3, which intrinsically contain a definition of “normality”, to quantify the evolution of motion abnormalities in a large group of patients pre- and post- CRT, and link it to CRT response. The aim of this study is to validate the clinical value of a statistical atlas of myocardial motion on a large set of patients treated with cardiac resynchronization therapy (CRT) and to better understand the effect of CRT by the use of this atlas.

The content of this chapter is adapted from the following publication:

N. Duchateau, A. Doltra, E. Silva, M. De Craene, G. Piella, M.A. Castel, L. Mont, J. Brugada, A.F. Frangi, and M. Sitges. Atlas-based Quantification of Myocardial Motion Abnormalities: added-value for Understanding the effect of Cardiac Resynchronization Therapy. 2012. Under review.



## 4.1 Introduction

The role of cardiac resynchronization therapy (CRT) in improving both clinical condition and cardiac function of heart failure patients has been clearly demonstrated [9]. The recovery of a synchronous contraction is a first necessary step to guarantee such an improvement, and from a broader perspective, that the patient can respond to the therapy. The importance of understanding the complexity and variety of the etiologies of cardiac dyssynchrony has been recently highlighted [8] [193], as an explanation to the limitations of single measurements of mechanical dyssynchrony [3] [4]. Echocardiography [36] with tissue Doppler and speckle tracking has shown its potential for estimating myocardial motion and deformation locally, and therefore quantifying mechanical dyssynchrony on individuals. However, its capability for intra- and inter- population comparison is limited, the analysis being performed at the regional level (myocardial segments) at some specific instants of the cardiac cycle, due to the lack of a common spatiotemporal system of coordinates to perform this comparison at any spatiotemporal location. In contrast, in methods derived from statistical atlases [109] [110], the data from each subject of a given population (shape or information defined at each point of this shape) is synchronized to a common reference anatomy, which provides a multivariate representation of the local anatomical and functional features of this population. For example, a statistical atlas of the left ventricle (LV) can contain information about myocardial velocities, strain or fiber structure at any spatiotemporal location of a reference shape of the LV. Recently, an atlas-based quantification of myocardial motion abnormalities was proposed [83], where the velocities of each studied patient were characterized according to their distance to normality. In the present study, we aim at demonstrating the usefulness of this technique for the characterization of abnormal patterns of cardiac motion, specifically applied to the field of CRT. Accordingly, we aim at showing the value of the atlas approach to characterize patterns of abnormal septal motion and the relation between their evolution and CRT response in a large group of patients pre- and post- CRT.

## 4.2 Methods

### 4.2.1 Patient population

For the present study, data was collected from 21 healthy volunteers and 88 patients undergoing CRT implantation. The baseline characteristics for these subjects are summarized in Tab. 4.1. Data from the healthy volunteers (age  $30 \pm 5$  years, 14 male) served as control group for the construction of an atlas of normal motion. Enrollment criteria were that they had no history of cardiac disease and a normal echocardiographic exam. All of them showed a QRS duration  $< 120$  ms, and their baseline characteristics matched the values found in the literature for a population of patients with normal cardiac function [187]. Differences in age with the set of CRT candidates may be a limitation of this study, and is discussed at the end of this paper. Additional justifications about this population were extensively described in [83]. The use of 21 healthy volunteers was justified by computing the evolution of the motion abnormality index depending on the size of the atlas population, and leave-one-out was used to check the normality of the motion of healthy volunteers. The 88 patients compared to the atlas (age  $68 \pm 9$  years, 64 male) were patients treated with CRT based on current international clinical guidelines [13]: left ventricular ejection fraction (LVEF)  $< 35\%$ , QRS duration  $> 120$  ms, and NYHA classification III-IV or NYHA II who covered less than 500 meters in the 6 minutes walking test. The research complied with the Declaration of Helsinki and the study protocol was accepted by our local ethics committee.

		CRT (N=88)	VOL (N=21)
Age (years)		68 ± 9	30 ± 5
Male gender		64 (73%)	14 (67%)
Ischemic etiology		29 (33%)	0
QRS width (ms)		178 ± 29	81 ± 10
6 min walking test (m)		271 (168-332)	.
	I	0	21 (100%)
NYHA	II	23 (26%)	0
class	III	56 (66%)	0
	IV	7 (8%)	0
LV end-diastolic volume (mL)		247 ± 88	104 ± 27
LV end-systolic volume (mL)		186 ± 76	41 ± 9
LV ejection fraction (%)		25 ± 8	60 ± 5
MR grade III-IV (%)		26 (43%)	0
TDI Septum-to-lateral delay (ms)		63 ± 41	.
ST anteroseptal-to-posterior delay (ms)		66 (28-158)	17 ± 27

LV: left ventricular; MR: mitral regurgitation.

**Table 4.1:** Baseline characteristics of volunteers and CRT candidates.

Written informed consent was obtained from all subjects.

## 4.2.2 Definition of response

Response was defined as a reduction  $\geq 15\%$  in the LV end-systolic volume [21]. Patients who died or had heart transplantation during the study were also considered as non-responders. Clinical improvement was defined as an increase  $\geq 10\%$  in the 6 minutes walking test, or a NYHA functional class reduction  $\geq 1$  point for patients unable to complete the 6 minutes walking test at baseline.

## 4.2.3 Echocardiographic acquisition

An echocardiographic examination using a commercially available system (Vivid 7, GE Healthcare, Milwaukee, WI) was performed in all patients at baseline and at 12 months follow-up after the implant. A zoomed-in 4-chamber view of the LV was acquired during breath-hold to minimize the influence of respiratory motion. LV volumes and ejection fraction were measured using the 2D Simpson’s method (biplane). Mitral regurgitation was semi-quantitatively classified into 4 degrees according to the color flow jet area method. LV dyssynchrony was also evaluated by two techniques: (1) measuring differences in time-to-peak myocardial velocity between the septal and the lateral walls of the LV, derived from color tissue Doppler 4 chamber views [17]; (2) measuring the time difference between peak systolic strain of the anteroseptal and posterior LV walls [171].

## 4.2.4 Automatic quantification of myocardial motion abnormalities

The atlas pipeline described in [83] was applied to the acquired 4-chamber views of the LV, focusing on the septal region (Fig. 4.1). Myocardial velocities were extracted from each sequence using speckle tracking based on image registration algorithms. Each sequence was spatiotemporally aligned to a common reference anatomy, chosen among the set of healthy volunteers, using ECG matching (time) and image registration (space). The importance of this alignment step is commented in the Results section. Average and covariance of myocardial velocities over the set of healthy volunteers encoded a representation of normal motion. Abnormality in local motion was computed through a statistical distance on

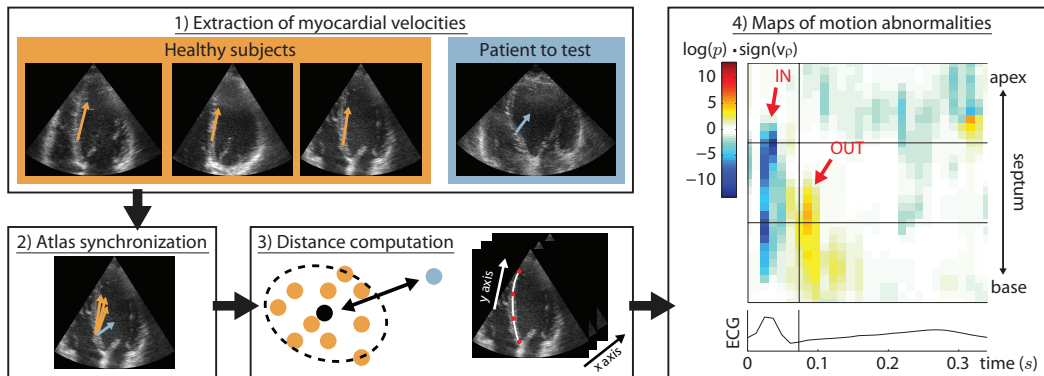


**Figure 4.1:** Pipeline for the atlas-based quantification of septal motion abnormalities, as described in [83]. Right part represents the motion abnormality map computed for one patient with SF during systole ( $p$ -value in logarithmic scale weighted by the sign of the radial velocity  $v_p$ ). Red arrows indicate the localization of inward (IN) and outward (OUT) events of SF. The vertical line indicates the end of the isovolumic contraction period.

velocities, between each individual and the atlas population (Mahalanobis distance). This computation returned a  $p$ -value at every location of the myocardial wall, low  $p$ -value indicating high degree of abnormality. A convenient way of representing this information consists of color-coded maps, inspired from anatomical M-mode echocardiographic images, in which the septal wall has been unfold around its medial line and used as vertical dimension, time being used as horizontal axis (Fig. 4.1). The color code for these maps encodes the  $p$ -value in a logarithmic scale, multiplied by the sign of the radial velocity, to distinguish between septal abnormal motion patterns (Fig. 4.1 and Sec. 4.3). Blue color represents highly abnormal inward motion of the septum, while red color represents highly abnormal outward motion. No abnormality is therefore represented by white color.

#### 4.2.5 Statistical analysis

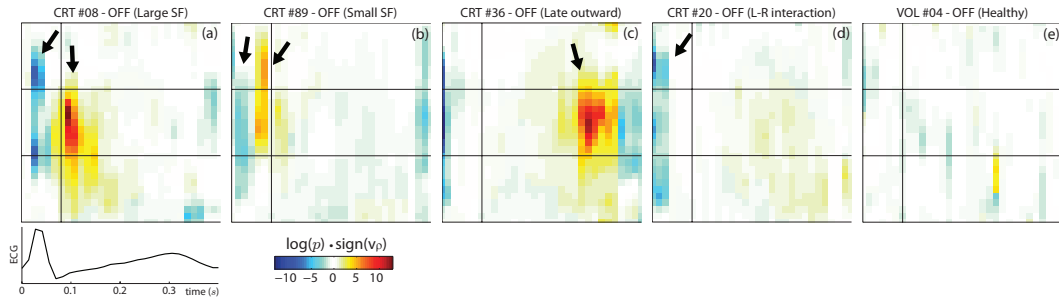
Normal distribution of quantitative variables was assessed using the Kolmogorov-Smirnov test. Normally distributed quantitative variables were expressed as mean  $\pm$  standard deviation, and unpaired Student's  $t$ -test was used for inter-groups comparison. When large deviations from the Gaussian distribution were noticed, the variable was expressed as median and (interquartile) range, and Mann-Whitney  $U$ -test was preferred for inter-groups comparison, while Wilcoxon signed-rank test was used for the comparison of paired data. Categorical variables were expressed in percentage over the number of patients for which data was available, and were compared using Fisher's exact test.  $p$ -values below 0.05 were considered as statistically significant difference between the tested groups. All data were analyzed using the SPSS statistical package (version 15.0, SPSS, Inc., Chicago, IL).

### 4.3 Results

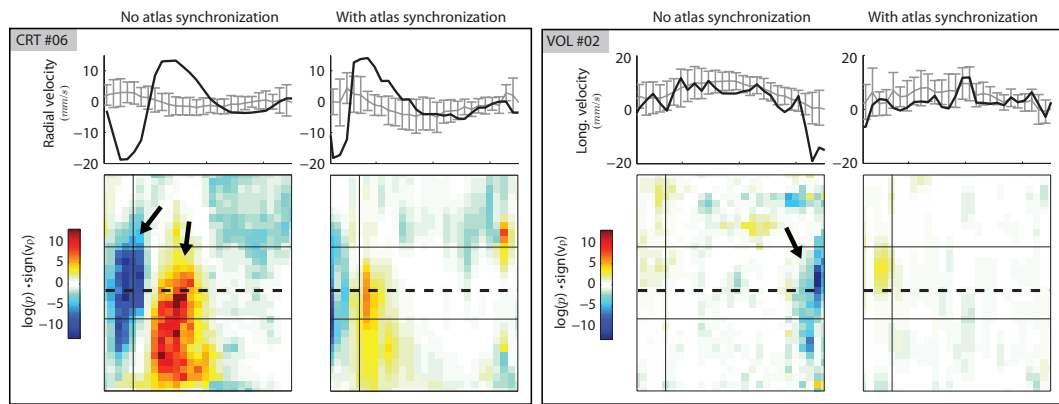
#### 4.3.1 Patterns of motion abnormality at baseline

Figure 4.2 represents the motion abnormality maps of five different subjects at baseline, during systole, illustrating the variety of patterns of abnormal motion that may be observed along the septal wall: (A) intra-ventricular dyssynchrony, assessed by the presence of a fast





**Figure 4.2:** Variety of the patterns observed on the motion abnormality maps.



**Figure 4.3:** Radial velocity and motion abnormality map for one patient and one healthy volunteer without and with the atlas spatiotemporal synchronization.

inward / outward motion of the septum during the isovolumic contraction period, otherwise called septal flash (SF) [8]. Variations in the amplitude of SF are associated to variations in the intensity of the blue- and red-colored abnormalities on the map (Fig. 4.2a and 4.2b). This pattern was present in 60 patients (68%) of our study group; (B) inter-ventricular dyssynchrony, with late systolic outward motion (Fig. 4.2c), or with inward motion only (Fig. 4.2d), referenced in the literature as left-right interaction (LR) [8] [193]. In contrast, no abnormal pattern is observed on a healthy volunteer (Fig. 4.2e).

### 4.3.2 Importance of the atlas spatiotemporal alignment

Figure 4.3 compares the maps of abnormality obtained for one patient with SF and one healthy volunteer, without (left) and with (right) the spatiotemporal alignment step inherent to the atlas construction. On the SF patient, the lack of spatiotemporal alignment overestimates the abnormality and the duration of the abnormality pattern, which does not fit anymore within the isovolumic contraction period. On the healthy volunteer, the lack of spatiotemporal alignment induces large abnormalities at the end of systole, which would make the subject being considered a false positive.

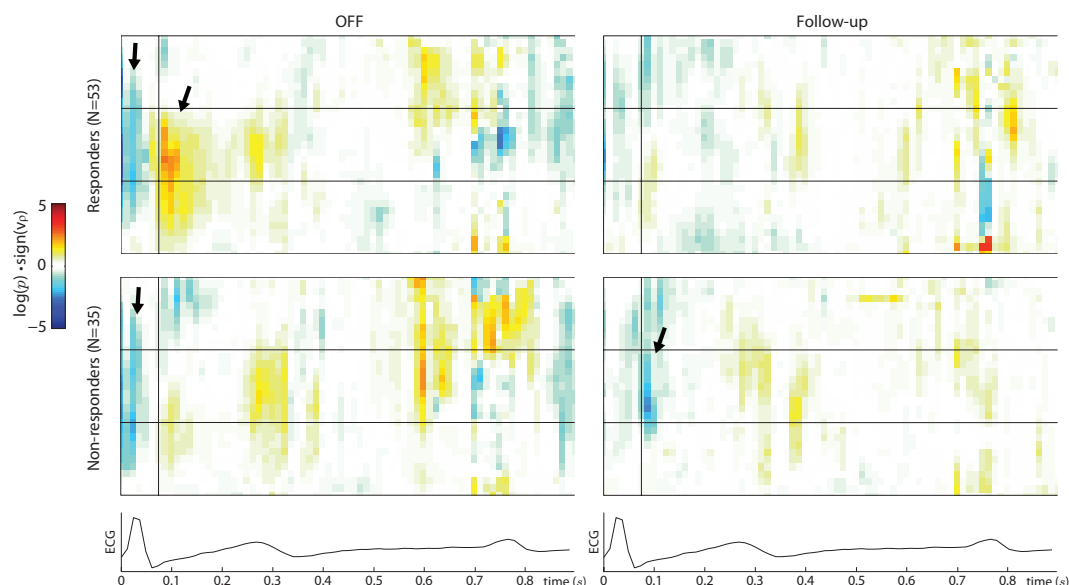


**Figure 4.4:** Average abnormality map for the set of volume responders and non-responders, at baseline and follow-up.

### 4.3.3 Response to CRT

Fifty-three patients (60%) showed significant reverse remodeling and were considered responders. The clinical condition improved in 72 patients (82%), 46 of them being also volume responders. One patient had heart transplantation, and died during the study. A second patient died from heart failure without heart transplantation.

### 4.3.4 Overall effects of CRT

There were no statistically significant differences at baseline between responders and non-responders for all the parameters (Tab. 4.2), except for (1) the amount of mitral regurgitation, moderate-severe mitral regurgitation being more frequent in non-responders ( $p = 0.04$ ), and (2) septal-to-lateral delay derived from tissue Doppler, responders having more dyssynchrony at baseline as measured by this parameter ( $p = 0.04$ ). Evolution of motion abnormalities with CRT The population of responders showed lower abnormalities at follow-up, and higher reduction of abnormalities in comparison with baseline. Values for the evolution of motion abnormalities in each spatiotemporal region are displayed in Tab.4.3, the highest reduction being observed for responders at basal- and mid-inferoseptal levels ( $p < 0.001$ ). The spatiotemporal localization of the motion abnormalities at baseline and follow-up is visible in Fig. 4.4, which represents the average abnormality map for the groups of responders and non-responders. Little abnormality in septal motion was observed at follow-up for the group of responders, while non-responders still presented a peak of abnormality with inward motion at the end of the isovolumic contraction period, predominant at mid-inferoseptal level, supporting the regional observations of Tab. 4.3. The patterns visible at baseline also indicated that large SF predominated in the group of responders, and was corrected at follow-up, while small SF and LR predominated in the group of non-responders.



		Resp. (N=53)	Non-resp. (N=35)	<i>p</i> -value
Age (years)		67 ± 9	69 ± 8	NS
Male gender		36 (68%)	28 (80%)	NS
Ischemic etiology		15 (28%)	14 (31%)	NS
QRS width (ms)		181 ± 27	172 ± 31	NS
6 min walking test (m)		275 (197-320)	270 (0-336)	NS
	I	0	0	.
NYHA	II	14 (27%)	9 (27%)	NS
class	III	36 (69%)	20 (59%)	NS
	IV	2 (4%)	5 (15%)	NS
LV end-diastolic volume (mL)		256 ± 95	231 ± 75	NS
LV end-systolic volume (mL)		196 ± 79	172 ± 68	NS
LV ejection fraction (%)		25 ± 7	27 ± 9	NS
MR grade III-IV (%)		10 (29%)	16 (59%)	0.04
TDI Septum-to-lateral delay (ms)		70 ± 36	51 ± 46	0.04
ST anteroseptal-to-posterior delay (ms)		70 (33-182)	48 (21-120)	NS

LV: left ventricular; MR: mitral regurgitation.  
NS: Non-significant statistical difference (*p*-value ≥ 0.05).

**Table 4.2:** Baseline characteristics of CRT candidates according to the response at follow-up.

		Responders			Non-responders		
		OFF	FU	<i>p</i> -value	OFF	FU	<i>p</i> -value
SYS	BI	1.02 (0.84-1.27)	0.74 (0.64-0.99)	< 0.001	0.96 (0.72-1.16)	0.81 (0.73-0.97)	NS
	MI	1.15 (0.97-1.74)	0.86 (0.66-1.22)	0.001	1.26 (0.81-1.58)	1.03 (0.80-1.30)	NS
	AS	0.82 (0.65-0.99)	0.78 (0.63-1.06)	textNS	0.68 (0.54-1.10)	0.78 (0.66-0.99)	NS
DIA	BI	0.76 (0.52-1.22)	0.76 (0.52-1.22)	0.014	0.65 (0.51-0.89)	0.57 (0.47-0.74)	NS
	MI	0.96 (0.62-1.71)	0.68 (0.52-1.20)	0.013	0.78 (0.55-1.62)	0.77 (0.53-0.94)	NS
	AS	0.90 (0.62-1.23)	0.66 (0.51-1.03)	0.030	0.84 (0.46-1.45)	0.70 (0.51-1.04)	NS

*p*-value corresponds to the discrimination score between baseline and follow-up abnormalities.

BI: Basal Inferoseptal; MI: Mid Inferoseptal; AS: Apical Septal; SYS: Systole; DIA: Diastole.

NS: Non-significant statistical difference (*p*-value ≥ 0.05).

**Table 4.3:** Abnormality reduction according to the response at follow-up.

## 4.4 Discussion

The results of this study demonstrate the usefulness of the proposed atlas-based quantification of myocardial motion abnormalities for CRT studies, highlighting (1) the relevance of statistical indexes that intrinsically embed the notion of “normality”, to characterize patterns of mechanical dyssynchrony and their evolution with the therapy; and (2) the need for a spatiotemporal synchronization of the data to avoid bias in the inter-subject comparison.

### 4.4.1 Abnormal patterns of septal motion and cardiac dyssynchrony

[8] proposed a classification of patients according to their pattern of mechanical dyssynchrony, and studied CRT response for each of these groups. Half of the patients had SF, which was associated to CRT response when the mechanism had been corrected at follow-up. Similar observations were made on patients with contractile reserve, for which SF was induced by dobutamine stress echocardiography [23]. The presence of an abnormal motion of the septum associated to an intra-ventricular type of dyssynchrony was first reported from M-mode observations [194] [195] [196] [197]. The authors described a specific pattern of mechanical dyssynchrony interpretable as a direct consequence of Left Bundle-Branch Block (LBBB) [8] [193] [198]. [199] interpreted it as the result of active septal contraction during LBBB and therefore suggested its inclusion in LV dyssynchrony studies. High re-



response rates were recently reported for septal rebound stretch [34] and apical rocking [35], two patterns very closely related to SF. Inter-ventricular dyssynchrony (LR) was described as a passive motion of the septum [8] [193] due to the presence of infarcted septal regions and a long inter-ventricular delay, the correction of which led to clinical improvement but not volume response. More complex patterns were also reported, resulting from prolonged atrio-ventricular delays or combined mechanisms [8]. The objective of the present study was to consider all types of septal motion abnormalities that may be observed on our study group (Fig. 4.2). This was achieved through the comparison of the motion of any individual to a control group with normal cardiac function, using a common system of coordinates to perform this comparison. This framework also allowed intra-subject comparison between baseline and follow-up data (Fig. 4.4 and Tab. 4.3).

#### 4.4.2 Conventional methods for dyssynchrony assessment

The limits of single measurements from current echocardiographic techniques<sup>6</sup> such as tissue Doppler and speckle tracking have been largely discussed [3] [4]. In particular, the relevance of considering individual components of the measured parameters (either temporally using time-to-peak or time-to-onset measurements, or spatially by considering segmental values) has been pointed out. The practical difficulties of identifying the peak values [6] may bias the analysis, despite the fact that statistical difference may be observed between responders and non-responders using these parameters (Tab. 4.2). To overcome these limitations, we chose a mechanistic approach inspired from the protocol presented in [8], therefore considering the whole patterns of dyssynchrony that may be observed along the septum (Fig. 4.2).

#### 4.4.3 Added-value of atlas-based quantification of motion abnormalities

The protocol described in [8] allows quantitative assessment of the abnormal patterns of septal motion (presence, timing and maximal excursion, if measurable), but is not automatic, pattern-dependent, and requires expert interpretation. Current echocardiographic techniques [36] such as tissue Doppler and speckle tracking allow the quantification of motion and deformation locally, but are still not adapted to perform intra- and inter-subject comparisons. Tissue Doppler is highly dependent of the insonation angle and only provides a one-dimensional measurement (the projection of the velocity vector along the observation beam), which limits its interest for our application. Both techniques process the sequence of each patient individually, but do not allow any comparison at any spatiotemporal location of a common system of coordinates. The need for such a comparison space, guaranteed by the use of a statistical atlas framework, was illustrated in Fig. 4.3. One of the main contributions of the present work consists in the computation of statistical indexes that intrinsically perform a comparison to normality. This concept is analogue to the learning process made by a clinical observer, which uses healthy and pathological sequences to learn the representations of specific patterns of abnormal motion. In our case, the analysis is completely quantitative, which allows baseline and follow-up comparisons, either regionally (Tab. 4.3) or locally at every point of the septal wall (Fig. 4.4).

#### 4.4.4 Changes in LV dyssynchrony induced by CRT

The primary objective of CRT is to restore the coordination in the motion of the cardiac chambers. With optimized resynchronization, cardiac function is expected to improve, leading to notable improvements in patient condition and allowing reverse remodeling of the LV

[12]. The link between mechanical dyssynchrony and CRT response is still a controversial issue, partially due to the limitations of single measurements of mechanical dyssynchrony [3] [4]. In contrast, mechanistic approaches [8] [193] do not discard the complexity of the etiologies of cardiac dyssynchrony and shed new light on the understanding of the effects of CRT. The therapy is expected to be highly efficient on patients with SF, for which mechanical dyssynchrony is mainly the consequence of an electrical problem (LBBB) [193] [198] [199]. In contrast, the therapy may have lower effect in case of passive motion of the septum (LR) or more complex mechanisms where mechanical dyssynchrony is a consequence of wall necrosis and akynesia of a given LV segment, rather unable to be corrected through electrical resynchronization [8]. Additional factors may also condition the ability of a patient to respond despite the reduction of the abnormal dyssynchrony patterns present at baseline. The presence of an extensive scar can limit the ability of the LV to show reverse remodeling in this region. The lack of contractile reserve [200], the presence of atrial fibrillation [201], an inappropriate lead position [202], and the patient condition at baseline (too advanced heart failure so that the patient could not respond [203]) may also strongly influence CRT response. The inclusion of additional variables of non-response such as the ones identified above is highly recommendable, and will lead to refinements of current multi-parametric analysis of CRT response [31] [32].

#### 4.4.5 Other potential clinical applications of statistical atlases of motion to cardiac imaging

We chose to work with 2D echocardiography as it is the most widespread modality in clinical practice with sufficient temporal resolution to accurately identify fast motion patterns such as SF. Using 3D echocardiography would allow the characterization of all myocardial segments, but this modality does not currently fulfill the above-mentioned technical requirement. We considered that apical 4-chamber represented the most relevant 2D view for our application, as we focus on types of mechanical dyssynchrony that may affect the whole septum, from base to apex. A reproducible position of the observation plane is harder to achieve in short axis views, which may be a strong limitation for building a statistical atlas from this view. Nonetheless, the methodology applied in this study is not specific to echocardiography and abnormal septal motion, and could be readily applicable to other imaging modalities (magnetic resonance, computed tomography ...), other clinical settings (stress echocardiography, ischemic cardiomyopathy ...), and other mechanisms of abnormal motion. The proposed technique could also be extended to compare individuals to a population with one of these specific abnormal motion patterns, and not only to normality, as described elsewhere.<sup>32</sup> Limitations The study focuses on motion abnormalities only. Computing maps of strain abnormalities would certainly help refining the analysis for patients who may have similar motion abnormality patterns despite different mechanisms. In particular, this may improve the understanding of CRT response, as the presence of local infarction may affect both the dyssynchrony patterns and the ability of the LV to remodel, and therefore, condition CRT response. The atlas of normal motion was built from a group of healthy volunteers recruited for research purposes, within our institution, which explains the difference in age with the set of CRT candidates, and may be a limitation to our study. Recruitment of older volunteers was not performed for practical reasons. Nonetheless, the definition of a normal cardiac function still remains a paradigm. Cardiac efficiency may not be preserved when the subject gets older, resulting in a less “normal” function. In addition, the parameter we look at, namely, motion, may not be as sensitive to such aging changes as compared to other motion parameters such as strain. The current study focused on observations of voxel-wise

motion abnormalities and did not attempt to do any classification of patients based on the observed patterns of abnormal motion, which would require the use of specific pattern analysis techniques [204]. The relation between patterns of mechanical dyssynchrony and CRT response is still complex [8] and such an analysis may also take into account external factors that condition CRT response, as commented in the Discussion section. Finally, the criteria for CRT response should also be considered carefully [205] [206]. In particular, the definition of fixed thresholds for defining response is certainly a limit for a clear understanding of the effects of CRT, in comparison with the use of a spectrum of responses, involving additional measures of CRT outcome [25].

## 4.5 Conclusion

The results presented in this study demonstrated the usefulness of an atlas-based quantification of motion abnormalities for characterizing the evolution of specific patterns of dyssynchrony with CRT. In particular, its combination with a comprehensive understanding of the etiologies of cardiac dyssynchrony allowed a better interpretation of the effects of the therapy.



---

## Constrained manifold learning for the characterization of pathological deviations from normality

This paper describes a technique to (1) learn the representation of a pathological motion pattern from a given population, and (2) compare individuals to this population. Our hypothesis is that this pattern can be modeled as a deviation from normal motion by means of non-linear embedding techniques. Each subject is represented by a 2D map of local motion abnormalities, obtained from a statistical atlas of myocardial motion built from a healthy population. The algorithm estimates a manifold from a set of patients with varying degrees of the same disease, and compares individuals to the training population using a mapping to the manifold and a distance to normality along the manifold. The approach extends recent manifold learning techniques by constraining the manifold to pass by a physiologically meaningful origin representing a normal motion pattern. Interpolation techniques using locally adjustable kernel improve the accuracy of the method. The technique is applied in the context of cardiac resynchronization therapy (CRT), focusing on a specific motion pattern of intra-ventricular dyssynchrony called septal flash (SF). We estimate the manifold from 50 CRT candidates with SF and test it on 37 CRT candidates and 21 healthy volunteers. Experiments highlight the relevance of nonlinear techniques to model a pathological pattern from the training set and compare new individuals to this pattern.

The content of this chapter is adapted from the following publication:

N. Duchateau, M. De Craene, G. Piella, and A.F. Frangi. Constrained manifold learning for the characterization of pathological deviations from normality. 2012. Under review.

## 5.1 Introduction

### 5.1.1 Patient selection for CRT

In this paper, we address the issue of learning the representation of a pathological motion pattern from a given population, and its use for the comparison of individuals to this population. Our strategy is based on the fact that different grades of the same disease, for a patient or within a population, can be seen as progressive impairments of the normal condition of an organism. This notion is particularly of interest for the understanding of this disease, from the early detection of its onset to the quantification of its progression and its monitoring post-treatment. In particular, we would like to apply these considerations to cardiac resynchronization therapy (CRT) studies, supported by the following paradigm: CRT targets the correction of the dyssynchrony in the motion of the cardiac chambers, leading to improvements in the cardiac function, the patient condition, and ventricular size [12]; however, CRT patient selection still discards mechanical dyssynchrony as a selection criteria [13]. There are several reasons for this: there is currently no consensus regarding the accurate characterization of mechanical dyssynchrony, its link with CRT outcome, and the way to include it within the patient selection process [3] [4] [26] [27].

Recently, [8] discussed the advantages of considering specific groups of mechanical dyssynchrony in the CRT selection process. Each of these groups was associated to one specific pathological pattern of myocardial motion and deformation, with different grades of abnormality with respect to a healthy cardiac function. The relevance of similar patterns of mechanical dyssynchrony was also described in [34, 35], using more quantitative measurements. Based on these findings, a straightforward improvement of CRT patient selection would be achieved through the recognition of such patterns in new CRT candidates, as the response rate of each of these patterns is roughly known. The same concept could also be applied to quantitatively grading the severity of the disease or the response to the therapy. Nonetheless, all the above-cited methods still lack reproducible tools to perform inter-subject comparison, as discussed in [4], which limits their applicability.



### 5.1.2 Robust comparison through statistical atlases

Statistical atlases were initially designed for representing instances of a given population, by modelling the statistical distribution of anatomical and functional features within this population [109, 110]. In these frameworks, the data of each subject is normalized to a common anatomical reference, which allows reproducible intra- and inter- population comparison. Atlases of motion and deformation [113, 112, 111] fit for the study of cardiac dyssynchrony, namely comparing the myocardial velocities and strain of individuals to a reference population (either healthy or with the same disease) used to build the atlas. In particular, [83] proposed a pipeline for the characterization of abnormal patterns of ventricular dyssynchrony, in comparison with a healthy population, using an atlas-based quantification of local myocardial motion abnormalities. However, the tools used for statistically modelling the variability of healthy subjects may not be adequate if the strategy is extended to build an atlas for a specific pattern of dyssynchrony. Variations of the pattern localization within the cardiac cycle and along the myocardial wall may bias the estimation of the local variability for this population, despite its synchronization to a common system of spatiotemporal coordinates, therefore requiring the inclusion of more complex statistics or pattern analysis techniques in the atlas construction.

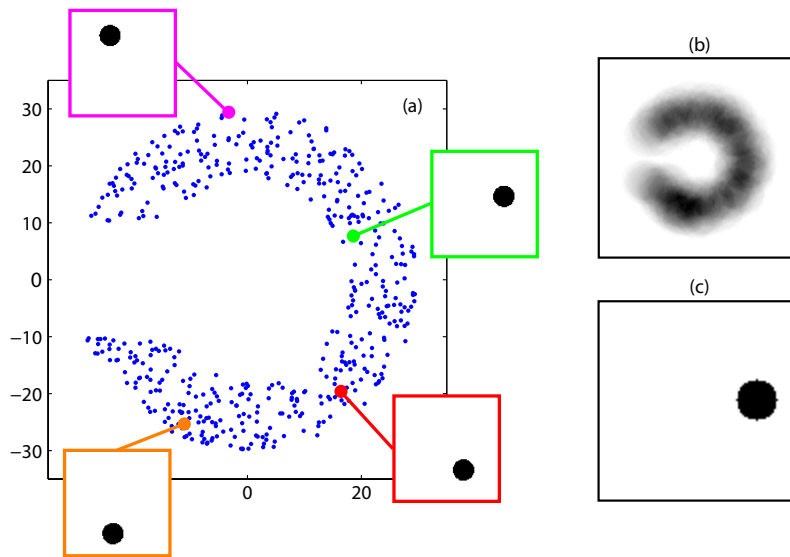


**Figure 5.1:** (a) Set of synthetic images representing a black disk over a white background. The maximum dimensionality of the space of images corresponds to the number of pixels of each image, but each synthetic image lies in a 2D subspace, the position of each disk being associated to a coordinate in a 2D space (blue dots). (b) Average image, without considering that data is arranged according to a 2D structure. (c) Fréchet mean image on the data-driven manifold, corresponding to coordinates  $(25, 0)$ .

### 5.1.3 Comparison to a given population

The comparison of individuals to a specific pattern of dyssynchrony can be seen as a two-steps approach: (1) finding a relevant space to model this pattern, and (2) defining a distance to this population through the mapping of any individual to this space.

The definition of an optimal space for representing and comparing populations has been extensively commented in the literature [155]. A  $k$ -nearest neighbours comparison in the original space, or linear dimensionality reduction techniques may bias the analysis in case the modeled population lies on a non-linear space ([207] [153] and Fig. 5.1).

In contrast, a manifold representation is particularly of interest for our application as it assumes that the global structure of the modeled population may be non-linear, and its parametrization allows inter-subject comparison along this structure.

Principal geodesic analysis [115] is a generalization of PCA for data lying on a manifold, but is described in cases where the manifold structure is already known and independent of the processed data.

Manifold learning algorithms were proposed to estimate the low-dimensional structure of the studied dataset by taking into account the local properties of the input data in the dimensionality reduction process (Isomap [153], Local Linear Embedding [208], Laplacian eigenmaps [209], kernel-PCA [210]).

The comparison of individuals to the modeled population requires mapping this new data to the manifold. Methods solving the “pre-image problem” [152, 211, 212] estimate the image generated from the manifold that shares the same coordinates than the input image, but do not explicitly provide a formulation for the mappings between the ambient space and the manifold system of coordinates.

Several works provided an explicit formulation of the above-mentioned mappings, extending the concept of principal curves [213], a non-linear generalization of PCA, using kernel

regression on scattered data. [214] demonstrated the analogy between these two concepts when the number of points tends to infinity. [215] proposed a framework to map new data to the manifold system of coordinates. The computation of the inverse mapping (estimating the image from the initial ambient space corresponding to a given manifold coordinate) was targeted in [216, 214, 217, 218, 118].

#### 5.1.4 Proposed approach

In this paper, we propose a framework for comparing the myocardial motion of individuals to a population with a specific pattern of abnormal motion, using manifold learning techniques to represent this population as a progressive deviation from normality. We extend manifold learning techniques to embed the definition of a relevant origin within the manifold, and use kernels with locally adjustable bandwidth to improve the accuracy of the mappings between the space of input images and the space of coordinates parameterizing the manifold.

The originality of our method resides in the use of 2D maps of local myocardial motion abnormalities as input, as introduced in [83]. This highlights the presence of specific abnormal motion patterns, which can be represented by a manifold structure specific to each pattern, and allows the definition of a physiologically meaningful origin within the manifold, representing a normal motion pattern. Each pathological pattern is therefore considered a deviation from normality along a manifold structure. The proposed technique represents a step forward for patient comparison in clinical applications, as it facilitates the identification of the closest class a sample falls in (distance to the manifold) and the localization of this sample within the identified class (distance to normality along the manifold).

The method is applied in the context of CRT, comparing both healthy subjects and patients to a population with a specific pattern of intra-ventricular dyssynchrony called septal flash (SF) [8]. This pattern consists of a fast inward / outward radial motion of the septum during the isovolumic contraction period, contrasting with healthy hearts, which contract along the longitudinal direction (Fig. 5.2, 5.3 and 5.4). [199] interpreted SF as the result of active septal contraction during left bundle-branch block, which was shown to actively condition CRT outcome [8] [198].

A preliminary version of this work was presented in [204], in which we illustrated the feasibility of such an approach. The current paper improves the whole methodology, from the atlas construction steps (use of temporal diffeomorphic free-form deformation, [73]) to the patient comparison to the manifold (use of locally adjustable kernels) and in-depth tuning of the whole set of parameters, using both synthetic and real data.

## 5.2 Methods

The computation of a distance between individuals and a given population considered as a pathological deviation from normality consists of three steps: (1) the quantification of motion abnormalities for all the subjects in the dataset, (2) the estimation of a relevant manifold for the training population, constrained to pass by an origin representing normal motion, and (3) the mapping of any subject to the manifold.

### 5.2.1 Atlas-based computation of myocardial motion abnormalities

The input images for our method consist of 2D spatiotemporal maps of myocardial motion abnormalities, obtained from a statistical atlas of motion built from healthy volunteers. The





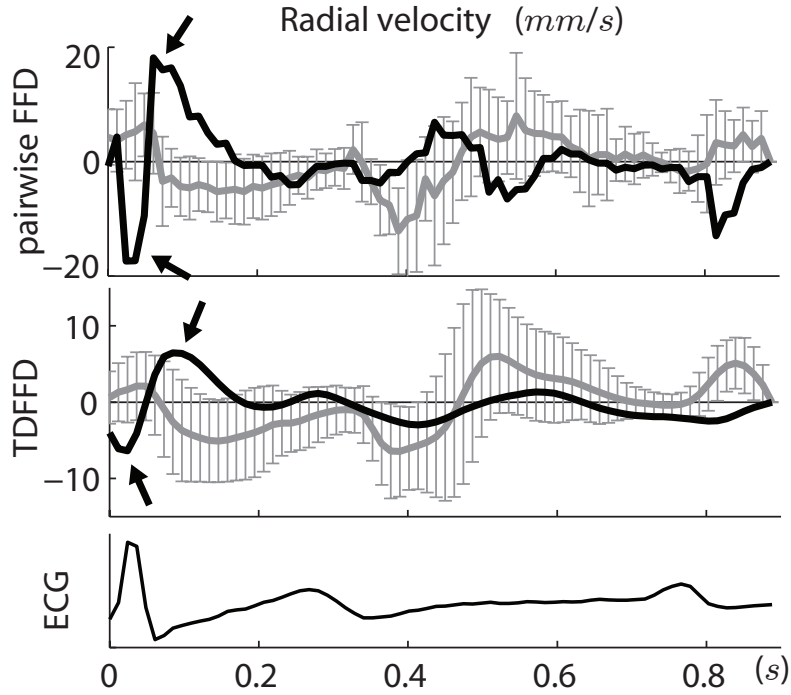


**Figure 5.2:** Radial velocities at one point of the septum (mid-inferoseptal level) during one cardiac cycle, for one CRT candidate with SF (black curve, arrows indicate the inward and outward events of SF), and the atlas of healthy volunteers (gray, average velocity  $\pm$  standard deviation). Comparison between diffeomorphic FFD between each pair of consecutive frames, providing piece-wise stationary velocities [83], and temporal diffeomorphic free-form deformation (TDFFD, [73]), which enforces temporal consistency and provides differentiable velocities, all pairs of frames being considered simultaneously during the computation.

implementation used in the current paper for computing these maps improves the pipeline proposed in [83], as described in the following paragraphs.

### Motion extraction

Myocardial velocities are extracted from the image sequence of each volunteer, at each point in time and space, using image-based registration. The diffeomorphic free-form deformation (FFD) implementation used in [83] provides piece-wise stationary velocities, which may be a limitation for the temporal synchronization step of the atlas building (Fig. 5.2). In our current implementation, we preferred the temporal diffeomorphic free-form deformation (TDFFD) method proposed in [73], which enforces temporal consistency and provides differentiable velocities.

We used a multi-resolution implementation of the TDFFD, the initial grid size being of  $5 \times 3$  control points in the spatial direction and 1 control point per frame in the temporal direction. Mean square error was used as similarity metric, combining a comparison to the first frame of the sequence and the comparison of consecutive frames [104], with equal weights. The L-BFGS-B algorithm [180] was chosen as optimizer for the whole registration procedure.

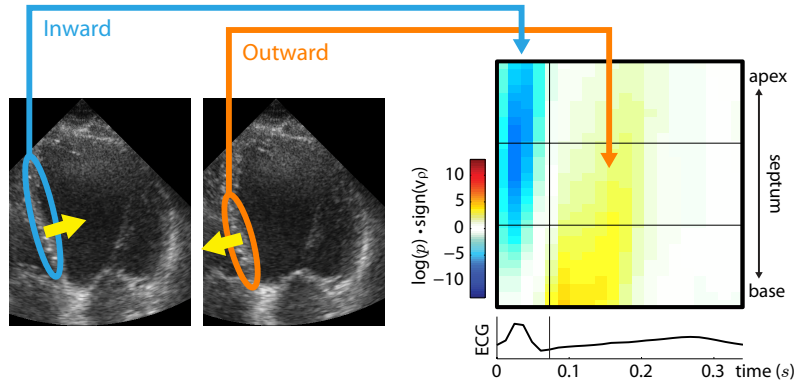


**Figure 5.3:** Map of septal motion abnormalities during systole, for one CRT candidate with SF. The color-scale encodes abnormality ( $p$ -value) in a logarithmic scale, multiplied by the sign of the radial velocity  $v_\rho$  to highlight the inward and outward events of SF.

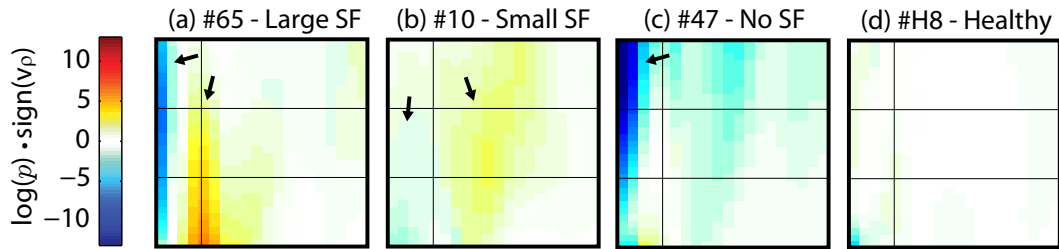


**Figure 5.4:** Abnormality maps for four different subjects: two with SF (top row, arrows indicate the inward and outward events of SF), one with left-right interaction (bottom left), a type of inter-ventricular dyssynchrony [8] where the septum moves passively inward, as indicated by the black arrow, and one healthy volunteer (bottom right).



### Atlas-based comparison to normality

The velocities extracted from each sequence are spatiotemporally synchronized to a common reference anatomy, using ECG matching (time) and local reorientation derived from image registration (multiscale diffeomorphic FFD, [78]) between the first frames of each sequence (space). At each instant of the cardiac cycle and each point of the septum, the velocity vector of each individual is compared to the distribution of velocity vectors for the atlas population at this location, using the Mahalanobis distance. Average and covariance of myocardial velocities over the set of healthy volunteers encode a representation of normal motion. Assuming that the local distribution of velocities for the atlas population is Gaussian, the cumulative function associated to this distribution returns a two-tailed  $p$ -value, low  $p$ -value indicating high degree of abnormality. In contrast, a  $p$ -value close to 1 indicates normal motion.

### Representation of $p$ -value maps of abnormalities

We chose to represent this spatiotemporal information by means of color-coded maps, in which the horizontal axis is time (systole) and the vertical one is the position along the septum (Fig. 5.3). Similar displays, inspired from anatomical M-mode echocardiographic images, were previously used in strain rate imaging [40] or speckle tracking applications [50]. In the current paper, each pixel value corresponds to the  $p$ -value index used to locally

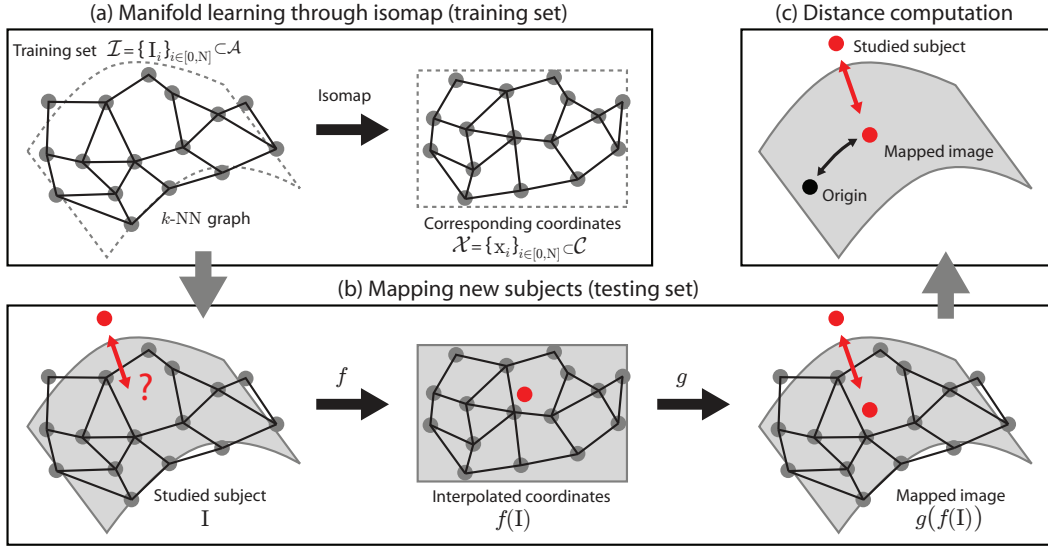


**Figure 5.5:** Pipeline for the method presented in this paper.

encode abnormality, in a logarithmic scale, multiplied by the sign of the radial velocity. The color-code associates blue and red color to highly abnormal inward and outward motion of the septum, respectively. This choice was made to highlight the inward and outward events of SF, in comparison with other patterns of left ventricular dyssynchrony (Fig. 5.4). According to these conventions, the origin used to constrain the manifold (Sec. 5.2.4) is defined as an image having 0 value at every pixel, representing a normal motion pattern.

## 5.2.2 Definition of variables

Each of the abnormality maps described in Sec. 5.2.1 corresponds to one subject in the dataset, and is used as a 2D input image for the manifold learning process. The rationale of manifold learning on maps of statistical significance is discussed in Sec. 5.4.

All the images considered in this paper belong to an ambient space  $\mathcal{A} \subset \mathbb{R}^P$ ,  $P$  being the number of pixels of each image. We denote  $\mathcal{I} = \{\mathbf{I}_0, \dots, \mathbf{I}_N\} \subset \mathcal{A}$  the dataset of  $N + 1$  images used for the manifold estimation. The image  $\mathbf{I}_0$  corresponds to the image origin for normality. This is a synthetic image with 0 value at each pixel, as explained in Sec. 5.2.1. This image is added to the original dataset  $\{\mathbf{I}_1, \dots, \mathbf{I}_N\}$  before any computation. Every image  $\mathbf{I}_i$ ,  $i > 0$  is therefore connected to  $\mathbf{I}_0$  through the isomap graph resulting from the computations described below (Sec. 5.2.3). This amounts to considering every element of  $\mathcal{I}$  as a deviation from the origin along a specific path on the manifold structure.

The coordinate space of the surface estimating the manifold is denoted  $\mathcal{C} \subset \mathbb{R}^M$ ,  $M$  being the estimated dimensionality of the manifold. Note that  $M < N + 1$  due to its estimation from a training set of  $N + 1$  images, this size being lower than  $P$ , the number of pixels of each image. We denote  $f : \mathcal{A} \rightarrow \mathcal{C}$  and  $g : \mathcal{C} \rightarrow \mathcal{A}$  the correspondence functions between  $\mathcal{A}$  and  $\mathcal{C}$ . The computation of these functions is based on interpolation techniques (Sec. 5.2.4), inspired from the concept of principal curves [213].

We preferred to keep notations general for the formulation of our problem, and we denote  $S_{\mathcal{A}} : \mathcal{A} \times \mathcal{A} \rightarrow \mathbb{R}$  and  $S_{\mathcal{C}} : \mathcal{C} \times \mathcal{C} \rightarrow \mathbb{R}$  the metrics used to compare elements of  $\mathcal{A}$  and  $\mathcal{C}$ , respectively. In our implementation, we used the Euclidean distance for both metrics  $S_{\mathcal{A}}$

and  $S_{\mathcal{C}}$ , for both synthetic and CRT datasets, this choice being discussed in Sec. 5.4.

### 5.2.3 Manifold learning through Isomap

The isomap algorithm [153] is used to estimate the manifold (Fig. 5.5a). First, a graph is built for the dataset  $\mathcal{I}$ , based on the  $k$ -NN algorithm, connecting all the images among themselves according to the metric  $S_{\mathcal{A}}$ . The geodesic distance between two points, defined as the shortest path connecting these two points, along the graph, is denoted  $d_{k\text{NN}}$ . Then, Euclidean embedding of this  $k$ -NN connected graph provides a set of coordinates  $\mathcal{X} = \{\mathbf{x}_0, \dots, \mathbf{x}_N\} \subset \mathcal{C}$ .

### 5.2.4 Mapping new patients: from $\mathcal{A}$ to $\mathcal{C}$

The estimation of  $f : \mathcal{A} \rightarrow \mathcal{C}$  is an interpolation problem, which can be re-defined on a reproducible kernel Hilbert space (RKHS) [70, 219, 69, 71]  $\mathcal{F}$  of functions  $\mathcal{A} \rightarrow \mathcal{C}$ . The solution of this problem belongs to a subspace  $\mathcal{F}_{\mathcal{I}} \subset \mathcal{F}$ , where the pairs  $(\mathbf{I}, \mathbf{a}) \in \mathcal{A} \times \mathcal{C}$  are constrained to be located in a specific set  $\mathcal{I} \times \mathcal{X}$ .

In our case,  $\mathcal{I} = \{\mathbf{I}_i\}_{i \in [0, N]}$  is finite-dimensional. As commented in [71],  $\mathcal{F}_{\mathcal{I}}$  is therefore finite-dimensional, and  $f$  can be searched in the closure of the set spanned by the vectors:

$$K_{\mathcal{F}}(\cdot, \mathbf{I}_i) \cdot \mathbf{a}_i, \quad (\mathbf{I}_i, \mathbf{a}_i) \in \mathcal{I} \times \mathcal{C}, \quad (5.1)$$

where  $K_{\mathcal{F}} : \mathcal{A} \times \mathcal{A} \rightarrow \mathbb{M}_{M, M}$  is the reproducible kernel of  $\mathcal{F}$ , and  $\mathbb{M}_{M, M}$  is the set of  $M \times M$ -dimensional real-valued matrices.

The Riesz's representation theorem implies that  $\forall f \in \mathcal{F}, \forall \mathbf{I} \in \mathcal{A}, \forall \mathbf{a} \in \mathcal{C}, \exists K_{\mathcal{F}}^{\mathbf{I}} \in \mathcal{F}$  such that:

$$\langle f(\mathbf{I}), \mathbf{a} \rangle_{\mathbb{R}^M} = \langle K_{\mathcal{F}}^{\mathbf{I}} \cdot \mathbf{a}, f \rangle_{\mathcal{F}}, \quad (5.2)$$

where  $K_{\mathcal{F}}^{\mathbf{I}} = K_{\mathcal{F}}(\mathbf{I}, \cdot)$ .

The interpolation problem can be formulated as an exact or inexact matching problem, depending if we assume that the manifold should pass exactly by the training set, or if we tolerate some dispersion of the data around the manifold.

The choice of the kernel determines the RKHS in which the problem is solved. This point is discussed in App. A.

In the following subsections, we describe the basic formulation of this problem and the improvements made to adapt it to our framework.

#### Exact matching

In case the interpolation is formulated as an exact matching problem, we look for the optimal  $f : \mathcal{A} \rightarrow \mathcal{C}$  passing by all the coordinates  $\mathbf{x}_i \in \mathcal{X}$  at the data points  $\mathbf{I}_i \in \mathcal{I}$ :

$$\begin{cases} \operatorname{argmin}_{f \in \mathcal{F}} \left( \frac{1}{2} \|f\|_{\mathcal{F}}^2 \right), \\ \text{under the constraint } f(\mathbf{I}_i) = \mathbf{x}_i, \quad \forall i \in [0, N]. \end{cases} \quad (5.3)$$

As commented in Sec. 5.2.4 and App. B, the solution for Eq. 5.3 can be written as:

$$\begin{cases} f(\mathbf{I}) = \sum_{i=0}^N K_{\mathcal{F}}(\mathbf{I}, \mathbf{I}_i) \cdot \mathbf{a}_i, \\ \text{with } \mathbf{A} = \mathbf{K}_{\mathcal{A}}^{-1} \cdot \mathbf{X}, \end{cases} \quad (5.4)$$

where:

- $\mathbf{A} = (\mathbf{a}_0, \dots, \mathbf{a}_N)^t \in \mathbb{M}_{N+1, M}$ , with  $\mathbf{a}_i \in \mathcal{C}$  and  $\cdot^t$  the transposition operator,



- $\mathbf{K}_{\mathcal{A}} = (K_{\mathcal{F}}(\mathbf{I}_i, \mathbf{I}_j))_{(i,j) \in [0,N]^2} \in \mathbb{M}_{N+1, N+1}$ ,
- $\mathbf{X} = (\mathbf{x}_0, \dots, \mathbf{x}_N)^t \in \mathbb{M}_{N+1, M}$ .

In this paper, the kernel  $K_{\mathcal{F}}$  is chosen of the exponential form:

$$K_{\mathcal{F}}(\mathbf{I}, \mathbf{J}) = \exp\left(-S_{\mathcal{A}}(\mathbf{I}, \mathbf{J})^2 / \sigma_{\mathcal{F}}^2\right), \quad (5.5)$$

$\sigma_{\mathcal{F}}$  being its bandwidth and  $(\mathbf{I}, \mathbf{J}) \in \mathcal{A}^2$ . The choice of such a function is commented in App. A, while the choice of a relevant bandwidth is discussed in Sec. 5.2.4.

### Inexact matching

In case we tolerate some dispersion of the data around the manifold, the previous interpolation needs to be re-written as an inexact matching problem, now looking for the optimal  $f : \mathcal{A} \rightarrow \mathcal{C}$  best approximating the coordinates  $\mathbf{x}_i \in \mathcal{X}$  at the data points  $\mathbf{I}_i \in \mathcal{I}$ :

$$\operatorname{argmin}_{f \in \mathcal{F}} \left( \frac{1}{2} \|f\|_{\mathcal{F}}^2 + \frac{\gamma_f}{2} \sum_{i=0}^N S_{\mathcal{C}}(f(\mathbf{I}_i), \mathbf{x}_i)^2 \right), \quad (5.6)$$

where  $\gamma_f$  is a weighting coefficient balancing the smoothness of the interpolation and the adherence to the data.

Eq. 5.6 has the following analytical solution:

$$\begin{cases} f(\mathbf{I}) = \sum_{i=0}^N K_{\mathcal{F}}(\mathbf{I}, \mathbf{I}_i) \cdot \mathbf{a}_i, \\ \text{with } \mathbf{A} = (\mathbf{K}_{\mathcal{A}} + \frac{1}{\gamma_f} \mathbf{Id}_{N+1, N+1})^{-1} \cdot \mathbf{X}, \end{cases} \quad (5.7)$$

$\mathbf{Id}_{N+1, N+1}$  being the identity matrix in  $\mathbb{M}_{N+1, N+1}$ .

### Constrained problem

In this paper, the formulation of Eq. 5.6 is adapted to force the interpolation function to pass by the coordinates origin  $\mathbf{x}_0$ :

$$\begin{cases} \operatorname{argmin}_{f \in \mathcal{F}} \left( \frac{1}{2} \|f\|_{\mathcal{F}}^2 + \frac{\gamma_f}{2} \sum_{i=1}^N S_{\mathcal{C}}(f(\mathbf{I}_i), \mathbf{x}_i)^2 \right), \\ \text{under the constraint } f(\mathbf{I}_0) = \mathbf{x}_0. \end{cases} \quad (5.8)$$

The analytical solution for this problem is written as:

$$\begin{cases} f(\mathbf{I}) = \sum_{i=0}^N K_{\mathcal{F}}(\mathbf{I}, \mathbf{I}_i) \cdot \mathbf{a}_i, \\ \text{with } \mathbf{A} = (\mathbf{K}_{\mathcal{A}} + \frac{1}{\gamma_f} \mathbf{M})^{-1} \cdot \mathbf{X}, \end{cases} \quad (5.9)$$

where  $\mathbf{M} = (M_{i,j})_{(i,j) \in [0,N]^2} \in \mathbb{M}_{N+1, N+1}$ , with  $M_{i,i} = 1 \forall i \neq 0$  and 0 otherwise.

With this formulation,

$$\mathbf{x}_i = \sum_{j=0}^N \left( K_{\mathcal{F}}(\mathbf{I}_i, \mathbf{I}_j) + \frac{1}{\gamma_f} M_{i,j} \right) \cdot \mathbf{a}_j. \quad (5.10)$$

Thus,  $\mathbf{x}_0 = \sum_{j=0}^N K_{\mathcal{F}}(\mathbf{I}_0, \mathbf{I}_j) \cdot \mathbf{a}_j$ , which corresponds to the exact matching formulation of Eq. 5.4, meaning that the constraint  $f(\mathbf{I}_0) = \mathbf{x}_0$  is satisfied.

The addition of such a constraint is illustrated in Fig. 5.6, which displays the curve interpolated from a 1D synthetic dataset, using inexact matching, before and after forcing the curve to pass by a given point, as described in Eq. 5.8.

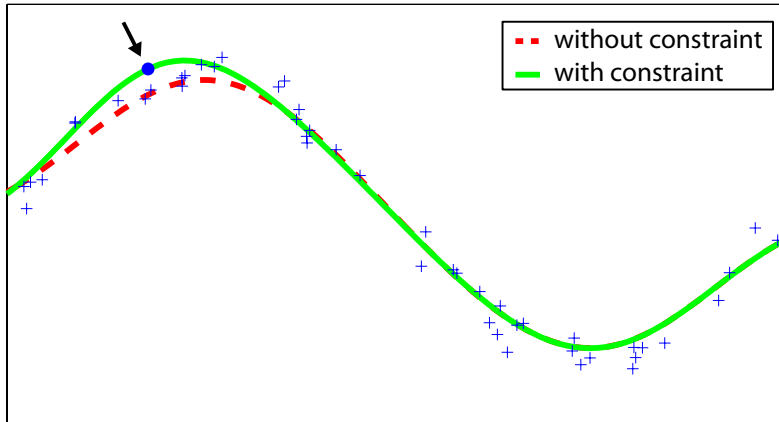


**Figure 5.6:** Interpolation of a 1D synthetic dataset using inexact matching, before and after the addition of a constraint forcing the curve to pass by the point indicated by the black arrow.

### Use of locally adjustable kernel

In the previous formulations, no constraint is made on the kernel bandwidth, which fully conditions the accuracy of the interpolation. Previous works used a fixed bandwidth, defined as average  $k$ -NN distance, namely:

$$\sigma_{\mathcal{F}} = \frac{1}{N+1} \sum_{i=0}^N S_{\mathcal{A}}(\mathbf{I}_i, \text{nn}_k(\mathbf{I}_i)), \quad (5.11)$$

where  $\text{nn}_k(\mathbf{I}_i)$  is the  $k$ th neighbour of  $\mathbf{I}_i$  [217].

In fact, the use of a fixed bandwidth has some limitations in case the points distribution is not uniform, which is our case (Sec. 5.3.1 and 5.3.2). Indeed, a small kernel in a sparse region of the dataset would result in mapping points in this region to zero, or closer to zero than they should. On the contrary, a kernel with a too large bandwidth could result in a too planar interpolation in comparison with the manifold curvature, therefore mapping points far from the manifold structure. Similar concerns were raised in the literature about probabilistic density estimation [220, 221]. The manifold learning algorithm described in [222] used a linear interpolation scheme with equal weights on each neighbourhood, proposing to locally adapt the number of  $k$ -NN to address this issue. In the sequel, we propose to use a varying bandwidth for the interpolation kernel, which is locally adapted depending on the neighbourhood size:

$$\sigma_{\mathcal{F}}(\mathbf{I}) = \frac{1}{K^2} \sum_{k=1}^K \sum_{\substack{l=1 \\ l \neq k}}^K S_{\mathcal{A}}(\text{nn}_k(\mathbf{I}), \text{nn}_l(\mathbf{I})), \quad (5.12)$$

where the right term in the equation is the average distance between the  $K$  nearest neighbours of  $\mathbf{I}$ .

The advantage of using such a varying bandwidth over a formulation with a fixed bandwidth is demonstrated in Sec. 5.3.1.

### 5.2.5 Mapping new patients: from $\mathcal{C}$ to $\mathcal{A}$

The formulation for the estimation of  $g : \mathcal{C} \rightarrow \mathcal{A}$  is similar to the one of  $f : \mathcal{A} \rightarrow \mathcal{C}$ , namely a matching problem on a RKHS  $\mathcal{G}$  of functions  $\mathcal{C} \rightarrow \mathcal{A}$ , equipped with a norm  $\|\cdot\|_{\mathcal{G}}$ :

$$\begin{cases} \operatorname{argmin}_{g \in \mathcal{G}} \left( \frac{1}{2} \|g\|_{\mathcal{G}}^2 + \frac{\gamma_g}{2} \sum_{i=1}^N S_{\mathcal{A}}(g(\mathbf{x}_i), \mathbf{I}_i)^2 \right), \\ \text{under the constraint } g(\mathbf{x}_0) = \mathbf{I}_0, \end{cases} \quad (5.13)$$

where  $\gamma_g$  is a weighting coefficient balancing the smoothness of the interpolation and the adherence to the data.

Eq. 5.13 has the following analytical solution:

$$\begin{cases} g(\mathbf{x}) = \sum_{i=0}^N K_{\mathcal{G}}(\mathbf{x}, \mathbf{x}_i) \cdot \mathbf{b}_i, \\ \text{with } \mathbf{B} = (\mathbf{K}_{\mathcal{C}} + \frac{1}{\gamma_g} \mathbf{M})^{-1} \cdot \mathbf{Y}, \end{cases} \quad (5.14)$$

where:

- $\mathbf{B} = (\mathbf{b}_0, \dots, \mathbf{b}_N)^t \in \mathbb{M}_{N+1, P}$ , with  $\mathbf{b}_i \in \mathcal{A}$ ,
- $\mathbf{K}_{\mathcal{C}} = (K_{\mathcal{G}}(\mathbf{x}_i, \mathbf{x}_j)^2)_{(i,j) \in [0, N]^2} \in \mathbb{M}_{N+1, N+1}$ ,
- and  $\mathbf{Y} = (\mathbf{I}_0, \dots, \mathbf{I}_N)^t \in \mathbb{M}_{N+1, P}$ .

The kernel  $K_{\mathcal{G}}$  is chosen of the exponential form:

$$K_{\mathcal{G}}(\mathbf{x}, \mathbf{y}) = \exp(-S_{\mathcal{C}}(\mathbf{x}, \mathbf{y})^2 / \sigma_{\mathcal{G}}^2), \quad (\mathbf{x}, \mathbf{y}) \in \mathcal{C}^2, \quad (5.15)$$

its bandwidth being defined as:

$$\sigma_{\mathcal{G}}(\mathbf{x}) = \frac{1}{K^2} \sum_{k=1}^K \sum_{\substack{l=1 \\ l \neq k}}^K S_{\mathcal{C}}(\operatorname{nn}_k(\mathbf{x}), \operatorname{nn}_l(\mathbf{x})). \quad (5.16)$$

### 5.2.6 Distance computation

With the previous formulations of the mappings  $f$  and  $g$ , any image  $\mathbf{I} \in \mathcal{A}$  is associated to another image  $\hat{\mathbf{I}}$  belonging to the manifold, by means of the composition of these mappings, using:

$$\hat{\mathbf{I}} = g(f(\mathbf{I})). \quad (5.17)$$

This composition allows defining a distance between any image  $\mathbf{I} \in \mathcal{A}$  and the manifold [217], namely:

$$d_P(\mathbf{I}) = S_{\mathcal{A}}(\hat{\mathbf{I}}, \mathbf{I}). \quad (5.18)$$

This distance is complemented by a second one, which compares individuals to normality along the manifold structure:

$$d_M(\mathbf{I}) = S_{\mathcal{C}}(f(\mathbf{I}), \mathbf{x}_0). \quad (5.19)$$

The relation between these two distances and the total abnormality contained in each map  $\mathbf{I}$ , defined as  $S_{\mathcal{A}}(\mathbf{I}, \mathbf{I}_0)$ , is discussed in App. C.

### 5.2.7 Additional metrics

We used the objective metrics described in [223] to evaluate the quality of the dimensionality reduction, in comparison with linear dimensionality reduction techniques.



## Compactness

Compactness estimates the convergence speed of the dimensionality reduction, namely its ability to represent the studied objects by the very first dimensions. We measure compactness as:

$$C(M) = \frac{1}{\Gamma} \sum_{m=1}^M \lambda_m, \quad (5.20)$$

where  $M$  is the number of retained dimensions for the coordinate space  $\mathcal{C}$ ,  $\lambda_m$  is the eigenvalue corresponding to the  $m$ th dimension, and  $\Gamma = \sum_{m=1}^{N+1} \lambda_m$ .

The eigenvalues for the non-linear dimensionality reduction technique (ML) are obtained from the diagonalization of the  $k$ -NN distance matrix  $\tau(\mathbf{D}) \in \mathbb{M}_{N+1, N+1}$  involved in the isomap process [153], where  $\tau(\mathbf{D}) = -\mathbf{H}\mathbf{D}\mathbf{H}/2$ , with  $\mathbf{D} = (d_{k\text{NN}}(\mathbf{x}_i, \mathbf{x}_j)^2)_{(i,j) \in [0, N]^2}$ , and  $\mathbf{H} = (\delta_{ij} - 1/(N+1))_{(i,j) \in [0, N]^2}$  is a centering operator. Each  $\lambda_m$  is associated to the  $m$ th principal direction along the manifold structure.

The eigenvalues for the linear dimensionality reduction technique (PCA) come from the diagonalization of the covariance matrix computed for the images of the training set  $\mathcal{I}$ . Each  $\lambda_m$  is associated to the  $m$ th principal direction along which the data variance is maximal.

The standard error of  $C(M)$  is defined as:

$$\sigma_C(M) = \frac{1}{\Gamma} \sum_{m=1}^M \sqrt{\frac{2}{N+1}} \lambda_m. \quad (5.21)$$

## Generalization ability

The generalization ability estimates the reconstruction error for points included within the range of noise of the training set. It represents the ability of the method to describe instances outside the training set. Each point in the training set  $\mathbf{I}_i \in \mathcal{I}$  is reconstructed using leave-one-out, namely, estimating the space of reduced dimensionality from the other points in the dataset. This leads to the following reconstruction error:

$$G(\mathbf{I}_i, M) = S_{\mathcal{A}}(\hat{\mathbf{I}}_i^{LVO}, \mathbf{I}_i), \quad (5.22)$$

where  $M$  is the number of retained dimensions, and  $\hat{\mathbf{I}}_i^{LVO}$  is the reconstruction of  $\mathbf{I}_i$  using the reduced set  $\mathcal{T} \setminus \mathbf{I}_i = \{\mathcal{I}_j\}_{j \neq i}$ .

We computed the median, the 1st and 3rd quartiles of  $G(\mathbf{I}_i, M)$  for all  $\mathbf{I}_i \in \mathcal{I}$  to fully characterize the generalization ability, the normality of its distribution not being guaranteed.

Compactness and generalization ability both reflect the amount of variance explained by the model, but these metrics are not redundant. For the compactness, the amount of variance explained depends on the retained eigenvalues, while for the generalization ability it depends on the distribution of the training set.

## Specificity

Specificity characterizes the relevance of objects generated from the low dimensional coordinates, with respect to the training set:

$$S(\mathbf{x}, M) = S_{\mathcal{A}}(g(\mathbf{x}), \text{nn}_1(g(\mathbf{x}))), \quad (5.23)$$

where  $g(\mathbf{x})$  is the image generated from the  $M$ -dimensional coordinate  $\mathbf{x}$ , and  $\text{nn}_1(g(\mathbf{x}))$  is its first nearest neighbour.



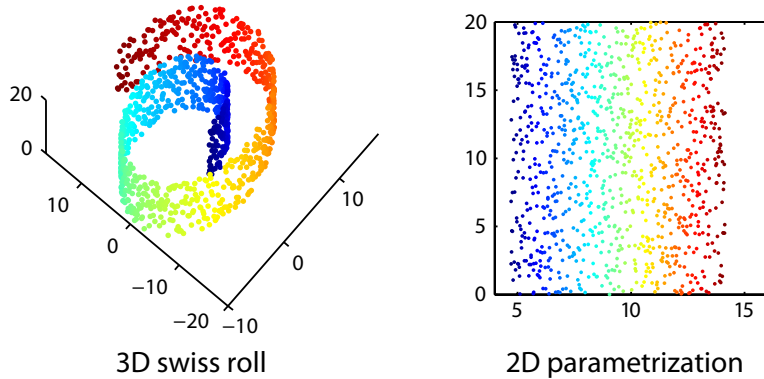


**Figure 5.7:** 3D swiss roll and 2D random distribution of points used as 2D parametrization for its construction.

We computed the median, the 1st and 3rd quartiles of  $S(\mathbf{x}, M)$  over a set of randomly generated coordinates  $\mathbf{x}$  to fully characterize the specificity, the normality of its distribution not being guaranteed.

## 5.3 Experiments

In the sequel, we detail the experiments designed for tuning the parameters of our method, namely: the manifold dimensionality, the number of  $k$ -NN, the bandwidth of the interpolation kernels, and the inexact matching weights  $\gamma_f$  and  $\gamma_g$ . We first use a synthetic dataset to understand the behaviour of some specific parameters. Then, these parameters are tuned for a real dataset of CRT candidates. The algorithm with optimal values is finally applied to compare a set of individuals to a specific population.

### 5.3.1 Parameter tuning - Synthetic data

We created a three dimensional dataset of 1000 points, arranged according to a 2D structure in the 3D space (swiss roll, Fig. 5.7), defined as:

$$\begin{cases} I_{i,1} = \cos(3\pi/2 \cdot (1 + 2x_{i,1})), \\ I_{i,2} = \sin(3\pi/2 \cdot (1 + 2x_{i,2})), \\ I_{i,3} = x_{i,2} \in [0, 20], \end{cases} \quad (5.24)$$

$(I_{i,1}, I_{i,2}, I_{i,3}) = \mathbf{I}_i$  referring to a point in the 3D space, obtained from the coordinate  $(x_{i,1}^{GT}, x_{i,2}^{GT}) = \mathbf{x}_i^{GT}$ , randomly generated from a uniform distribution. In the following, we denote  $g^{GT} : \mathcal{C} \rightarrow \mathcal{A}$  the parametrization function allowing the generation of points in the 3D space from ground truth coordinates, and Eq. 5.24 can be rewritten as  $\mathbf{I}_i = g^{GT}(\mathbf{x}_i^{GT})$ .

For this synthetic dataset, the Euclidean distance  $\|\cdot\|$  was used for both metrics  $S_{\mathcal{A}}$  and  $S_{\mathcal{C}}$ .

#### Number of $k$ -NN

The output from the isomap algorithm is a low-dimensional approximation of a Riemannian space. We used the metric described in [224] to estimate the quality of this approximation.

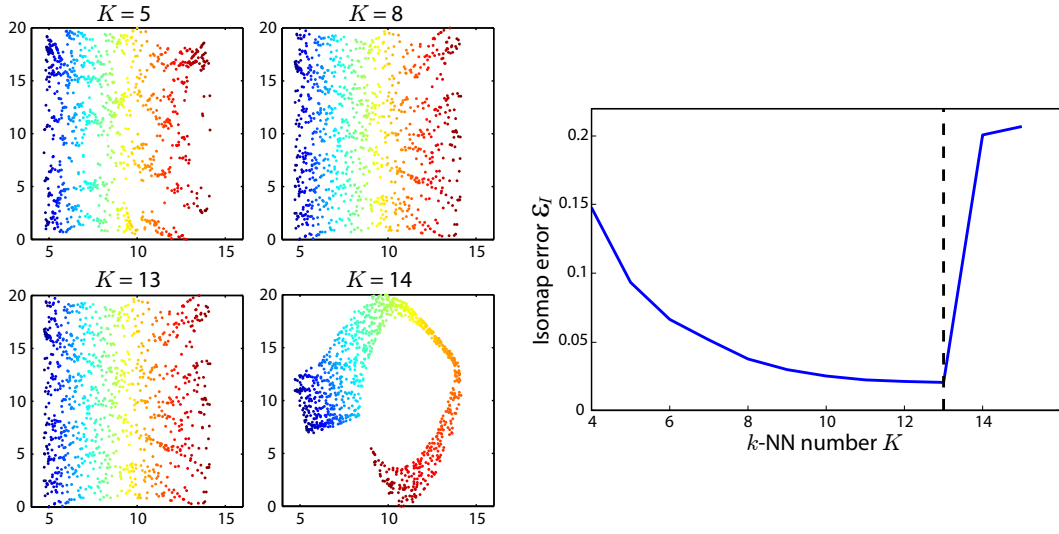


**Figure 5.8:** Influence of the number of  $k$ -NN on the isomap output, for the 3D swiss roll data. Top: isomap output for  $K = \{5, 8, 13, 14\}$ . Bottom: evolution of the isomap error  $\epsilon_I$  (Eq. 5.25) with the number of  $k$ -NN. Mean error over all the pairs  $(\mathbf{x}_i, \mathbf{x}_j) \in \mathcal{X}^2$ . A jump is present on this curve for  $K = 14$ , reflecting the apparition of a short-circuit in the  $k$ -NN graph.

The error in the approximation of the path between two coordinates  $(\mathbf{x}_i, \mathbf{x}_j) \in \mathcal{X}^2$  is defined as the relative difference between the geodesic distance  $d_{k\text{NN}}$ , and the distance defined by  $S_C$ :

$$\epsilon_I(\mathbf{x}_i, \mathbf{x}_j) = 1 - \frac{S_C(\mathbf{x}_i, \mathbf{x}_j)}{d_{k\text{NN}}(\mathbf{x}_i, \mathbf{x}_j)}. \quad (5.25)$$

We evaluated the influence of the number of  $k$ -NN on the isomap output using this error. The experiment is illustrated in Fig. 5.8, and displays the mean error over all the pairs  $(\mathbf{x}_i, \mathbf{x}_j) \in \mathcal{X}^2$ . When the number of  $k$ -NN increases, the 2D distribution of points estimated by the isomap algorithm gets closer to the 2D parametrization used for building the swiss roll, until a short-circuit appears for  $K = 14$ , visible both in the curve representing the isomap error  $\epsilon_I$  and in the subfigure of the isomap output. The optimal number of  $k$ -NN for this dataset is therefore  $K = 13$ .

The error  $\epsilon_I$  could also be used for parameter tuning in case the dimensionality  $M$  is unknown (Sec. 5.3.2), but this strategy may not be optimal to assess the presence or absence of a short-circuit, in particular if the number of samples in the training set is low. We adapted the measurement of node flow on a graph [225] to assess the apparition of a short-circuit in the  $k$ -NN graph. We first defined the flow of a given edge  $F_{\text{edge}}(\text{edge}_{\mathbf{x}_i \rightarrow \mathbf{x}_j})$  as the number of shortest paths  $(\text{path}_{\mathbf{x}_r \rightarrow \mathbf{x}_s})_{(r,s) \in [0,N]^2}$  of the graph passing on the edge. The total flow at a node  $\mathbf{x}_i \in \mathcal{X}$  is therefore defined as:

$$F_{\text{node}}(\mathbf{x}_i) = \sum_{k=1}^K F_{\text{edge}}(\text{edge}_{\mathbf{x}_i \rightarrow \text{nn}_k(\mathbf{x}_i)}). \quad (5.26)$$

The node flow reflects the spatial arrangement of the nodes of the graph, conditioned by the number of  $k$ -NN used. Optimal  $K$  should minimize  $\epsilon_I$  within the spatial domain occupied by the nodes of the graph. The uniformity of the spatial arrangement of the nodes ( $K$  being set to its optimal value) leads to the uniformity of the node flow distribution. In

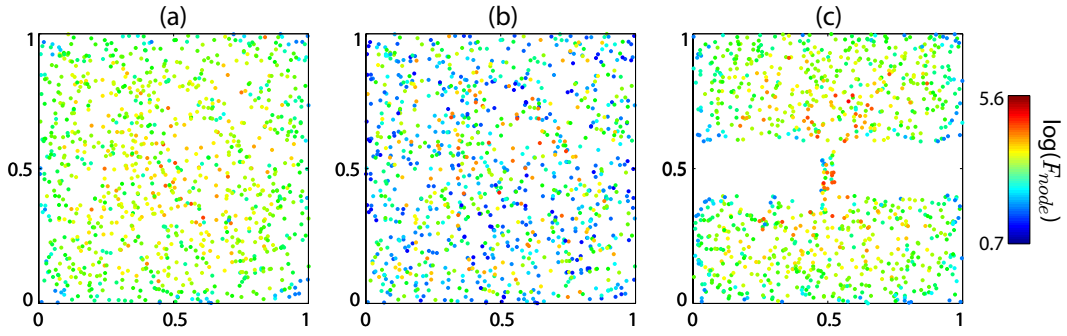


**Figure 5.9:** Influence of the graph number of  $k$ -NN and the spatial arrangement of the graph nodes on the the node flow distribution. Synthetic dataset of 1000 points within a given spatial domain. (a) Initial spatial domain with  $K = 20$ . (b) Same spatial domain with  $K = 5$ . Large local variations of the node flow are locally observed, reflecting a too low connectivity within the graph. (c) Modified spatial domain with  $K = 20$ . Node flow is higher where the spatial domain is narrow, reflecting that a large number of shortest paths along the graph pass within this region.

the absence of short-circuit, the local density of the graph and local variations of the spatial domain occupied by the nodes of the graph may change the node flow locally (Fig. 5.9). The evolution of the node flow distribution with the number of  $k$ -NN, for all the points of the  $k$ -NN graph, is shown in Fig. 5.10. Low variability of the node flow distribution is observed when the estimated coordinates  $\mathbf{x}_i$  tend to be uniformly distributed ( $K$  getting closer to 13). Note that the points on the border of the graph have slightly lower node flow, due to a lower probability that a shortest path passes by these points. When a short-circuit appears at a

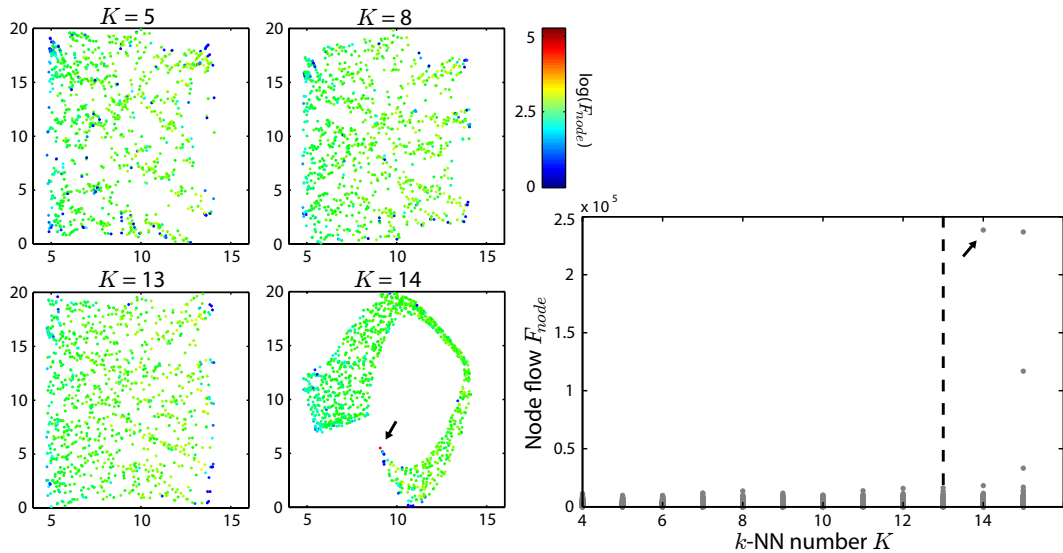


**Figure 5.10:** Influence of the number of  $k$ -NN on the node flow, for the 3D swiss roll data. Top: isomap output for  $K = \{5, 8, 13, 14\}$ , where each node is colored according to its flow (Eq. 5.26). For all points, the variability of the flow distribution is low when  $K \leq 13$ , while the apparition of a short-circuit for  $K = 14$  makes one specific point having almost the highest flow possible (black arrow). Bottom: evolution of the node flow distribution with the number of  $k$ -NN. Black arrow indicates the value of the node flow for the point where the short-circuit appears.

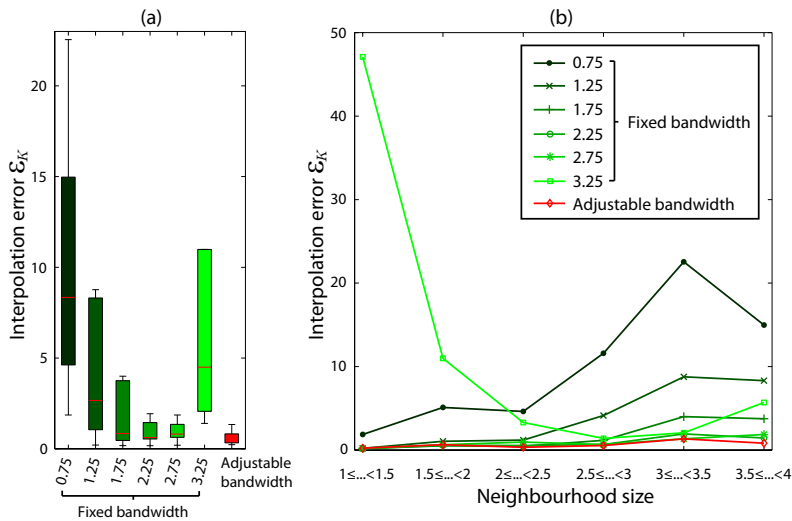


**Figure 5.11:** Comparison of locally adjustable kernel (red) and fixed bandwidth kernels (green levels) in terms of interpolation error  $\epsilon_K$  (Eq. 5.28), for 100 testing points belonging to the swiss roll, generated using Eq. 5.24. (a) Median and 1st/3rd quartiles for each kernel size. (b) Median of the interpolation error  $\epsilon_K$  for the points within a given interval of neighbourhood size (right term in Eq. 5.12), highlighting the accuracy of the locally adjustable kernel for each type of neighbourhood.

specific point ( $K = 14$ , black arrow), a majority of the shortest paths pass by this point, which has therefore a much higher node flow.

### Varying kernel

The accuracy of an interpolation based on a locally adjustable kernel (Sec. 5.2.4) was compared to the one of kernels with fixed bandwidth. We first generated a testing set of 100 points belonging to the swiss roll (note that these points are different from the already existing set of 1000 points generated in Sec. 5.3.1), as follows:

1. We first generated 100 ground truth coordinates  $\mathbf{x}^{GT}$ , randomly obtained from a uniform distribution.
2. For each ground truth coordinate, we computed the weighted center of mass of its neighbourhood:

$$W(\mathbf{x}^{GT}, \mathbf{p}) = \sum_{k=1}^K p_k \cdot \text{nn}_k(\mathbf{x}^{GT}), \quad (5.27)$$

where  $\mathbf{p}$  is a vector of weights  $p_k$ , randomly generated for each coordinate  $\mathbf{x}^{GT}$  from a uniform distribution, such that  $\sum_{k=1}^K p_k = 1$ .

3. Finally, we computed the point on the swiss roll associated to this center of mass, using the parametrization described in Sec. 5.3.1, namely:  $\mathbf{I} = g^{GT}(W(\mathbf{x}^{GT}, \mathbf{p}))$ .

The kernel interpolation is accurate if the point  $\mathbf{I} = g^{GT}(W(\mathbf{x}^{GT}, \mathbf{p}))$  is mapped to the weighted center of mass of the coordinates  $f(\text{nn}_k(\mathbf{I}))$ , with the same weights  $p_k$ . We defined the interpolation error as:

$$\epsilon_K(\mathbf{I}) = S_C \left( f(\mathbf{I}), \sum_{k=1}^K p_k f(\text{nn}_k(\mathbf{I})) \right). \quad (5.28)$$

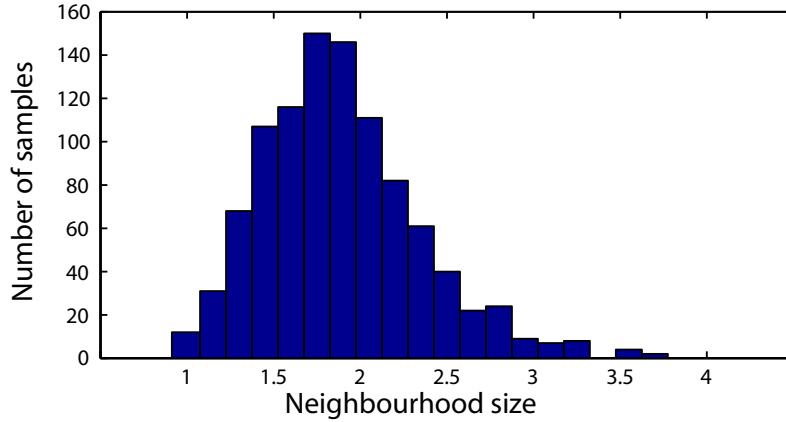


**Figure 5.12:** Histogram of the distribution of neighbourhood sizes (right term in Eq. 5.12) for the 3D swiss roll dataset. Non-uniformity in the data distribution supports the use of a kernel with varying bandwidth for this dataset.

The median and 1st/3rd quartiles of the interpolation error  $\epsilon_K$  over the generated set of 100 points, for each kernel size, is represented in Fig. 5.11a, and is complemented by Fig. 5.11b, representing the median of the interpolation error  $\epsilon_K$  for the points within a given interval of neighbourhood size (right term in Eq. 5.12). As commented in Sec. 5.2.4, small kernels (dark green) introduce more errors for large neighbourhoods, while on the contrary, larger kernels (light green) are less accurate for small neighbourhoods. In contrast, the proposed kernel (red) with adjustable bandwidth results in an accurate interpolation for any neighbourhood size. The performance of kernels with fixed bandwidth of 2.25 and 2.75 is very similar, probably as a consequence of this specific dataset (100 randomly selected points, using randomly generated testing weights  $p_k$ ).

The relevance of using a kernel with varying bandwidth depends on the extent of non-uniformity in the data distribution. This was assessed by representing the histogram of the distribution of neighbourhood sizes (right term in Eq. 5.12) over the studied dataset, which supports the use of such a kernel (Fig. 5.12).

### 5.3.2 Parameter tuning - CRT data

#### Dataset description

Using the method presented in Sec. 5.2.3, a manifold was estimated from a population of 50 CRT candidates with SF. This manifold is expected to represent pathological deviations from normal motion, each point of the manifold being a SF pattern. The parameter optimization described in the following sections was performed on this population. Justifications about the size of this population are given in Sec. 5.3.2. Note that this number is conditioned by the number of patients undergoing CRT in the hospital from which the data was collected (Hospital Clínic, Barcelona, Spain), and among them, by the presence of SF for these patients (generally half of the population undergoing CRT). As a comparison, the clinical study of [8], which motivated our approach, considered a population of 161 patients, 87 of which had SF.

A second population was used for testing the distances proposed in Sec. 5.2.6, as described in Sec. 5.3.3. This population was made of 37 CRT candidates (6 having SF and 31 without SF) and 21 healthy volunteers. All patient data was acquired before the implantation of the

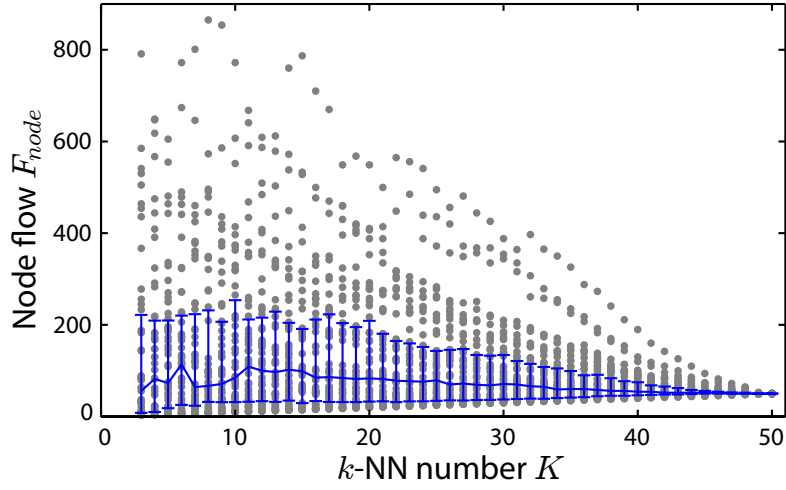


**Figure 5.13:** Evolution of the node flow distribution with the number of  $k$ -NN. Blue errorbars represent the median and 1st/3rd quartiles over the training set of CRT candidates with SF.

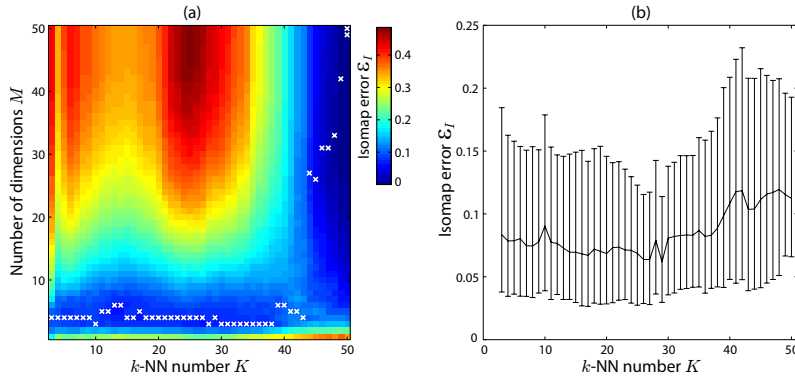


**Figure 5.14:** (a) Evolution of the isomap error  $\epsilon_I$  with the dimensionality  $M$  and the number of  $k$ -NN, for the training set of CRT candidates with SF. White crosses indicate the minimum value of  $\epsilon_I$  for each value of  $k$ -NN. (b) Evolution of the isomap error  $\epsilon_I$  with the number of  $k$ -NN, for  $M = 4$ .



CRT device. The presence of SF was assessed by two experienced cardiologists, from the visual inspection of echocardiographic M-mode images, as described in [8].

A 2D spatiotemporal map of myocardial motion abnormalities obtained from a statistical atlas of motion [83] was associated to each subject, as explained in Sec. 5.2.1. The atlas was built from the set of 21 healthy volunteers. Abnormality maps for the set of volunteers used for the atlas construction were computed using leave-one-out on this population. The abnormality maps had a size of  $20 \times 31$  pixels, corresponding to the sampling of the systolic period (horizontal dimension) and the septum along its medial line (vertical dimension), respectively.

For this dataset, the Euclidean distance  $\|\cdot\|$  was used for both metrics  $S_A$  and  $S_C$ . The choice of this distance for  $S_A$  is discussed in Sec. 5.4. This distance was used for the metric  $S_C : \mathcal{C} \rightarrow \mathbb{R}$  due to the Euclidean embedding of the coordinate space provided by the isomap algorithm (Sec. 5.2.3).

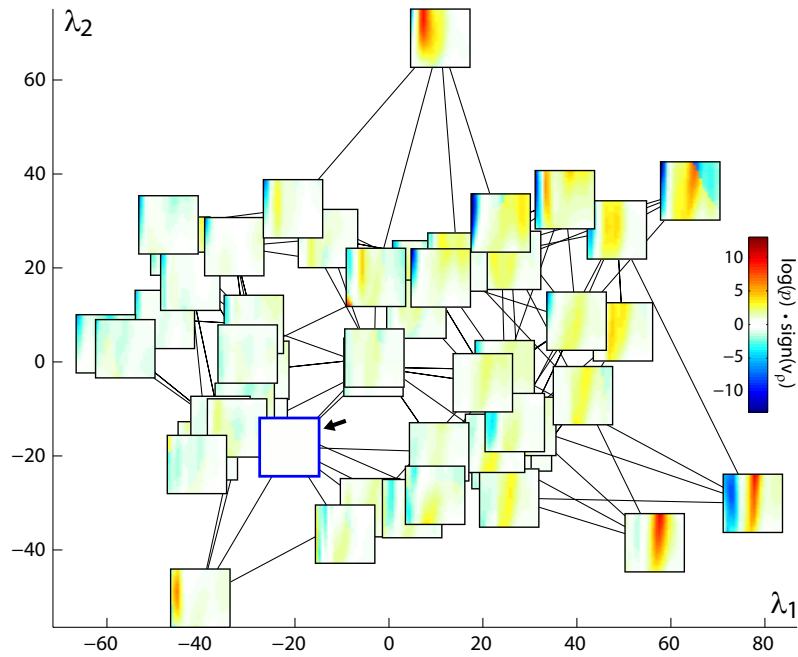


**Figure 5.15:** 2D embedding of the manifold of SF  $p$ -value maps (output of isomap) according to its two first dimensions. The black arrow indicates the origin image used to constrain the manifold, representing a normal motion pattern.

### Dimensionality reduction and $k$ -NN

An overview of methods for estimating the intrinsic dimensionality of a dataset was given in [226], but there is no standard manner of performing this step. For the CRT dataset, both optimal dimensionality and number of  $k$ -NN were unknown, and were determined using the same experimental design as in Sec. 5.3.1.

We first computed the evolution of the node flow distribution (Eq. 5.26) with the number of  $k$ -NN, as represented in Fig. 5.13. Note that this measurement is directly performed on the  $k$ -NN graph, before the dimensionality reduction step, and is therefore independent of the retained dimensionality  $M$ . No jump in the node flow distribution was observed when the number of  $k$ -NN increased, meaning that no short-circuit had been introduced. We therefore chose the dimensionality looking at the value of  $M$  minimizing the isomap error  $\epsilon_I$  for each value of  $K$  (white crosses on Fig. 5.14a), taking its median value as final value for  $M$ . Then, we determined the value of  $K$  from the evolution of  $\epsilon_I$  with the number of  $k$ -NN, when  $M$  is set to its optimal value (Fig. 5.14b). According to this experiment, we set  $M = 4$  and  $K = 5$ , as hardly any influence on  $\epsilon_I$  is observed for values of  $K < 30$ , and high values of  $K$  represent a substantial increase in terms of computational time.

A 2D embedding of the computed manifold (output of isomap) is represented in Fig. 5.15 for illustration purposes, showing the link in the coordinate space between each image and its nearest neighbours. We can qualitatively observe that subjects are arranged in the 2D space according to the pattern present on the map. In particular, subjects with high abnormal motion patterns are located on the border zone of the graph, while the closest subjects to normality are located at the center. However, further investigation is required to determine which characteristic of the SF abnormality pattern (e.g. magnitude, temporal location or spread, spatial location or spread, etc.) is modeled by each of the principal directions of the

manifold dataset, as also observed in Fig. 5.22.

### Kernel bandwidth

We used a locally adjustable kernel for the interpolation performed by  $f : \mathcal{A} \rightarrow \mathcal{C}$  and  $g : \mathcal{C} \rightarrow \mathcal{A}$ , as described in Sec. 5.2.4. The relevance of using such a kernel for the CRT dataset is illustrated in Fig. 5.16, through the histogram of the distribution of neighbourhood sizes, similarly to the experiment performed in Fig. 5.12 for the synthetic dataset. The accuracy of such a kernel, in comparison with kernels of fixed bandwidth, was already demonstrated on synthetic data (Sec. 5.3.1). This experiment cannot be repeated for the CRT dataset due to the lack of ground truth parametrization of the manifold.

### Weighting the closeness to the data

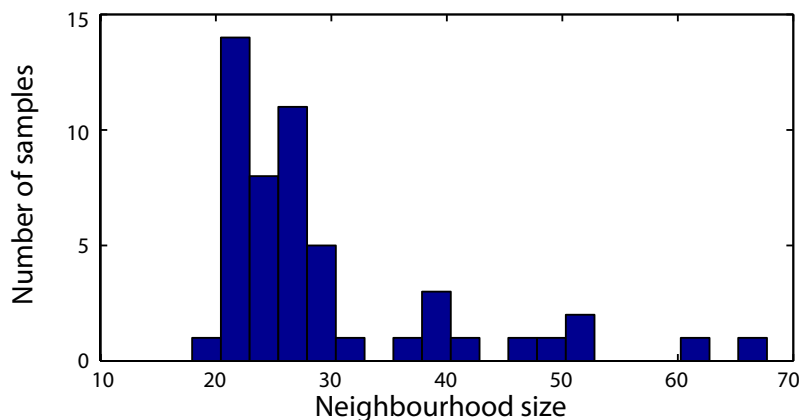
The generalization ability metric (Sec. 5.2.7) was used to determine the optimal values of the weighting terms  $\gamma_f$  and  $\gamma_g$  in Eq. 5.8 and 5.13, respectively. Both weights were determined jointly, as illustrated in Fig. 5.17. Optimal values were those that minimized the median generalization ability. These values were found to be  $\log(\gamma_f) = 1$  and  $\log(\gamma_g) = 0.5$  for our dataset.

Fig. 5.18 represents the reconstruction of five patients from the training set (using leave-one-out), for the optimal values of  $\gamma_f$  and  $\gamma_g$ .

### Performance of the dimensionality reduction

We used the objective metrics described in Sec. 5.2.7 to evaluate the performance of the non-linear dimensionality reduction technique (manifold learning, ML) we used, in comparison with a linear technique (PCA). This comparison is presented in Fig. 5.19.

Note that in PCA and ML methods, the eigenvalues used for the estimation of compactness correspond to different objects (comparison of images using the Euclidean distance [linear case] or the geodesic distances [Isomap]). This limits the value of comparing the PCA and ML methods in terms of compactness, despite the fact that compactness is a normalized measure (Eq. 5.20).



**Figure 5.16:** Histogram of the distribution of neighbourhood sizes (right term in Eq. 5.12) for the training set of CRT candidates with SF. Non-uniformity in the data distribution supports the use of a kernel with varying bandwidth for this dataset.



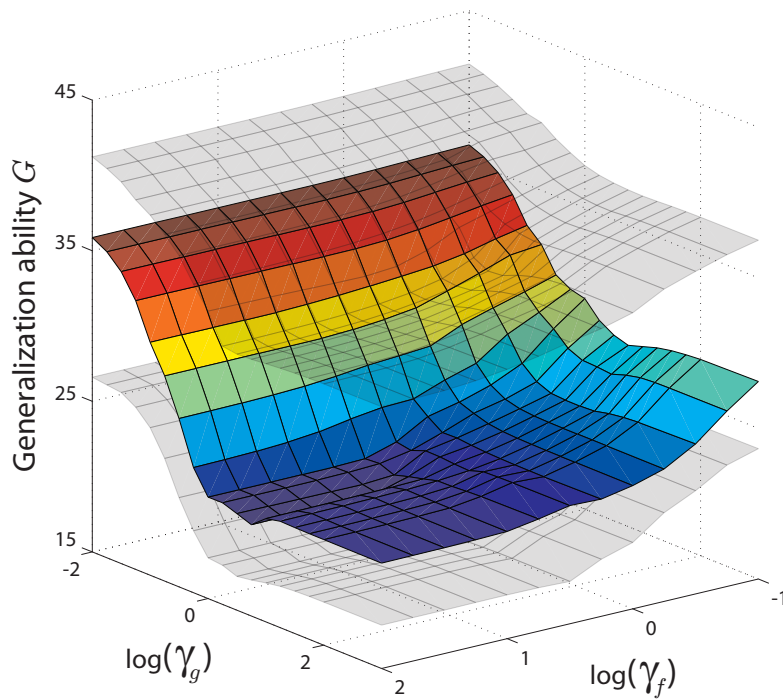


**Figure 5.17:** Generalization ability in function of the weighting terms  $\gamma_f$  and  $\gamma_g$ . Median value (color) and 1st/3rd quartiles (gray) over the training set of CRT candidates with SF.

The results in Fig. 5.19 indicate that the PCA approach is more compact than the ML one, and has a lower generalization ability and higher specificity. We provide in the following some elements of interpretation of these results. Main concerns are (1) the relevance of using non-linear techniques to estimate the manifold structure, and (2) preventing from over-fitting.

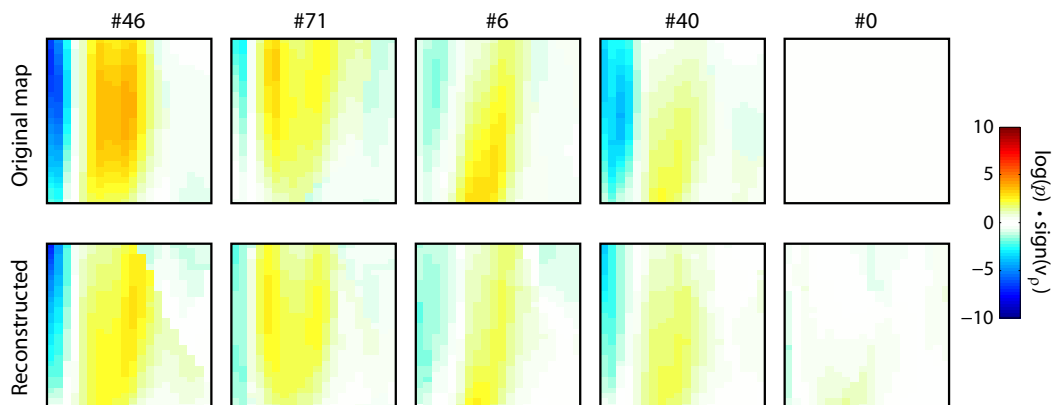
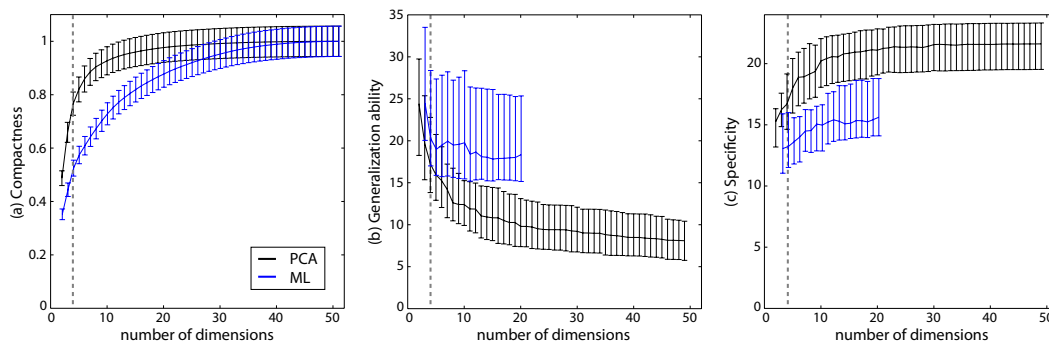


**Figure 5.18:** Reconstruction of five patients from the training set of CRT candidates with SF (using leave-one-out), for the optimal values of  $\gamma_f$  and  $\gamma_g$ .



	ML	PCA	<i>p</i> -value
Compactness	$0.52 \pm 0.03$	$0.77 \pm 0.04$	0.000 <sup>†</sup>
Generalization ability	20.27(17.01 – 28.37)	17.26(13.83 – 22.78)	0.011 <sup>‡</sup>
Specificity	13.23(11.52 – 16.00)	16.71(14.63 – 19.16)	0.000 <sup>‡</sup>

<sup>†</sup> unpaired Student’s *t*-test; <sup>‡</sup> Mann-Whitney *U*-test.

**Figure 5.19:** Comparison between non-linear (ML) and linear (PCA) dimensionality reduction techniques using the objective metrics described in Sec. 5.2.7. Mean  $\pm$  standard deviation (compactness) or median and 1st/3rd quartiles (generalization ability and specificity) over the training set of CRT candidates with SF. Generalization ability and specificity experiments were performed up to  $M = 20$  due to the poor relevance of using ML for  $M > 20$  (Fig. 5.14). Vertical dashed line indicates the retained dimensionality  $M = 4$ . Top: Values for a range of dimensions. Optimal values for  $\gamma_f$  and  $\gamma_g$  were determined for each tested dimensionality using the framework of Sec. 5.3.2 (ML case). Bottom: Values for the retained dimensionality  $M = 4$ . Unpaired Student’s *t*-test (a) and Mann-Whitney *U*-test (b) were used for inter-groups comparison (last column), depending if normal distribution of the values can be assumed or not.

*Relevance of using a non-linear model* First, consider the dataset represented in Fig. 5.20. When computing the generalization ability, one sample is removed (black dot), and the ability of the model to reconstruct it measured. In the ML case (left), this reconstruction will be affected by the changes in the local structure of the estimated manifold (dashed line) induced by the leave-one-out process. In contrast, few changes are expected on the PCA coordinates if such a point is left out. The generalization ability will therefore have lower values in the PCA case.

Now, consider the dataset represented in Fig. 5.21. When computing the specificity, synthetic data is generated from the manifold coordinates, and their closeness to the training set is measured. Points generated from the model coordinates (black dots #1, #2 and #3) will still be close from the training set (red dots) in the non-linear case (left), while nothing prevents them to be far from it in the linear case (right). The specificity will therefore have higher values in the PCA case.

These illustrative examples may help interpreting the values obtained in Fig. 5.19, but nothing guarantees that the manifold estimated for the SF patients has a structure similar as the one represented in Fig. 5.20 and 5.21.

The experiment illustrated in Fig. 5.22 goes in the direction of the above interpretation. It represents synthetic images generated from the model coordinates (progressive deviations from the map used as origin for normality  $\mathbf{I}_0$ , along the two first principal directions of the manifold dataset  $\mathcal{I}$ ), obtained using either PCA or ML. As indicated by the black arrows, PCA does not guarantee that the computed maps still contain the characteristic inward and outward events of SF, while this pattern is preserved by the use of ML. This supports the relevance of using non-linear techniques to estimate the manifold structure.

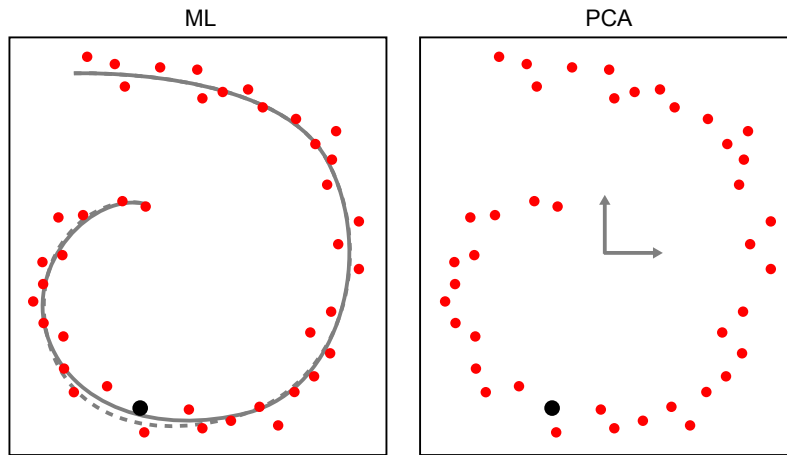


**Figure 5.20:** Influence of the removal of one sample (black dot) on the ability of the model to reconstruct the training set (red dots).

*Prevention of over-fitting* An over-fitting model has bad generalization ability (high values for  $G(\mathbf{I}_i, M)$ ), and good specificity (low values of  $S(\mathbf{x}, M)$ ). The results of Fig. 5.19 may raise the possibility that our model is over-fitting (higher generalization and lower specificity for the ML method, compared to PCA). However, the experiment illustrated in Fig. 5.17 aimed at determining the optimal weights  $\gamma_f$  and  $\gamma_g$  to fit to the data, optimality being associated to the lowest generalization ability values. This limits over-fitting, which would correspond to high values of this metric.

*Size of the training population* To justify that the subject comparison is not biased due to the size of the training population ( $N = 50 + 1$  synthetic image), we computed the evolution of the distances  $d_M$  and  $d_P$  for a training population made of  $N_s < N$  patients. This experiment is summarized in Fig. 5.23. Little variation was observed for the learning

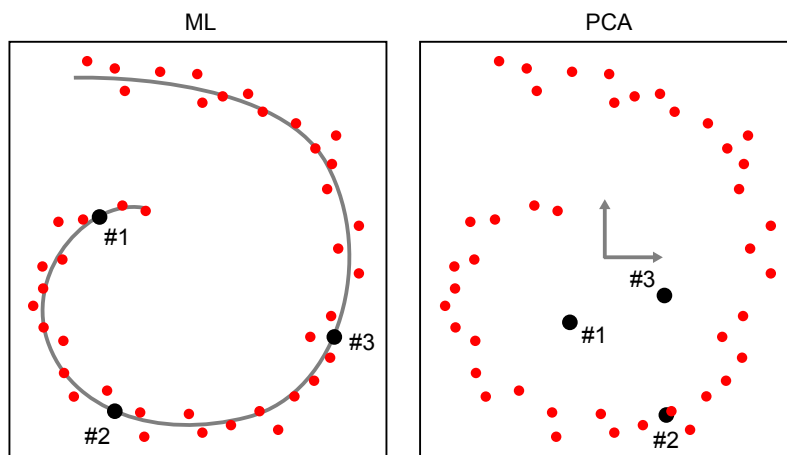


**Figure 5.21:** Comparison of three points generated from the model coordinates (black dots #1, #2 and #3) to the training set (red dots).

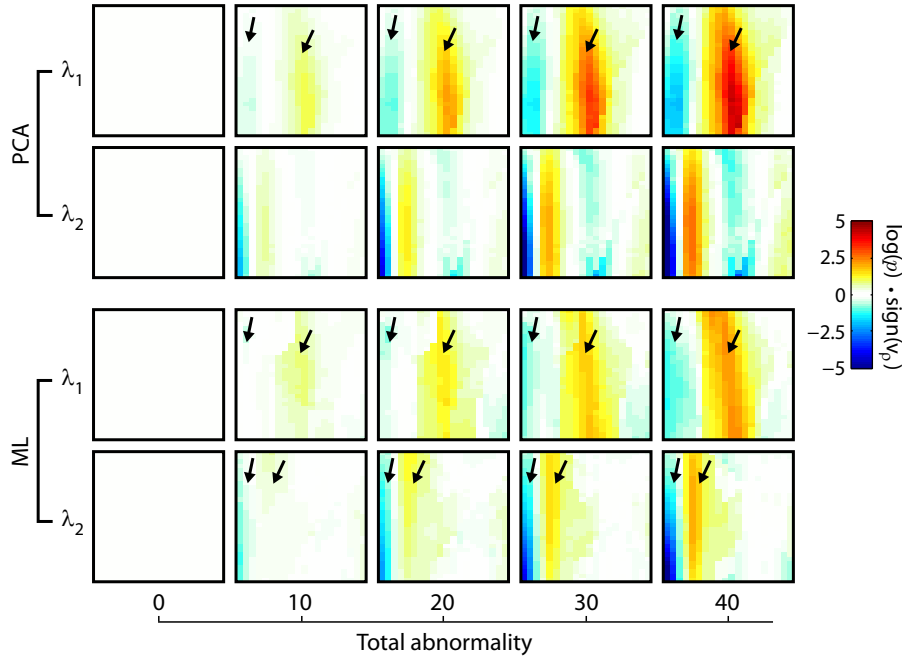


**Figure 5.22:** Progressive deviations from the map used as origin for normality  $\mathbf{I}_0$ , along the two first principal directions of the manifold dataset  $\mathcal{X}$ , obtained using either PCA or manifold learning (ML). Arrows indicate the characteristic inward and outward motion events of SF. Total abnormality is defined as  $S_{\mathcal{A}}(\mathbf{I}, \mathbf{I}_0)$  (Sec. 5.2.6).



parameters ( $M$ ,  $K$ ,  $\gamma_f$  and  $\gamma_g$ ) with training population sizes  $30 \geq N_s \geq 50$ , and we kept for this experiment the parameters estimated for  $N_s = N$ . Curves were normalized against the value obtained for the largest training population, so that the evolution is represented in the same magnitude scale (%). The plot on the top represents this evolution for one subject of each tested population. For each value of  $N_s < N$ , the experiment was repeated for 100 random combinations of  $N_s$  subjects (vertical error bars). For each tested population and each distance ( $d_M$  and  $d_P$ ), the number of subjects above which this evolution stabilizes to its final value  $\pm 5\%$  is summarized in the table of Fig. 5.23 (average  $\pm$  standard deviation values over each tested population). Based on this convergence, we can reasonably trust a manifold estimation with the 50 patients of the training population.

### 5.3.3 Patient analysis - CRT data

Fig. 5.24a represents the distance between all the subjects involved in this study and the manifold. We separated the analysis between  $d_M$  and  $d_P$  for interpretation purposes. The patients from the training set have low  $d_P$  (distance to the manifold), which corresponds to the reconstruction error inherent to the estimation of  $f$  and  $g$  using an inexact matching formulation (Eq. 5.8 and 5.13), and largely span the space associated to  $d_M$  (distance to normality along the manifold). As the training population size is finite, the density in the space of coordinates around patients with the most abnormal patterns is lower, and these patients have higher reconstruction error, namely higher  $d_P$ . Few patients from the training set are close to the origin according to  $d_M$ , in comparison with the healthy volunteers. This may come from the accuracy of the patient selection process using M-mode images [8], small

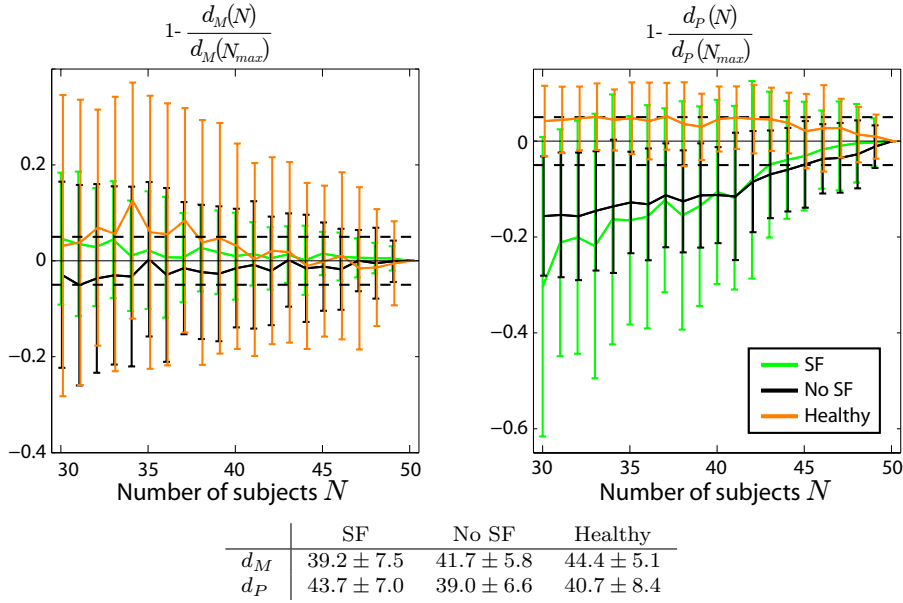


**Figure 5.23:** Top: Normalized evolution of the distances  $d_M$  and  $d_P$  for each subject of each tested population, versus the size of the training population (number of SF patients). Error bars represent the standard deviation over 100 random combinations of  $N_s < N$  subjects. Bottom: values above which this evolution stabilizes to its final value  $\pm 5\%$  (dashed line). Average  $\pm$  standard deviation values over each tested population.

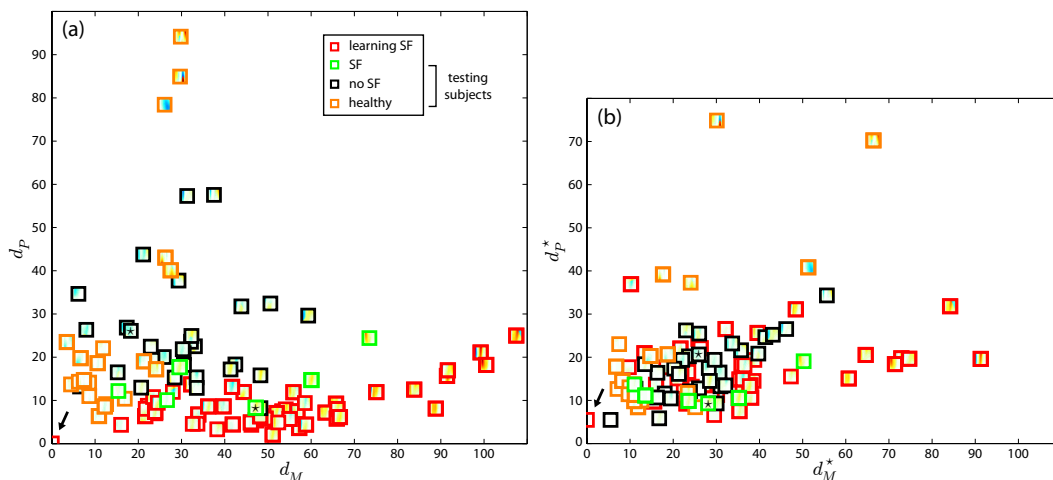
SF being harder to identify, and from the accuracy of the abnormality maps to detect low abnormalities [83]. Among the testing subjects, patients having SF are closer to the manifold than patients without SF, according to  $d_P$ , and almost within the range of the reconstruction error for the training set. Higher values of  $d_M$  are observed in the subjects having higher SF abnormalities on the maps. Large values of  $d_P$  can be observed for some volunteers. These subjects actually have high velocities during the cardiac cycle, reflected by high values of abnormality on their associated 2D maps. Their pattern of motion abnormality cannot be accurately reconstructed from the training population, which does not include any healthy subject. Thus, their corresponding image on the manifold  $\hat{\mathbf{I}}$  tends to be close to  $\mathbf{I}_0$ , resulting in a low  $d_M$  and a high  $d_P$ .

Fig. 5.24b uses a similar display to represent the ordering of subjects obtained using PCA, separating the analysis between  $d_M^*$  and  $d_P^*$ , defined as:

$$\begin{cases} d_P^*(\mathbf{I}) = S_{\mathcal{A}}(\hat{\mathbf{I}}^*, \mathbf{I}), \\ d_M^*(\mathbf{I}) = S_{\mathcal{C}}(\mathbf{x}^*, \mathbf{x}_0^*), \end{cases} \quad (5.29)$$

where  $\hat{\mathbf{I}}^*$  is the reconstruction of  $\mathbf{I}$  using the first  $M$  principal directions obtained from PCA, and  $\mathbf{x}^*$  are the  $M$ -dimensional coordinates of  $\mathbf{I}$  in the PCA space.

This figure highlights the limitations of PCA to perform patient comparison to a population with a specific abnormal pattern. Little discrimination is observed between the healthy volunteers, the testing patients having SF, and patients without SF. Both patients with and without SF appear equally distant from the SF training set according to  $d_P^*$ , and volunteers do not have necessarily low values of  $d_M^*$ . The PCA-based approach therefore does not guarantee that our main objectives for CRT studies (characterizing patients according to



**Figure 5.24:** (a) Subject ordering according to  $d_M$  and  $d_P$  (Sec. 5.2.6), used as horizontal and vertical axis, respectively. (b) Subject ordering according to  $d_M^*$  and  $d_P^*$  (Eq. 5.29), used as horizontal and vertical axis, respectively. The black arrow indicates the image used to constrain the manifold, representing a normal motion pattern, and used as origin. Asterisk-marked miniatures refer to two subjects with the same amount of total abnormality, but belonging to different populations (cf. App. C).

their distance to patterns of dyssynchrony for which the response rate is roughly known, and grading of the disease severity) are fulfilled, in comparison with the manifold learning approach.

### 5.3.4 Total distance to normality

Each 2D map processed in this study locally contains a measure of abnormality, and the total abnormality contained in each map is therefore defined as  $S_A(\mathbf{I}, \mathbf{I}_0)$  (Sec. 5.2.6).

It is therefore interesting to look for the link between  $S_A(\mathbf{I}, \mathbf{I}_0)$  and the distances  $d_M$  and  $d_P$  defined in Sec. 5.2.6. We can show that the dimensionality reduction inherent to the manifold estimation preserves the concept of abnormality embedded in the input maps, but also takes into account the geometry of the training set. This interpretation and the comparison between the ML and PCA cases are detailed in App. C.

## 5.4 Discussion

We have described a complete pipeline to compare individuals and a population with a specific pattern of abnormal motion in terms of myocardial motion. The extension of manifold learning techniques to embed the definition of a physiologically meaningful origin allowed representing the learnt population as progressive deviations from normality along a manifold structure. The originality of our work resides in using 2D maps of motion abnormalities as input, obtained from a statistical atlas of myocardial motion built from a set of healthy volunteers, which facilitates the definition of an origin for normality. Our experiments demonstrated the relevance of manifold learning techniques to learn a population with a specific pathological pattern, and to compare individuals to this pattern. We first selected the optimal values for the parameters involved in our method, using a synthetic dataset and the training set of CRT candidates for which the manifold is learnt. Then, we demonstrated the performance of our method to characterize both training and testing datasets.

As described in Sec. 5.3.2, we used the Euclidean distance for the metric  $S_A$ . This metric evaluates pixel-wise the difference between two maps of abnormality, being considered as 2D images. The relationship between this metric and the statistical information locally contained in each map will be addressed in further work. Choosing the Euclidean distance may introduce some bias towards global and local shifts of the observed patterns. However, the use of TDFFD [73] guarantees the velocities computed for each subject to be differentiable, and therefore introduces smoothness on the abnormality maps, which limits the above-mentioned bias. We preferred to choose a simple metric for the sake of computational speed. Metrics based on image registration (as used in other manifold learning applications working directly on real images [217]) or image correlation-based metrics cannot be applied in our case as they require the processed images to share the same topology. Indeed, a large variety of patterns are observed on the maps of abnormality we used either for the manifold estimation or for the comparison to the manifold, as visible in Fig. 5.4. In particular, these alternative metrics would certainly fail in case of the lack of abnormal pattern, typically for the maps of healthy volunteers.

We preferred a strategy in which the manifold is estimated for one specific population only (SF patients). This approach differs from classic methods for population comparison [155], which generally consider all subjects as part of a single dataset, and look for the space of reduced dimensionality that allows the best discrimination between different pre-identified groups. Nonetheless, the flexibility of these techniques is limited when a new subject or a new population is added to the existing dataset, as dimensionality reduction is applied to the whole set of studied subjects. In addition, the dimensionality reduction could be biased towards certain populations if they show higher variability. An alternative for moving beyond these limitations consists in separating the analysis for each coherent group of subjects, which is the strategy we have opted for.

In this work, we assumed that the training set contained members close from the origin, namely close from normality. This allows modeling the pathological pattern of SF as a progressive degeneration from normality. In case this methodology is applied to other populations where this assumption does not hold, the ML process can be made simpler (without the additional constraint of exact matching for one point), as formulated in Sec. 5.2.4.

The approach we proposed represents a potential step forward to improve patient selection in the context of CRT. As highlighted in [4], current approaches lack of reproducible tools to perform patient comparison pre- and post- therapy. Our method is ready to be used in both cases: (1) using baseline data, it would allow grading a pattern (distance to normality) and estimating the ability of a patient to respond (distance to patterns for which the response rate is known [8]); (2) using baseline and follow-up data, it would improve the understanding of the link between the evolution of abnormal patterns and CRT outcome. Both aspects will be studied in further work as part of a thorough clinical study.

*Limitations* The pipeline presented in this study was applied to the characterization of individuals against patients with SF, as this pattern is clearly defined on the maps we used as input, which were validated in [83]. Besides, this pattern has been shown to highly condition CRT outcome [8] [198].

The maps were computed from 2D echocardiographic sequences, as it is currently the most clinically widespread modality with sufficient temporal resolution to accurately quantify SF.

The study focused on motion abnormalities only. Its extension to strain abnormalities may refine the analysis of the patterns of cardiac dyssynchrony by allowing the characterization of locally infarcted segments, which may affect CRT outcome [227].

Nonetheless, the methodology described in the present work is generic, and therefore not specific to SF, or abnormality maps obtained from 2D echocardiography. Other potential strategies for building the maps of abnormality could include other imaging modalities (3D echocardiography, magnetic resonance and tagged magnetic resonance as recently proposed [228]) and other pathological cardiac mechanisms such as the classes of mechanical dyssynchrony identified in [8].

The quality of the maps of abnormality is primordial for the accuracy of the proposed method. Both the echocardiographic acquisition and the atlas construction steps (velocity extraction and spatiotemporal synchronization) may influence the patterns observed on the maps and the subject comparison, within the manifold learning process (construction of the  $k$ -NN graph and intra-manifold distance) and when mapping patients to the manifold.

The current strategy, namely first compute maps of abnormality and then perform ML, may not be optimal as both steps are independent. An improvement of our method could combine both steps, learning directly from 2D maps of velocities. Optimality of the method should however be carefully defined, depending on the objective (population modeling or classification, for instance).

## 5.5 Conclusion

We have proposed a method for representing a specific pathological motion pattern as a deviation from normality along a manifold structure, normality being by construction the manifold origin. The method was used to characterize individuals according to their distance to normality, and to the pathological pattern used to estimate the manifold. We first evaluated the optimal set of parameters involved in our pipeline. Then, we illustrated the performance of such an approach in the context of CRT, learning the manifold for a set of patients with SF, a specific pattern of intra-ventricular dyssynchrony, and comparing both healthy volunteers and CRT candidates to this population. Experiments demonstrated the advantage of non-linear embedding of the training set, and the relevance of the proposed method for grading different stages of motion abnormalities and comparing subjects to a specific pathological pattern.



## Appendix A. Choice of the kernel.

The theory of RKHS provides specific results about the link between the properties of the RKHS and the kernel ones. [69] extensively discusses these properties, among which are regularity and invariance by rigid transforms, and the definition of an observation scale.

Taking as example the matching problem of Sec. 5.2.4, simple parametric kernels are of the form  $K_{\mathcal{F}}(\mathbf{I}, \mathbf{J}) = h(S_{\mathcal{A}}(\mathbf{I}, \mathbf{J})) \cdot \mathbf{Id}_{M,M}$ ,  $\forall \mathbf{I}, \mathbf{J} \in \mathcal{A}$ , namely isotropic scalar and invariant by rigid transforms, where  $h : \mathbb{R}^+ \rightarrow \mathbb{R}$  is a given scalar function, and  $\mathbf{Id}_{M,M}$  the identity matrix in  $\mathbb{M}_{M,M}$ .

Examples of such kernels that are semi-definite positive, given  $x \in \mathbb{R}^+$ , are:

- Bessel kernels [229, 69],
- Gaussian kernels:  $h(x) = \exp(-x^2/\sigma_{\mathcal{F}}^2)$ ,
- Cauchy kernels:  $h(x) = (1 + x/\sigma_{\mathcal{F}}^2)^{-1}$ ,
- Sobolev kernels, for which  $h$  is the inverse Fourier transform of  $(1 + x^2)^{-s}$ ,  $s > P + 1/2$ .

Gaussian and Cauchy kernels are particularly of interest as they introduce an observation scale  $\sigma_{\mathcal{F}}$ . However, the choosing the optimal function  $h$  defining the kernel is still an open



issue. In our application, we opted for Gaussian kernels due to their wide use in the machine learning community.

## Appendix B. Formulation of the exact matching problem.

According to the formulation of Eq. 5.3 (Sec. 5.2.4), the exact matching problem has the following analytical solution:

$$f(\mathbf{I}) = \sum_{i=0}^N K_{\mathcal{F}}(\mathbf{I}, \mathbf{I}_i) \cdot \mathbf{a}_i, \quad (5.30)$$

where the vectors  $\mathbf{a}_i \in \mathcal{C}$  are solutions of the following linear system:

$$\sum_{j=0}^N K_{\mathcal{F}}(\mathbf{I}_i, \mathbf{I}_j) \cdot \mathbf{a}_j = \mathbf{x}_i, \quad \forall i \in [0, N]. \quad (5.31)$$

Note that  $K_{\mathcal{F}}(\mathbf{I}_i, \mathbf{I}_j) \in \mathbb{M}_{M,M}$  with this formulation.

Eq. 5.31 can be condensed using the product of block matrices:

$$\mathbf{K}_{\mathcal{A}} \cdot \mathbf{A} = \mathbf{X}, \quad (5.32)$$

where:

- $\mathbf{A}^t = (\mathbf{a}_0^t, \dots, \mathbf{a}_N^t) \in \mathbb{R}^{(N+1)M}$ ,
- $\mathbf{K}_{\mathcal{A}} \in \mathbb{M}_{(N+1)M, (N+1)M}$  is the matrix made of the  $M \times M$ -dimensional blocks  $K_{\mathcal{F}}(\mathbf{I}_i, \mathbf{I}_j)$ ,  $(i, j) \in [0, N]^2$ ,
- $\mathbf{X}^t = (\mathbf{x}_0^t, \dots, \mathbf{x}_N^t) \in \mathbb{R}^{(N+1)M}$ .

If we choose a reproducing kernel of the form (App. A):

$$K_{\mathcal{F}}(\mathbf{I}, \mathbf{J}) = h(S_{\mathcal{A}}(\mathbf{I}, \mathbf{J})) \cdot \mathbf{Id}_{M,M}, \quad (5.33)$$

where  $\mathbf{Id}_{M,M}$  is the identity matrix in  $\mathbb{M}_{M,M}$ , the solution for Eq. 5.3 can be re-written in a simpler form, namely:

$$\begin{cases} f(\mathbf{I}) = \sum_{i=0}^N K_{\mathcal{F}}(\mathbf{I}, \mathbf{I}_i) \cdot \mathbf{a}_i, \\ \text{with } \mathbf{A} = \mathbf{K}_{\mathcal{A}}^{-1} \cdot \mathbf{X}, \end{cases} \quad (5.34)$$

where:

- $\mathbf{A} = (\mathbf{a}_0, \dots, \mathbf{a}_N)^t \in \mathbb{M}_{N+1, M}$ ,
- $\mathbf{K}_{\mathcal{A}} = (K_{\mathcal{F}}(\mathbf{I}_i, \mathbf{I}_j))_{(i,j) \in [0, N]^2} \in \mathbb{M}_{N+1, N+1}$ ,
- $\mathbf{X} = (\mathbf{x}_0, \dots, \mathbf{x}_N)^t \in \mathbb{M}_{N+1, M}$ .

## Appendix C. Link between the total abnormality in each map and proposed distances.

In this paper, we used the Euclidean distance for both metrics  $S_{\mathcal{A}}$  and  $S_{\mathcal{C}}$ . Thus, the total abnormality contained in each map is:

$$S_{\mathcal{A}}(\mathbf{I}, \mathbf{I}_0) = \|\mathbf{I} - \mathbf{I}_0\| = \|\mathbf{I}\|. \quad (5.35)$$

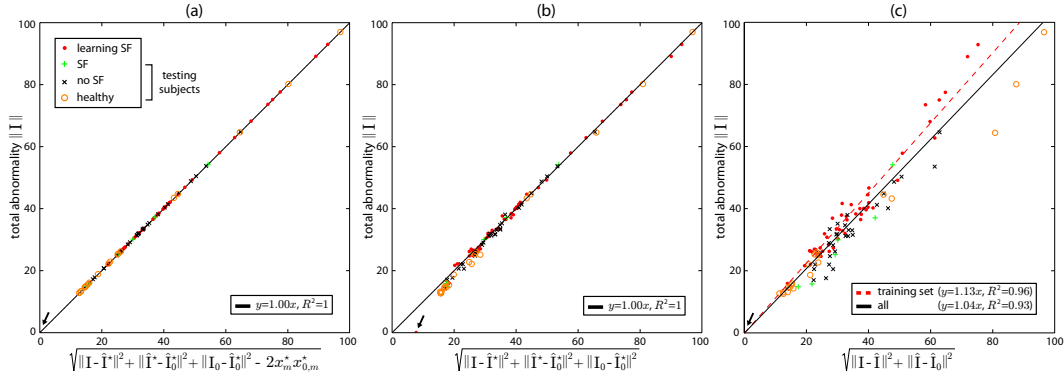


**Figure 5.25:** Subject ordering according to the amount of total abnormality contained in each map and (a) the PCA-based distance to normality with residual, or (b) without residual, or (c) the ML-based total distance to normality. The black arrow indicates the image used to constrain the manifold, representing a normal motion pattern, and used as origin.

In the PCA case, we can demonstrate that:

$$\|\mathbf{I}\|^2 = \|\mathbf{I} - \hat{\mathbf{I}}^*\|^2 + \|\hat{\mathbf{I}}^* - \hat{\mathbf{I}}_0^*\|^2 + \|\mathbf{I}_0 - \hat{\mathbf{I}}_0^*\|^2 - 2 \sum_{m=M+1}^{N+1} x_m^* \cdot x_{0,m}^*, \quad (5.36)$$

where  $\hat{\mathbf{I}}^*$  and  $\hat{\mathbf{I}}_0^*$  are the PCA-based reconstruction of  $\mathbf{I}$  and  $\mathbf{I}_0$  using the first  $M$  principal directions, and  $x_m^*$  and  $x_{0,m}^*$  correspond to the  $m$ th component of  $\mathbf{x}^*$  and  $\mathbf{x}_0^*$ , respectively.

*Proof:* We denote  $\mathbf{e}_m^*$  the eigenvector of the PCA basis corresponding to the  $m$ th component. We can write from the PCA definition:

$$\mathbf{I} = \frac{1}{N+1} \sum_{i=0}^N \mathbf{I}_i + \sum_{m=1}^{N+1} x_m^* \mathbf{e}_m^*. \quad (5.37)$$

From the dimensionality reduction process, we also have that:

$$\hat{\mathbf{I}}^* = \frac{1}{N+1} \sum_{i=0}^N \mathbf{I}_i + \sum_{m=1}^M x_m^* \mathbf{e}_m^*. \quad (5.38)$$

Thus, for the left side of Eq. 5.36:

$$\begin{aligned} \|\mathbf{I}\|^2 &= \|\mathbf{I} - \mathbf{I}_0\|^2 = \sum_{m=1}^{N+1} (x_m^* - x_{0,m}^*)^2, \\ &= \sum_{m=1}^{N+1} ((x_m^*)^2 + (x_{0,m}^*)^2 - 2 \cdot x_m^* \cdot x_{0,m}^*). \end{aligned} \quad (5.39)$$

And for each term of the right side of Eq. 5.36:

$$\|\mathbf{I} - \hat{\mathbf{I}}^*\|^2 = \left\| \sum_{m=1}^{N+1} x_m^* \mathbf{e}_m^* - \sum_{m=1}^M x_m^* \mathbf{e}_m^* \right\|^2 = \sum_{m=M+1}^{N+1} (x_m^*)^2. \quad (5.40)$$

Similarly, we have:

$$\|\mathbf{I}_0 - \hat{\mathbf{I}}_0^*\|^2 = \sum_{m=M+1}^{N+1} (x_{0,m}^*)^2. \quad (5.41)$$

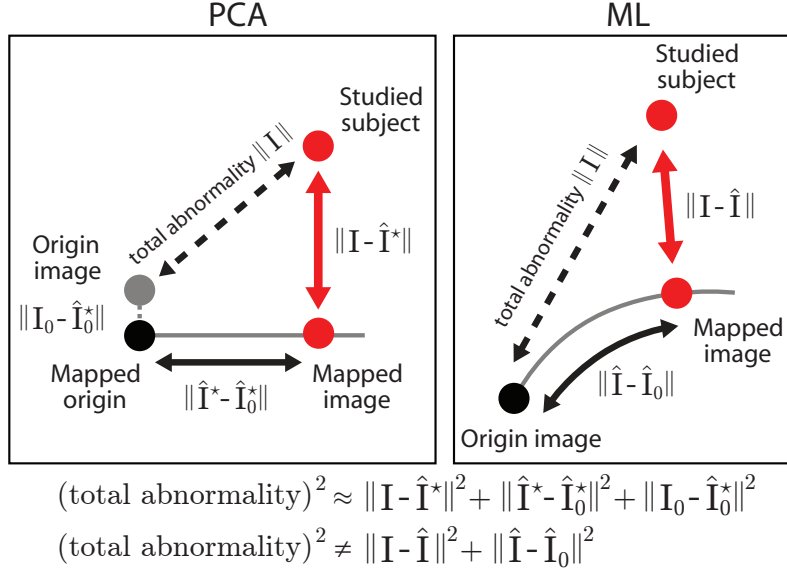


**Figure 5.26:** Relationship between the total abnormality contained in each map and the proposed distances for comparing subjects to the training population.

And finally:

$$\begin{aligned}
\|\hat{\mathbf{I}}^* - \hat{\mathbf{I}}_0^*\|^2 &= \left\| \sum_{m=1}^M x_m^* \mathbf{e}_m^* - \sum_{m=1}^M x_{0,m}^* \mathbf{e}_m^* \right\|^2, \\
&= \sum_{m=1}^M ((x_m^*)^2 + (x_{0,m}^*)^2 - 2 \cdot x_m^* \cdot x_{0,m}^*).
\end{aligned} \tag{5.42}$$

The result of Eq. 5.36 is therefore straightforward.  $\square$

In the PCA case, and according to the computations above, we also have:

$$\|\hat{\mathbf{I}}^* - \hat{\mathbf{I}}_0^*\|^2 = \sum_{m=1}^M (x_m^* - x_{0,m}^*)^2 = S_C(\mathbf{x}^*, \mathbf{x}_0^*)^2, \tag{5.43}$$

and Eq. 5.36 can be rewritten as:

$$\|\mathbf{I}\|^2 = d_P^*(\mathbf{I})^2 + d_M^*(\mathbf{I})^2 + d_P^*(\mathbf{I}_0)^2 - 2 \sum_{m=M+1}^{N+1} x_m^* \cdot x_{0,m}^*. \tag{5.44}$$

This is illustrated in Fig. 5.25a, confirming that both expressions are equal. Note that  $d_M$  and  $d_P$  calculate the Euclidean norm of  $M$ - and  $P$ - dimensional vectors, respectively. The validity of using such distances in the same equation is therefore ensured by the residual term  $2 \cdot \sum_{m=M+1}^{N+1} x_m^* \cdot x_{0,m}^*$ .

Fig. 5.25b compares the amount of total abnormality to the right term of Eq. 5.36 without this residual term, namely to

$\sqrt{\|\mathbf{I} - \hat{\mathbf{I}}^*\|^2 + \|\hat{\mathbf{I}}^* - \hat{\mathbf{I}}_0^*\|^2 + \|\mathbf{I}_0 - \hat{\mathbf{I}}_0^*\|^2}$ , showing this mostly affects the images close to normality.

We performed the same comparison in the ML case, for which the manifold is constrained to pass by  $\mathbf{I}_0$ , and therefore  $\hat{\mathbf{I}}_0^* = \mathbf{I}_0$ , namely  $d_P(\mathbf{I}_0) = 0$ . As visible in Fig. 5.25c, the property

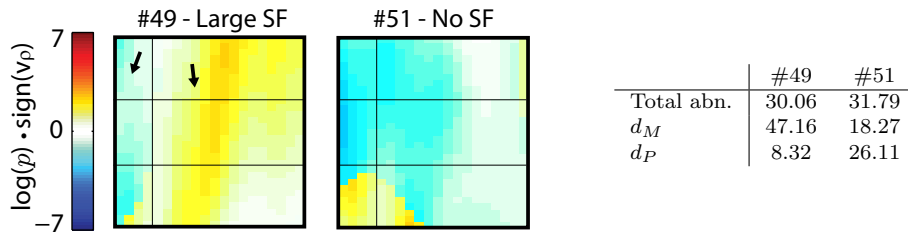


**Figure 5.27:** Example of two patients having the same amount of total abnormality  $S_A(\mathbf{I}, \mathbf{I}_0)$ , but different patterns (presence and absence of SF, respectively). These subjects are clearly discriminated by the use of the proposed distances  $d_M$  and  $d_P$  (cf. table values and asterisks-marked miniatures on Fig. 5.24).

discussed above is not satisfied in this case, linear regression over the plotted data leading to slope coefficients of 1.13 (manifold data only, dashed red line) and 1.04 (whole data, black line), associated to  $R^2$  coefficients of 0.96 and 0.93, respectively. The dimensionality reduction inherent to the manifold estimation still preserves the concept of abnormality embedded in the input maps, but also takes into account the geometry of the training set, as summarized in Fig. 5.26.

These observations are also supported by the fact that some images may contain the same amount of total abnormality, but be clearly discriminated by the proposed distances  $d_M$  and  $d_P$ . Fig. 5.27 illustrates this point for two subjects with different patterns on the maps (one with SF, and the other without SF). Both maps contain the same amount of total abnormality despite the fact that they belong to different groups, but are correctly discriminated by the distances we propose (Fig. 5.27 and asterisk-marked miniatures in Fig. 5.24).



---

## Conclusions

### 6.1 Overview

During the realization of this thesis, we investigated ways of characterizing myocardial motion and deformation patterns, and to include this information in a robust computational scheme for inter-subject comparison. Requirements for this approach (Sec. 1.2) were:

- Quantifying myocardial motion and deformation on each subject. Our solutions for this objective were reported in Chap. 3.
- Estimating the degree of abnormality for each subject, based on the statistical analysis of groups of subjects. This objective was reached in Chap. 3 and 4.
- Being able to compare patients in terms of patterns of dyssynchrony, and not only on a voxel-wise basis. This contribution was reported in Chap. 5.

The underlying clinical objective was to apply these tools to a population of CRT candidates, and demonstrate their added-value for the characterization of pattern-related abnormalities and their evolution. A clinical study was designed on this specific point in Chap. 4.

### 6.2 Outlook and future work

The work carried out in this thesis constitutes a first step towards the use of motion and deformation patterns to understand the effects of CRT and consequently improve the patient selection process. We expect that the work done in this thesis will definitely contribute to further progress in this direction, as discussed in the following paragraphs.

*Registration-based motion and deformation estimation.* The estimation of myocardial motion and deformation has been achieved in this thesis using image registration techniques to track the myocardium along cardiac sequences. As a first step, the registration scheme considered independently each pair of consecutive frames (Chap. 3). The estimated transformations were estimated using a parametric approach (multiscale FFD), and constrained to be diffeomorphic. This approach provided piece-wise stationary velocities, which may be a limitation for the temporal synchronization step of the atlas building, as discussed in Chap. 5.

The design of the atlas pipeline allows the improvement of the registration step independently from the synchronization and statistical steps coming further. Thus, in a subsequent application to the initial atlas publication [83], we improved this step by using temporal diffeomorphic free-form deformation (TDDFD) [73], which enforces temporal consistency and provides differentiable velocities at each instant of the cardiac sequence.

Further work at this level of the atlas pipeline could consist in the improvement of the registration accuracy for any imaging modality, as initiated by some recent registration challenges [230].

*Voxel-based vs. pattern-based inter-subject comparison.* As discussed in Sec. 2.3, the statistical comparison of motion and deformation in sets of subjects can be performed on a voxel-wise or a pattern-wise basis, this latter option being conditioned by the definition of a relevant comparison space. We preferred to keep the analysis general in the first part of the thesis work (Chap. 3) and therefore started with observations at the voxel level. Thus, the interpretation of the patterns of dyssynchrony that may be observed for each patient remained qualitative in a first time. Pattern-based analysis were proposed in Chap. 4 and 5, extending the voxel-wise analysis to groups of voxels or to a space of reduced dimensionality. In particular, the work described in Chap. 4 illustrated the importance of analyzing dyssynchrony in patients at a pattern level before relating it with the therapy outcome.

Future work on this field should first clearly state the space or arrangement of voxels to be considered, depending on the observations to be made: introducing smoothness in the voxel-based analysis (as a consequence of a smooth registration scheme), recognizing abnormal patterns, or comparing subjects to a population (Chap. 5), for example.

*Going beyond Parsai's paper.* The paper of Parsai *et al.* [8] pointed out several interesting issues for CRT studies that we can answer or comment after the work developed in this thesis:

- **Value of SF:** The results presented in [8] may suggest that due to its high response rate, SF should be used as criteria for selecting CRT candidates. Nonetheless, we would like to nuance this statement, based the findings described in Chap. 4. In our data, the detection of SF at baseline led to a modest sensitivity to predict CRT response. There are still few studies about SF targeting the physiological understanding of this mechanism [199] [198]. In terms of its link with CRT response, we agreed with the findings of [8] and [23] in that the correction of SF highly conditions CRT response, but this is not a sufficient condition for CRT response, particularly regarding reverse remodeling. The inclusion of additional variables of non-response such as the ones discussed in Chap. 4 (presence of atrial fibrillation [201], lack of contractile reserve [200], lead position [227], etc.) would be highly recommendable before any consideration of the SF mechanism for selecting patients.

- **Baseline comparison to specific patterns of dyssynchrony:** The paper of Parsai *et al.* [8] invited the cardiologists to rethink their strategy for patient selection. The comparison of a new patient to different mechanisms of dyssynchrony for which the response rate is known may help for estimating the probability of a patient to respond. We started investigating this line of research in Chap. 5 through the proposition of an algorithm for comparing the patterns of abnormal motion of a patient to a population with a given pattern of dyssynchrony. The method is currently applied to baseline data, for the SF pattern. Future work should (1) extend it to the patterns proposed in [8], looking at the predictive value of these classes using baseline data only; (2) apply it to baseline and follow-up data to complement the findings of the study performed in Chap. 4.



• **Which patterns of dyssynchrony?** The paper of [8] presents an algorithmic approach to improve patient selection for CRT, based on the classification of patients according to specific patterns of dyssynchrony (inter-, intra- and atrio-ventricular dyssynchrony). The rationale behind such a classification is that it covers the most common types of patterns of dyssynchrony affecting the LV. Additional patterns of dyssynchrony such as the ones affecting the right ventricle, or a combination of mechanisms (which forms a specific group of patients in [8]) may also be observed. Their influence on CRT response requires further analysis, in particular due to the implantation of the CRT device on the septal and lateral wall of the LV only.

• **A threshold for CRT response?** As discussed in Sec. 2.1.1, a strong limitation to CRT studies may be the definition of CRT response. The concept of quantifying motion and deformation abnormality is particularly interesting with respect to this point, as it overcomes the limitations of a qualitative description or a binary recognition of the mechanisms of dyssynchrony conditioning CRT response. Further studies should not rely on a binary threshold for defining CRT response, but rather consider a spectrum of responses, which may include measures of the abnormality evolution with the therapy.

*Application to other imaging modalities and other mechanisms.* Most of the work realized during this thesis was applied to 2D echocardiographic sequences of the LV, acquired in a 4-chamber view. The 2D US modality was chosen for its high temporal resolution, and its availability pre- and post-implant. The apical 4-chamber view represented the most relevant 2D view to visualize the type of LV dyssynchrony we focused on. Using 3D echocardiography would allow the characterization of all myocardial segments, but with a lower temporal resolution. The application of the atlas framework to other 2D US views, other imaging modalities (magnetic resonance, computed tomography ...) and other clinical settings (stress echocardiography, ischemic cardiomyopathy ...) is relatively straightforward, and only requires a careful tuning of the registration parameters, as we started to do in [73] for 3D US and [104] for t-MRI.

In a similar manner, the methodology developed during the thesis is not specific to the study of LV dyssynchrony and more particularly patterns of intra-ventricular dyssynchrony such as SF, but could perfectly be applied to the characterization of other mechanisms of abnormal motion and deformation. The only requirement to this would be that the use of a complex framework such as building a statistical atlas or learning a manifold represents an added-value for the quantification and the characterization of these mechanisms, as we attempted to demonstrate in Chap. 4 and 5.



CHAPTER 6.



---

## References

- [1] C.-M. Yu, D. L. Hayes, and A. Auricchio, *Cardiac Resynchronization Therapy*. Wiley-Blackwell, 2006.
- [2] J.-U. Voigt, “Rocking will tell it,” *European Heart Journal*, vol. 30, pp. 885–6, 2009.
- [3] B. K. Fornwalt, J. G. Delfino, W. W. Sprague, and J. N. Oshinski, “It’s time for a paradigm shift in the quantitative evaluation of left ventricular dyssynchrony,” *Journal of the American Society of Echocardiography*, vol. 22, pp. 672–6, 2009.
- [4] B. K. Fornwalt, “The dyssynchrony in predicting response to cardiac resynchronization therapy: A call for change,” *Journal of the American Society of Echocardiography*, vol. 24, pp. 180–4, 2011.
- [5] M. D. Cerqueira, N. J. Weissman, V. Dilsizian, A. K. Jacobs, S. Kaul, W. K. Laskey, D. J. Pennell, J. A. Rumberger, T. Ryan, and M. S. Verani, “Standardized myocardial segmentation and nomenclature for tomographic cardiac imaging of the heart: A statement for healthcare professionals from the cardiac imaging committee of the council on clinical cardiology of the American Heart Association,” *Circulation*, vol. 105, pp. 539–42, 2002.
- [6] L. J. Anderson, C. Miyazaki, G. R. Sutherland, and J. K. Oh, “Patient selection and echocardiographic assessment of dyssynchrony in cardiac resynchronization therapy,” *Circulation*, vol. 117, pp. 2009–23, 2008.
- [7] N. M. Hawkins, M. C. Petrie, M. I. Burgess, and J. J. V. McMurray, “Selecting patients for cardiac resynchronization therapy: The fallacy of echocardiographic dyssynchrony,” *Journal of the American College of Cardiology*, vol. 53, pp. 1944–59, 2009.
- [8] C. Parsai, B. H. Bijnens, G. R. Sutherland, A. Baltabaeva, P. Claus, M. Marciniak, V. Paul, M. Schefker, E. Donal, G. Derumeaux, and L. Anderson, “Toward understanding response to cardiac resynchronization therapy: left ventricular dyssynchrony is only one of multiple mechanisms,” *European Heart Journal*, vol. 30, pp. 940–9, 2009.
- [9] W. T. Abraham, W. G. Fisher, A. L. Smith, D. B. Delurgio, A. R. Leon, E. Loh, D. Z. Kocovic, M. Packer, A. L. Clavell, D. L. Hayes, M. Ellestad, J. Messenger, and the MIRACLE study group, “Cardiac resynchronization in chronic heart failure,” *The New England Journal of Medicine*, vol. 346, pp. 1845–53, 2002.
- [10] W. Mullens, R. A. Grimm, T. Verga, T. Dresing, R. C. Starling, B. L. Wilkoff, and W. H. Wilson Tang, “Insights from a cardiac resynchronization optimization clinic as part of a heart failure disease management program,” *Journal of the American College of Cardiology*, vol. 53, pp. 765–73, 2009.
- [11] J. G. F. Cleland, J. C. Daubert, E. Erdmann, N. Freemantle, D. Gras, L. Kappenberger, L. Tavazzi, and the Cardiac Resynchronization Heart Failure (CARE-HF) Study Investigators, “The effect of cardiac resynchronization on morbidity and mortality in heart failure,” *New England Journal of Medicine*, vol. 352, pp. 1539–49, 2005.
- [12] M. G. St John Sutton, T. Plappert, W. T. Abraham, A. L. Smith, D. B. DeLurgio, A. R. Leon, E. Loh, D. Z. Kocovic, W. G. Fisher, M. Ellestad, J. Messenger, K. Kruger, K. E. Hilpisch, M. R. S. Hill, and for the Multicenter InSync Randomized Clinical Evaluation (MIRACLE) Study Group, “Effect of cardiac resynchronization therapy on left ventricular size and function in chronic heart failure,” *Circulation*, vol. 107, pp. 1985–90, 2003.
- [13] K. Dickstein, P. E. Vardas, A. Auricchio, J. C. Daubert, C. Linde, J. McMurray, P. Ponikowski, S. G. Priori, R. Sutton, and D. J. van Veldhuisen, “Focused update of ESC guidelines on device therapy in heart failure: an update of the 2008 ESC guidelines for the diagnosis and treatment of acute and chronic heart failure and the 2007 ESC guidelines for cardiac and resynchronization therapy,” *European Heart Journal*, vol. 31, pp. 2677–87, 2010.

- [14] J. Bax, J. T. Abraham, S. S. Barold, O. A. Breithardt, J. W. H. Fung, S. Garrigue, J. Gorcsan III, D. L. Hayes, D. A. Kass, J. Knuuti, C. Leclercq, C. Linde, D. B. Mark, M. J. Monaghan, P. Nihoyannopoulos, M. J. Schalij, C. Stellbrink, and C.-M. Yu, "Cardiac resynchronization therapy: Part 2 - Issues during and after device implantation and unresolved questions," *Journal of the American College of Cardiology*, vol. 46, pp. 2168–82, 2005.
- [15] K. Dickstein, A. Cohen-Solal, G. Filippatos, J. J. V. McMurray, P. Ponikowski, P. A. Poole-Wilson, A. Strömberg, D. J. van Veldhuisen, D. Atar, A. W. Hoes, A. Keren, A. Mebazaa, M. Nieminen, S. G. Priori, and K. Swedberg, "ESC Guidelines for the diagnosis and treatment of acute and chronic heart failure 2008. The Task Force for the Diagnosis and Treatment of Acute and Chronic Heart Failure 2008 of the European Society of Cardiology. Developed in collaboration with the Heart Failure Association of the ESC (HFA) and endorsed by the European Society of Intensive Care Medicine (ESICM)," *European Heart Journal*, vol. 29, pp. 2388–442, 2008.
- [16] D. J. van Veldhuisen, A. H. Maass, S. G. Priori, P. Stolt, I. C. van Gelder, K. Dickstein, and K. Swedberg, "Implementation of device therapy (cardiac resynchronization therapy and implantable cardioverter defibrillator) for patients with heart failure in Europe: changes from 2004 to 2008," *European Journal of Heart Failure*, vol. 11, pp. 1143–51, 2009.
- [17] J. Bax, J. T. Abraham, S. S. Barold, O. A. Breithardt, J. W. H. Fung, S. Garrigue, J. Gorcsan III, D. L. Hayes, D. A. Kass, J. Knuuti, C. Leclercq, C. Linde, D. B. Mark, M. J. Monaghan, P. Nihoyannopoulos, M. J. Schalij, C. Stellbrink, and C.-M. Yu, "Cardiac resynchronization therapy: Part 1 - Issues before device implantation," *Journal of the American College of Cardiology*, vol. 46, pp. 2153–67, 2005.
- [18] C.-M. Yu, J. E. Sanderson, and J. Gorcsan III, "Echocardiography, dyssynchrony, and the response to cardiac resynchronization therapy," *European Heart Journal*, vol. 31, pp. 2326–39, 2010.
- [19] S. Stewart, A. Jenkins, S. Buchan, A. McGuire, S. Capewell, and J. J. McMurray, "The current cost of heart failure to the National Health Service in the UK," *European Journal of Heart Failure*, vol. 4, pp. 361–71, 2002.
- [20] S. A. Hunt, W. T. Abraham, M. H. Chin, A. M. Feldman, G. S. Francis, T. G. Ganiats, M. Jessup, M. A. Konstam, D. M. Mancini, K. Michl, J. A. Oates, P. S. Rahko, M. A. Silver, L. W. Stevenson, C. W. Yancy, E. M. Antman, S. C. J. Smith, C. D. Adams, J. L. Anderson, D. P. Faxon, V. Fuster, J. L. Halperin, L. F. Hiratzka, S. A. Hunt, A. K. Jacobs, R. Nishimura, J. P. Ornato, R. L. Page, and B. Riegel, "ACC/AHA 2005 Guideline update for the diagnosis and management of chronic heart failure in the adult: A report of the American College of Cardiology/American Heart Association task force on practice guidelines (writing committee to update the 2001 guidelines for the evaluation and management of heart failure): Developed in collaboration with the American College of Chest Physicians and the International Society for Heart and Lung Transplantation: Endorsed by the Heart Rhythm Society," *Circulation*, vol. 112, pp. e154–235, 2005.
- [21] G. B. Bleeker, J. J. Bax, J. W.-H. Fung, E. E. van der Wall, Q. Zhang, M. J. Schalij, J. Y.-S. Chan, and C.-M. Yu, "Clinical versus echocardiographic parameters to assess response to cardiac resynchronization therapy," *The American Journal of Cardiology*, vol. 97, pp. 260–3, 2006.
- [22] N. M. Hawkins, M. C. Petrie, M. R. MacDonald, K. J. Hogg, and J. J. V. McMurray, "Selecting patients for cardiac resynchronization therapy: electrical or mechanical dyssynchrony?," *European Heart Journal*, vol. 27, pp. 1270–81, 2006.
- [23] C. Parsai, A. Baltabaeva, L. Anderson, M. Chaparro, B. H. Bijmens, and G. R. Sutherland, "Low-dose dobutamine stress echo to quantify the degree of remodelling after cardiac resynchronization therapy," *European Heart Journal*, vol. 30, pp. 950–8, 2009.
- [24] J. B. Young, W. T. Abraham, A. L. Smith, A. R. Leon, R. Lieberman, B. Wilkoff, R. C. Canby, J. S. Schroeder, L. B. Liem, S. Hall, K. Wheelan, and the Multicenter InSync ICD Randomized Clinical Evaluation (MIRACLE-ICD) trial investigators, "Combined cardiac resynchronization and implantable cardioversion defibrillation in advanced chronic heart failure: the MIRACLE ICD trial," *Journal of the American Medical Association*, vol. 289, pp. 2685–94, 2003.
- [25] P. W. X. Foley, F. Leyva, and M. P. Frenneaux, "What is treatment success in cardiac resynchronization therapy?," *Europace*, vol. 11, pp. v58–65, 2009.
- [26] V. Delgado and J. J. Bax, "Assessment of systolic dyssynchrony for cardiac resynchronization therapy is clinically useful," *Circulation*, vol. 123, pp. 640–55, 2011.
- [27] R. K. Sung and E. Foster, "Assessment of systolic dyssynchrony for cardiac resynchronization therapy is not clinically useful," *Circulation*, vol. 123, pp. 656–62, 2011.
- [28] E. S. Chung, A. R. Leon, L. Tavazzi, J.-P. Sun, P. Nihoyannopoulos, J. Merlino, W. T. Abraham, S. Ghio, C. Leclercq, J. J. Bax, C.-M. Yu, J. Gorcsan III, M. St John Sutton, J. De Sutter, and J. Murillo, "Results of the predictors of response to CRT (PROSPECT) trial," *Circulation*, vol. 117, pp. 2608–16, 2008.

- [29] A. Achilli, C. Peraldo, M. Sassara, S. Orazi, S. Bianchi, F. Laurenzi, R. Donati, G. B. Perego, A. Spampinato, S. Valsecchi, A. Denaro, and A. Puglisi, "Prediction of response to cardiac resynchronization therapy: the selection of candidates for CRT (SCART) study," *Pacing and Clinical Electrophysiology*, vol. 29, pp. S11–9, 2006.
- [30] M. Richardson, N. Freemantle, M. J. Calvert, J. G. Cleland, L. Tavazzi, C. S. S. Committee, and Investigators, "Predictors and treatment response with cardiac resynchronization therapy in patients with heart failure characterized by dyssynchrony: a predefined analysis from the CARE-HF trial," *European Heart Journal*, vol. 28, pp. 1827–34, 2007.
- [31] S. Lafitte, P. Reant, A. Zaroui, E. Donal, A. Mignot, H. Bougted, H. Belghiti, P. Bordachar, A. Deplagne, J. Chabaneix, F. Franceschi, J.-C. Deharo, P. Dos Santos, J. Clementy, R. Roudaut, C. Leclercq, and G. Habib, "Validation of an echocardiographic multiparametric strategy to increase responders patients after cardiac resynchronization: a multicentre study," *European Heart Journal*, vol. 30, pp. 2880–7, 2009.
- [32] M. Santaularia-Tomas and T. P. Abraham, "Criteria predicting response to crt: is more better?," *European Heart Journal*, vol. 30, pp. 2835–7, 2009.
- [33] E. K. Heist, C. Taub, D. Fan, D. Arzola-Castaner, C. R. Alabiad, V. Y. Reddy, M. Mansour, T. Mela, M. H. Picard, J. N. Ruskin, and J. P. Singh, "Usefulness of a novel "response score" to predict hemodynamic and clinical outcome from cardiac resynchronization therapy," *The American Journal of Cardiology*, vol. 97, pp. 1732–6, 2006.
- [34] B. W. L. De Boeck, A. J. Teske, M. Meine, G. E. Leenders, M. J. Cramer, F. W. Prinzen, and P. A. Doevendans, "Septal rebound stretch reflects the functional substrate to cardiac resynchronization therapy and predicts volumetric and neurohormonal response," *European Journal of Heart Failure*, vol. 11, pp. 863–71, 2009.
- [35] M. Szulik, M. Tillekaerts, V. Vangeel, J. Ganame, R. Willems, R. Lenarczyk, F. Rademakers, Z. Kalarus, T. Kukulski, and J.-U. Voigt, "Assessment of apical rocking: a new, integrative approach for selection of candidates for cardiac resynchronization therapy," *European Journal of Echocardiography*, vol. 11, pp. 863–9, 2010.
- [36] V. Mor-avi, R. M. Lang, L. P. Badano, M. Belohlavek, N. M. Cardim, G. Derumeaux, M. Galderisi, T. Marwick, S. F. Nagueh, P. P. Sengupta, R. Sicari, O. A. Smiseth, B. Smulevitz, M. Takeuchi, J. D. Thomas, M. Vannan, J.-U. Voigt, and J. L. Zamorano, "Current and evolving echocardiographic techniques for the quantitative evaluation of cardiac mechanics: ASE/EAE consensus statement on methodology and indications endorsed by the Japanese Society of Echocardiography," *Journal of the American Society of Echocardiography*, vol. 24, pp. 277–313, 2011.
- [37] G. R. Sutherland, L. Hatle, P. Claus, J. D'hooge, and B. Bijnens, *Doppler Myocardial Imaging, A Textbook*. BSWK bvba, Scientific Consulting and Publishing-Hasselt, Belgium, 2006.
- [38] P. Sogaard, H. Egeblad, W. Y. Kim, H. K. Jensen, A. K. Pedersen, B. Ø. Kristensen, and P. T. Mortensen, "Tissue doppler imaging predicts improved systolic performance and reversed left ventricular remodeling during long-term cardiac resynchronization therapy," *Journal of the American College of Cardiology*, vol. 40, pp. 723–30, 2002.
- [39] J. D'hooge, A. Heimdal, F. Jamal, T. Kukulski, B. Bijnens, F. Rademakers, L. Hatle, P. Suetens, and G. Sutherland, "Regional strain and strain rate measurements by cardiac ultrasound: Principles, implementation and limitations," *European Journal of Echocardiography*, vol. 1, pp. 154–70, 2000.
- [40] A. Heimdal, A. Støylen, H. Torp, and T. Skjaerpe, "Real-time strain rate imaging of the left ventricle by ultrasound," *Journal of the American Society of Echocardiography*, vol. 11, pp. 1013–9, 1998.
- [41] T. F. Cootes, C. J. Taylor, D. H. Cooper, and J. Graham, "Active shape models - their training and application," *Computer Vision and Image Understanding*, vol. 61, pp. 38–59, 1995.
- [42] T. F. Cootes, G. J. Edwards, and C. J. Taylor, "Active appearance models," *IEEE Transactions on Pattern Analysis and Machine Intelligence*, vol. 23, pp. 681–5, 2001.
- [43] S. C. Mitchell, J. G. Bosch, B. P. F. Lelieveldt, R. J. van der Geest, J. H. C. Reiber, and M. Sonka, "3-d active appearance models: Segmentation of cardiac MR and ultrasound images," *IEEE Transactions on Medical Imaging*, vol. 21, pp. 1167–78, 2002.
- [44] N. F. Osman, W. S. Kerwin, E. R. McVeigh, and J. L. Prince, "Cardiac motion tracking using CINE harmonic phase (HARP) magnetic resonance imaging," *Magnetic Resonance in Medicine*, vol. 42, pp. 1048–60, 1999.
- [45] N. F. Osman, E. R. McVeigh, and J. L. Prince, "Imaging heart motion using harmonic phase MRI," *IEEE Transactions on Medical Imaging*, vol. 19, pp. 186–202, 2000.

- [46] T. Arts, F. W. Prinzen, T. Delhaas, J. Milles, A. Rossi, and P. Clarysse, "Mapping displacement and deformation of the heart with local sine wave modeling," *IEEE Transactions on Medical Imaging*, vol. 29, pp. 1114–23, 2010.
- [47] Z. Qian, D. N. Metaxas, and L. Axel, "Non-tracking-based 2D strain estimation in tagged MRI," in *Proc. IEEE International Symposium on Biomedical Imaging (ISBI)*, pp. 711–4, 2008.
- [48] T. Chen, X. Wang, and L. Axel, "Automated 3D motion tracking using Gabor filter bank, robust point matching, and deformable models," *IEEE Transactions on Medical Imaging*, vol. 9, pp. 1–11, 2010.
- [49] H. Wang and A. Amini, "Cardiac Motion and Deformation Recovery from MRI: A Review," *IEEE Transactions on Medical Imaging*, vol. 31, no. 2, pp. 487–503, 2012.
- [50] T. H. Marwick, C.-M. Yu, and J. P. Sun, *Myocardial Imaging: Tissue Doppler and Speckle Tracking*. Wiley-Blackwell, 2007.
- [51] Q. Duan, E. Angelini, S. Homma, and A. Laine, "Validation of optical-flow for quantification of myocardial deformations on simulated RT3D ultra-sound," in *Proc. IEEE International Symposium on Biomedical Imaging*, pp. 944–7, 2007.
- [52] A. Elen, H. Choi, D. Loeckx, H. Gao, P. Claus, P. Suetens, F. Maes, and J. D'hooge, "Three-dimensional cardiac strain estimation using spatio-temporal elastic registration of ultrasound images: a feasibility study," *IEEE Transactions on Medical Imaging*, vol. 27, pp. 1580–91, 2008.
- [53] T. Kawagishi, "Speckle tracking for assessment of cardiac motion and dyssynchrony," *Echocardiography*, vol. 25, pp. 1167–71, 2008.
- [54] Y. Abe, T. Kawagishi, and H. Ohuchi, "Accurate detection of regional contraction using novel 3-dimensional speckle tracking technique," *Journal of the American College of Cardiology*, vol. 51, pp. 903–1253, 2008.
- [55] Y. Wang, B. Georgescu, H. Houle, and D. Comaniciu, "Volumetric myocardial mechanics from 3d+t ultrasound data with multi-model tracking," in *Proc. Statistical Atlases and Computational Models of the Heart (STACOM), MICCAI'10 Workshop, LNCS vol. 6364*, pp. 184–93, 2010.
- [56] J. Andrade, L. Cortez, O. Campos, A. Arruda, J. Pinheiro, L. Vulcanis, T. Shiratsuchi, R. Kalil-Filho, and G. Cerri, "Left ventricular twist: comparison between two-and three-dimensional speckle-tracking echocardiography in healthy volunteers," *European Journal of Echocardiography*, vol. 12, p. 76, 2011.
- [57] J. P. Thirion, "Image matching as a diffusion process: An analogy with Maxwell's demons," *Medical Image Analysis*, vol. 2, pp. 243–60, 1998.
- [58] D. Rueckert, L. I. Sonoda, C. Hayes, D. L. Hill, M. O. Leach, and D. J. Hawkes, "Nonrigid registration using free-form deformations: application to breast MR images," *IEEE Transactions on Medical Imaging*, vol. 18, pp. 712–21, 1999.
- [59] X. Pennec, P. Cachier, and N. Ayache, "Understanding the "demon's algorithm"?: 3D non-rigid registration by gradient descent," in *Proc. International Conference on Medical Image Computing and Computer Assisted Intervention (MICCAI), LNCS vol. 1679*, pp. 597–605, 1999.
- [60] P. Cachier, E. Bardinnet, D. Dormont, X. Pennec, and N. Ayache, "Iconic feature based nonrigid registration: the pasha algorithm," *Computer Vision and Image Understanding*, vol. 89, pp. 272–98, 2003.
- [61] S. Modersitzki, *Numerical Methods for Image Registration*. Oxford University Press, 2004.
- [62] T. Vercauteren, X. Pennec, A. Perchant, and N. Ayache, "Diffeomorphic demons: efficient non-parametric image registration," *Neuroimage*, vol. 45, pp. S61–72, 2009.
- [63] S. Lee, G. Wolberg, K.-Y. Chwa, and S. S. Y., "Image metamorphosis with scattered feature constraints," *IEEE Transactions on Visualization and Computer Graphics*, vol. 2, pp. 337–54, 1996.
- [64] S. Lee, G. Wolberg, and S. S. Y., "Scattered data interpolation with multilevel b-splines," *IEEE Transactions on Visualization and Computer Graphics*, vol. 3, pp. 228–44, 1997.
- [65] G. Christensen, R. Rabbit, and M. Miller, "Deformable templates using large deformation kinematics," *IEEE Transactions on Image Processing*, vol. 5, pp. 1437–47, 1996.
- [66] A. Trouvé, "Diffeomorphisms groups and pattern matching in image analysis," *International Journal of Computer Vision*, vol. 28, pp. 213–21, 1998.
- [67] M. Miller, A. Trouvé, and L. Younes, "On the metrics and Euler-Lagrange equations of computational anatomy," *Annual Review of Biomedical Engineering*, vol. 4, pp. 375–405, 2002.

- [68] M. F. Beg, M. I. Miller, A. Trouvé, and L. Younes, “Computing large deformation metric mappings via geodesic flows of diffeomorphisms,” *International Journal of Computer Vision*, vol. 61, pp. 139–57, 2005.
- [69] J. A. Glaunes, *Transport par difféomorphismes de points, de mesures et de courants pour la comparaison de formes et l’anatomie numérique*. Phd thesis, Université Paris 13, 2005.
- [70] S. Saitoh, *Theory of Reproducing Kernels and its Applications*. Pitman Research Notes in Mathematical Series, 189. Wiley, 1988.
- [71] S. Durrleman, *Statistical models of currents for measuring the variability of anatomical curves, surfaces and their evolution*. Phd thesis, Université de Nice-Sophia Antipolis, 2010.
- [72] M. Bro-Nielsen and C. Gramkow, “Fast fluid registration of medical images,” in *Proc. International Conference on Visualization in Biomedical Computing (VBC), LNCS vol. 1131*, pp. 267–76, 1996.
- [73] M. De Craene, G. Piella, O. Camara, N. Duchateau, E. Silva, A. Doltra, J. Dhooge, J. Brugada, M. Sitges, and A. F. Frangi, “Spatiotemporal diffeomorphic free-form deformation: Application to motion and strain estimation from 3D echocardiography,” *Medical Image Analysis*, vol. 16, no. 2, pp. 427–50, 2012.
- [74] V. Arsigny, O. Commowick, X. Pennec, and N. Ayache, “A log-Euclidean framework for statistics on diffeomorphisms,” in *Proc. International Conference on Medical Image Computing and Computer Assisted Intervention (MICCAI), LNCS vol. 4190*, pp. 924–31, 2006.
- [75] M. Bossa, M. Hernandez, and S. Olmos, “Contributions to 3D diffeomorphic atlas estimation: Application to brain images,” in *Proc. International Conference on Medical Image Computing and Computer Assisted Intervention (MICCAI), LNCS vol. 4791*, pp. 667–74, 2007.
- [76] M. Hernandez, M. Bossa, and S. Olmos, “Registration of anatomical images using paths of diffeomorphisms parameterized with stationary vector field,” *Journal of Computational and Applied Mathematics*, vol. 85, pp. 291–306, 2009.
- [77] T. Vercauteren, X. Pennec, A. Perchant, and N. Ayache, “Non-parametric diffeomorphic image registration with the demons algorithm,” in *Proc. International Conference on Medical Image Computing and Computer Assisted Intervention (MICCAI), LNCS vol. 4792*, pp. 319–26, 2007.
- [78] D. Rueckert, P. Aljabar, R. A. Heckemann, J. V. Hajnal, and A. Hammers, “Diffeomorphic registration using B-splines,” in *Proc. International Conference on Medical Image Computing and Computer Assisted Intervention (MICCAI), LNCS vol. 4191*, pp. 702–9, 2006.
- [79] G. Wahba, *Spline models for observational data*. Philadelphia: Society for Industrial and Applied Mathematics, 1990.
- [80] K. Strassburger and F. Bretz, *Splines minimizing rotation-invariant seminorms in Sobolev spaces, constructive theory of functions of several variables*. Constructive Theory of Functions of Several Variables, LNM 571, Springer-Verlag, Berlin, 1977.
- [81] S. Nithianathan, K. K. Brock, M. J. Daly, H. Chan, J. C. Irish, and J. H. Siewerdsen, “Demons deformable registration for CBCT-guided procedures in the head and neck: convergence and accuracy,” *Medical Physics*, vol. 36, pp. 4755–64, 2009.
- [82] H. C. Kuo, K. S. Chuang, D. Mah, A. Wu, L. Hong, R. Yaparalvi, and S. Kalnicki, “Multi-scale regularization approaches of non-parametric deformable registrations,” *Journal of Digital Imaging*, vol. 24, pp. 586–97, 2011.
- [83] N. Duchateau, M. De Craene, G. Piella, E. Silva, A. Doltra, M. Sitges, B. H. Bijnens, and A. F. Frangi, “A spatiotemporal statistical atlas of motion for the quantification of abnormal myocardial tissue velocities,” *Medical Image Analysis*, vol. 15, pp. 316–28, 2011.
- [84] L. Risser, F.-X. Vialard, M. Murgasova, D. Holm, and D. Rueckert, “Large deformation diffeomorphic registration using fine and coarse strategies,” in *Proc. International Conference on Medical Image Computing and Computer Assisted Intervention (MICCAI), LNCS vol. 6204*, pp. 186–97, 2010.
- [85] S. Song and R. Leahy, “Computation of 3D velocity fields from 3D cine ct images of a human heart,” *IEEE Transactions on Medical Imaging*, vol. 10, pp. 295–306, 1991.
- [86] J. Gorce, D. Friboulet, and I. Magnin, “Estimation of three-dimensional cardiac velocity fields: assessment of a differential method and application to three-dimensional CT data,” *Medical Image Analysis*, vol. 1, pp. 245–61, 1997.
- [87] A. Bistoquet, J. Oshinski, and O. Skrinjar, “Left ventricular deformation recovery from cine MRI using an incompressible models,” *IEEE Transactions on Medical Imaging*, vol. 26, pp. 1136–53, 2007.

- [88] E. Haber and J. Modersitzki, "Numerical methods for volume preserving image registration," *Inverse Problems*, vol. 20, p. 1621, 2004.
- [89] K. A. Saddi, C. Chefd'hotel, and F. Cheriet, "Large deformation registration of contrast-enhanced images with volume-preserving constraint," in *Proc. SPIE Conference on Medical Imaging*, p. 651203, 2007.
- [90] T. Mansi, X. Pennec, M. Sermesant, H. Delingette, and N. Ayache, "ilogdemons: A demons-based registration algorithm for tracking incompressible elastic biological tissues," *International Journal of Computer Vision*, vol. 92, pp. 92–111, 2011.
- [91] T. Mansi, X. Pennec, M. Sermesant, H. Delingette, and N. Ayache, "Logdemons revisited: Consistent regularisation and incompressibility constraint for soft tissue tracking in medical images," in *Proc. International Conference on Medical Image Computing and Computer Assisted Intervention (MICCAI), LNCS vol. 6362*, pp. 652–9, 2010.
- [92] J. Hinkle, P. Fletcher, B. Wang, B. Salter, and S. Joshi, "4D map image reconstruction incorporating organ motion," in *Proc. Information Processing in Medical Imaging (IPMI), LNCS vol. 5636*, pp. 676–87, 2009.
- [93] M. J. Ledesma-Carbayo, J. Kybic, M. Desco, A. Santos, M. Suhling, P. Hunziker, and M. Unser, "Spatio-temporal nonrigid registration for ultrasound cardiac motion estimation," *IEEE Transactions on Medical Imaging*, vol. 24, pp. 1113–26, 2005.
- [94] C. Metz, S. Klein, M. Schaap, T. van Walsum, and W. Niessen, "Nonrigid registration of dynamic medical imaging data using nD+t B-splines and a groupwise optimization approach," *Medical Image Analysis*, vol. 15, pp. 238–49, 2011.
- [95] M. Yigitsoy, C. Wachinger, and N. Navab, "Temporal groupwise registration for motion modeling," in *Proc. Image Processing in Medical Imaging (IPMI), LNCS vol. 6801*, pp. 648–59, 2011.
- [96] A. R. Khan and M. F. Beg, "Representation of time-varying shapes in the large deformation diffeomorphic framework," in *Proc. IEEE International Symposium on Biomedical Imaging (ISBI)*, pp. 1521–4, 2008.
- [97] A. Qiu, M. Albert, L. Younes, and M. I. Miller, "Time sequence diffeomorphic metric mapping and parallel transport track time-dependent shape changes," *Neuroimage*, vol. 45, pp. S51–60, 2009.
- [98] S. Durrleman, X. Pennec, A. Trouvé, G. Gerig, and N. Ayache, "Spatiotemporal atlas estimation for developmental delay detection in longitudinal datasets," in *Proc. International Conference on Medical Image Computing and Computer Assisted Intervention (MICCAI), LNCS vol. 5761*, pp. 297–304, 2009.
- [99] A. Trouvé and F. X. Vialard, "Shape splines and stochastic shape evolutions: A second order point of view," *ArXiv e-prints 1003.3895*, 2010.
- [100] F. X. Vialard and A. Trouvé, "A second-order model for time-dependent data interpolation: Splines on shape spaces," in *Proc. Spatio-temporal Image Analysis for Longitudinal and Time-Series Image Data (STIA), MICCAI'10 Workshop*, 2010.
- [101] M. De Craene, G. Piella, N. Duchateau, E. Silva, A. Doltra, J. D'hooge, O. Camara, M. Sitges, and A. F. Frangi, "Temporal diffeomorphic free-form deformation for strain quantification in 3D-US images," in *Proc. International Conference on Medical Image Computing and Computer Assisted Intervention (MICCAI), LNCS vol. 6362*, pp. 1–8, 2010.
- [102] Z. Zhang, D. J. Sahn, and X. Song, "Frame to frame diffeomorphic motion analysis from echocardiographic sequences," in *Proc. Mathematical Foundations of Computational Anatomy (MFCA), MICCAI'11 Workshop*, pp. 15–24, 2011.
- [103] Z. Zhang, D. J. Sahn, and X. Song, "Temporal diffeomorphic motion analysis from echocardiographic sequences by using intensity transitivity consistency," in *Proc. Statistical Atlases and Computational Models of the Heart (STACOM), MICCAI'11 Workshop*, pp. 267–76, 2011.
- [104] M. De Craene, C. Tobon-Gomez, C. Butakoff, N. Duchateau, G. Piella, K. S. Rhode, and A. F. Frangi, "Temporal diffeomorphic free form deformation (TDFFD) applied to motion and deformation quantification of tagged MRI sequences," in *Proc. Statistical Atlases and Computational Models of the Heart (STACOM), MICCAI'11 Workshop, LNCS vol.7085*, pp. 68–77, 2012.
- [105] U. Grenander and M. I. Miller, "Computational anatomy: an emerging discipline," *Quarterly of Applied Mathematics*, vol. 56, pp. 617–94, 1998.
- [106] M. Miller, A. Banerjee, G. Christensen, S. Joshi, N. Khaneja, U. Grenander, and L. Matejic, "Statistical methods in computational anatomy," *Statistical Methods in Medical Research*, vol. 60, p. 267, 1997.

- [107] M. I. Miller, “Computational anatomy: shape, growth, and atrophy comparison via diffeomorphisms,” *Neuroimage*, vol. 23, pp. 19–33, 2004.
- [108] M. I. Miller and A. Qiu, “The emerging discipline of computational functional anatomy,” *Neuroimage*, vol. 45, pp. S16–39, 2009.
- [109] A. W. Toga, P. M. Thompson, S. Mori, K. Amunts, and K. Zilles, “Towards multimodal atlases of the human brain,” *Nature Reviews Neuroscience*, vol. 7, pp. 952–66, 2006.
- [110] A. A. Young and A. F. Frangi, “Computational cardiac atlases: from patient to population and back,” *Experimental Physiology*, vol. 94, pp. 578–96, 2009.
- [111] R. Chandrashekar, R. Mohiaddin, and D. Rueckert, “Comparison of cardiac motion fields from tagged and untagged MR images using nonrigid registration,” in *Proc. International Conference on Functional Imaging and Modeling of the Heart (FIMH), LNCS vol. 3504*, pp. 425–33, 2005.
- [112] A. Rao, R. Chandrashekar, G. I. Sanchez-Ortiz, R. Mohiaddin, P. Aljabar, J. V. Hajnal, B. K. Puri, and D. Rueckert, “Spatial transformation of motion and deformation fields using nonrigid registration,” *IEEE Transactions on Medical Imaging*, vol. 23, pp. 1065–76, 2004.
- [113] N. F. Rougon, C. Petitjean, and F. J. Prêteux, “Building and using a statistical 3D motion atlas for analyzing myocardial contraction in MRI,” in *Proc. SPIE Conference on Medical Imaging*, pp. 253–64, 2004.
- [114] M. Vaillant, M. Miller, L. Younes, and A. Trouvé, “Statistics on diffeomorphisms via tangent space representations,” *Neuroimage*, vol. 23, pp. 161–9, 2004.
- [115] P. T. Fletcher, C. Lu, S. M. Pizer, and S. Joshi, “Principal geodesic analysis for the study of nonlinear statistics of shape,” *IEEE Transactions on Medical Imaging*, vol. 23, pp. 995–1005, 2004.
- [116] C. J. Twining and S. Marsland, “Constructing an atlas for the diffeomorphism group of a compact manifold with boundary, with application to the analysis of image registrations,” *Journal of Computational and Applied Mathematics*, vol. 222, pp. 411–28, 2008.
- [117] X. Pennec and P. Fillard, “Statistical computing on non-linear spaces for computational anatomy,” in *Biomedical Image Analysis: Methodologies and Applications*, Springer, 2010. In press.
- [118] B. C. Davis, P. T. Fletcher, E. Bullitt, and S. Joshi, “Population shape regression from random design data,” *International Journal of Computer Vision*, vol. 90, pp. 255–66, 2010.
- [119] G. Hart, Y. Shi, H. Zhu, M. Sanchez, M. Styner, and M. Niethamme, “DTI longitudinal atlas construction as an average of growth models,” in *Proc. Spatio-temporal Image Analysis for Longitudinal and Time-Series Image Data (STIA), MICCAI’10 Workshop*, 2010.
- [120] G. Langs, G. Kasprian, E. Ditttrich, M. Bittner, P. C. Brugger, and D. Prayer, “Group-wise spatio-temporal registration and segmentation of fetal cortical surface development,” in *Proc. Spatio-temporal Image Analysis for Longitudinal and Time-Series Image Data (STIA), MICCAI’10 Workshop*, 2010.
- [121] A. R. Khan, A. Trouvé, and M. F. Beg, “Cross-sectional analysis of anatomical shape change over time via statistics on 4D within-subject flows,” in *Proc. Spatio-temporal Image Analysis for Longitudinal and Time-Series Image Data (STIA), MICCAI’10 Workshop*, 2010.
- [122] A. Qiu, L. Younes, M. I. Miller, and J. G. Csernansky, “Parallel transport in diffeomorphisms distinguishes the time-dependent pattern of hippocampal surface deformation due to healthy aging and the dementia of the Alzheimer’s type,” *NeuroImage*, vol. 40, pp. 68–76, 2008.
- [123] M. Lorenzi, N. Ayache, X. Pennec, and the Alzheimer’s Disease Neuroimaging Initiative, “Schild’s ladder for the parallel transport of deformations in time series of images,” in *Proc. Information Processing in Medical Imaging (IPMI), LNCS vol. 6801*, pp. 463–74, 2011.
- [124] M. Lorenzi and X. Pennec, “Geodesics, parallel transport and one-parameter subgroups for diffeomorphic image registration,” in *Proc. Mathematical Foundations of Computational Anatomy (MFCA), MICCAI’11 Workshop*, pp. 64–74, 2011.
- [125] X. Pennec and M. Lorenzi, “Which parallel transport for the statistical analysis of longitudinal deformations?,” in *Proc. Colloque GRETSI*, 2011.
- [126] K. J. Friston, C. D. Frith, P. F. Liddle, and R. S. J. Frackowiak, “Comparing functional (PET) images: The assessment of significant change,” *Journal of Cerebral Blood Flow and Metabolism*, vol. 11, pp. 690–9, 1991.
- [127] K. J. Worsley, A. C. Evans, S. Marrett, and P. Neelin, “A three-dimensional statistical analysis for rCBF activation studies in human brain,” *Journal of Cerebral Blood Flow and Metabolism*, vol. 12, pp. 900–18, 1992.

- [128] K. J. Friston, K. J. Worsley, R. S. J. Frackowiak, J. C. Mazziotta, and A. C. Evans, "Assessing the significance of focal activations using their spatial extent," *Human Brain Mapping*, vol. 1, pp. 214–20, 1994.
- [129] K. J. Worsley, "Local maxima and the expected Euler characteristic of excursion sets of  $\chi^2$ ,  $f$  and  $t$  fields," *Advances in applied probability*, vol. 2, pp. 13–42, 1994.
- [130] K. J. Friston, A. P. Holmes, K. J. Worsley, J.-B. Poline, C. D. Frith, and R. S. J. Frackowiak, "Statistical parametric maps in functional imaging: A general linear approach," *Human Brain Mapping*, vol. 2, pp. 189–210, 1995.
- [131] K. J. Friston, A. P. Holmes, J.-B. Poline, C. J. Price, and C. D. Frith, "Detecting activations in PET and fMRI: Levels of inference and power," *Neuroimage*, vol. 4, pp. 223–35, 1995.
- [132] K. J. Friston, J. B. Poline, A. P. Holmes, C. D. Frith, and R. S. J. Frackowiak, "A multivariate analysis of PET activation studies," *Human Brain Mapping*, vol. 40, pp. 140–51, 1996.
- [133] K. J. Worsley, S. Marrett, P. Neelin, A. C. Vandal, K. J. Friston, and A. C. Evans, "A unified statistical approach for determining significant voxels in images of cerebral activation," *Human Brain Mapping*, vol. 4, pp. 58–73, 1996.
- [134] I. C. Wright, P. K. McGuire, J. B. Poline, J. M. Travere, R. M. Murray, C. D. Frith, R. S. J. Frackowiak, and K. J. Friston, "A voxel-based method for the statistical analysis of gray and white matter density applied to schizophrenia," *Neuroimage*, vol. 20, pp. 244–52, 1995.
- [135] J. Ashburner and K. J. Friston, "Voxel-based morphometry: the methods," *Neuroimage*, vol. 11, pp. 805–21, 2000.
- [136] J. Ashburner, J. G. Csernansky, C. Davatzikos, N. C. Fox, G. B. Frisoni, and P. M. Thompson, "Computer-assisted imaging to assess brain structure in healthy and diseased brains," *Lancet Neurology*, vol. 2, pp. 79–88, 2003.
- [137] N. Leporé, C. Brun, M. C. Chou, Y. Y. and Chiang, R. A. Dutton, K. M. Hayashi, E. Luders, O. L. Lopez, H. Aizenstein, A. W. Toga, J. T. Becker, and P. M. Thompson, "Generalized tensor-based morphometry of HIV/AIDS using multivariate statistics on deformation tensors," *IEEE Transactions on Medical Imaging*, vol. 27, pp. 129–41, 2008.
- [138] O. Commowick, P. Fillard, O. Clatz, and S. K. Warfield, "Detection of DTI white matter abnormalities in multiple sclerosis patients," in *Proc. International Conference on Medical Image Computing and Computer Assisted Intervention (MICCAI), LNCS vol. 5241*, pp. 975–82, 2008.
- [139] F. L. Bookstein, "'voxel-based morphometry' should not be used with imperfectly registered images," *Neuroimage*, vol. 14, pp. 1454–62, 2001.
- [140] J. Ashburner and K. J. Friston, "Why voxel-based morphometry should be used," *Neuroimage*, vol. 140, pp. 1238–43, 2001.
- [141] C. Davatzikos, "Why voxel-based morphometric analysis should be used with great caution when characterizing group differences," *Neuroimage*, vol. 23, pp. 17–20, 2004.
- [142] H. Abdi, *Bonferroni and Šidák corrections for multiple comparisons*. In N. J. Salkind (ed.). *Encyclopedia of Measurement and Statistics*. Thousand Oaks, CA: Sage, 2000.
- [143] J. P. Shaffer, "Multiple hypothesis testing," *Annual Review of Psychology*, vol. 46, pp. 561–84, 1995.
- [144] T. V. Perneger, "What's wrong with Bonferroni adjustments," *British Medical Journal*, vol. 316, pp. 1236–8, 1998.
- [145] P. C. Fletcher, R. J. Dolan, T. Shallice, C. D. Frith, R. S. J. Frackowiak, and K. J. Friston, "Is multivariate analysis of PET data more revealing than the univariate approach? Evidence from a study of episodic memory retrieval," *Neuroimage*, vol. 30, pp. 209–15, 1996.
- [146] A. R. McIntosh, F. L. Bookstein, J. V. Haxby, and C. L. Grady, "Spatial pattern analysis of functional brain images using partial least squares," *Neuroimage*, vol. 30, pp. 143–57, 1996.
- [147] F. L. Bookstein, *Biometrics and brain maps: the promise of the morphometric synthesis*. In: *Neuroinformatics: an Overview of the Human Brain Project*. Oxford University Press, 1996.
- [148] P. Comon, "Independent component analysis: a new concept?," *Signal Processing*, vol. 36, pp. 287–314, 1994.
- [149] A. Hyvärinen, J. Karhunen, and E. Oja, *Independent Component Analysis*. New York: Wiley, 2001.
- [150] A. Hyvärinen and E. Oja, "Independent component analysis: Algorithms and application," *Neural Networks*, vol. 13, pp. 411–30, 2000.



- [151] T.-W. Lee, *Independent component analysis: Theory and applications*. Boston, Mass: Kluwer Academic Publishers, 1998.
- [152] S. Mika, B. Scholkopf, A. Smola, K. R. Müller, M. Scholz, and G. Rtsch, "Kernel PCA and de-noising in feature spaces," *Advances in Neural Information Processing Systems*, vol. 11, pp. 536–42, 1999.
- [153] J. B. Tenenbaum, V. De Silva, and J. C. Langford, "A global geometric framework for nonlinear dimensionality reduction," *Science*, vol. 290, pp. 2319–23, 2000.
- [154] S. T. Roweis and L. K. Saul, "Nonlinear dimensionality reduction by locally linear embedding," *Science*, vol. 290, pp. 2323–6, 2000.
- [155] J. Ashburner and S. Klöppel, "Multivariate models of inter-subject anatomical variability," *Neuroimage*, vol. 56, pp. 422–39, 2011.
- [156] A. M. Martinez and A. C. Kak, "PCA versus LDA," *IEEE Transactions on Pattern Analysis and Machine Intelligence*, vol. 23, pp. 228–33, 2001.
- [157] F. R. Bach and M. I. Jordan, "A probabilistic interpretation of canonical correlation analysis," *Technical Report. Department of Statistics, University of California, Berkeley, CA*, vol. 688, 2005.
- [158] K. J. Worsley, J. E. Taylor, F. Tomaiuolo, and J. Lerch, "Unified univariate and multivariate random field theory," *Neuroimage*, vol. 23, pp. S189–95, 2004.
- [159] R. O. Duda, P. E. Hart, and D. G. Stork, *Pattern Classification*. Wiley, New York, 1996.
- [160] C. M. Bishop, *Pattern Recognition and Machine Learning*. Springer, New York, 2006.
- [161] T. M. Mitchell, R. Hutchinson, R. S. Niculescu, F. Pereira, X. Wang, M. Just, and S. Newman, "Learning to decode cognitive states from brain images," *Machine Learning*, vol. 570, pp. 145–75, 2004.
- [162] F. Pereira, T. Mitchell, and M. Botvinick, "Machine learning classifiers and fMRI: a tutorial overview," *Neuroimage*, vol. 450, pp. 199–209, 2009.
- [163] B. E. Boser, I. M. Guyon, and V. N. Vapnik, "A training algorithm for optimal margin classifiers," in *Proc. Annual Workshop on Computational Learning Theory (WCLT)*, ACM, pp. 144–52, 1992.
- [164] N. Cristianini and J. Shawe-Taylor, *An Introduction to Support Vector Machines: and Other Kernel-Based Learning Methods*. Cambridge University Press, 2000.
- [165] B. Schölkopf and A. J. Smola, *Learning with Kernels: Support Vector Machines, Regularization, Optimization, and Beyond*. MIT Press, 2000.
- [166] P. Golland, "Discriminative direction for kernel classifiers," *Advances in Neural Information Processing Systems*, vol. 1, pp. 745–52, 2002.
- [167] P. Golland, W. E. L. Grimson, M. E. Shenton, and R. Kikinis, "Detection and analysis of statistical differences in anatomical shape," *Medical Image Analysis*, vol. 90, pp. 68–86, 2005.
- [168] B. Gaonkar, K. Pohl, and C. Davatzikos, "Pattern based morphometry," in *Proc. International Conference on Medical Image Computing and Computer Assisted Intervention (MICCAI), LNCS vol. 6892*, pp. 459–66, 2011.
- [169] C. Stellbrink, O. A. Breithardt, A. M. Sinha, and P. Hanrath, "How to discriminate responders from non-responders to cardiac resynchronization therapy," *European Heart Journal Supplements*, vol. 6, pp. 101–5, 2004.
- [170] J. J. Bax, G. Ansalone, O. A. Breithardt, G. Derumeaux, C. Leclercq, M. J. Schalij, P. Søgaard, M. St John Sutton, and P. Nihoyannopoulos, "Echocardiographic evaluation of cardiac resynchronization therapy: ready for routine clinical use?: A critical appraisal," *Journal of the American College of Cardiology*, vol. 44, pp. 1–9, 2004.
- [171] V. Delgado, C. Ypenburg, R. J. Van Bommel, L. F. Tops, S. A. Mollema, N. A. Marsan, G. B. Bleeker, M. J. Schalij, and J. J. Bax, "Assessment of left ventricular dyssynchrony by speckle tracking strain imaging: Comparison between longitudinal, circumferential, and radial strain in cardiac resynchronization therapy," *Journal of the American College of Cardiology*, vol. 51, pp. 1944–52, 2008.
- [172] C. Sonne, L. Sugeng, M. Takeuchi, L. Weinert, R. Childers, N. Watanabe, K. Yoshida, V. Mor-Avi, and R. M. Lang, "Real-time 3-Dimensional echocardiographic assessment of left ventricular dyssynchrony: Pitfalls in patients with dilated cardiomyopathy," *Journal of the American College of Cardiology - Cardiovascular Imaging*, vol. 2, pp. 802–12, 2009.
- [173] A. K. Rutz, R. Manka, S. Kozerke, S. Roas, P. Boesiger, and J. Schwitler, "Left ventricular dyssynchrony in patients with left bundle branch block and patients after myocardial infarction: integration of mechanics and viability by cardiac magnetic resonance," *European Heart Journal*, vol. 30, pp. 2117–27, 2009.

- [174] R. Chandrashekhara, R. Mohiaddin, and D. Rueckert, "Analysis of 3-D myocardial motion in tagged MR images using nonrigid image registration," *IEEE Transactions on Medical Imaging*, vol. 23, pp. 1245–50, 2004.
- [175] C. Petitjean, N. Rougon, P. Cluzel, F. Prêteux, and P. Grenier, "Quantification of myocardial function using tagged-MR and cine-MR images," *International Journal of Cardiovascular Imaging*, vol. 20, pp. 497–508, 2004.
- [176] M. De Craene, O. Camara, B. H. Bijnens, and A. F. Frangi, "Large diffeomorphic FFD registration for motion and strain quantification from 3D-US sequences," in *Proc. International Conference on Functional Imaging and Modeling of the Heart (FIMH)*, LNCS vol. 5528, pp. 437–46, 2009.
- [177] D. Perperidis, R. H. Mohiaddin, and D. Rueckert, "Spatio-temporal free-form registration of cardiac MR image sequences," *Medical Image Analysis*, vol. 9, pp. 441–56, 2005.
- [178] J.-M. Peyrat, H. Delingette, M. Sermesant, C. Xu, and N. Ayache, "Registration of 4D cardiac CT sequences under trajectory constraints with multichannel diffeomorphic demons," *IEEE Transactions on Medical Imaging*, vol. 29, pp. 1351–68, 2010.
- [179] N. Duchateau, M. De Craene, E. Silva, M. Sitges, B. H. Bijnens, and A. F. Frangi, "Septal flash assessment on CRT candidates based on statistical atlases of motion," in *Proc. International Conference on Medical Image Computing and Computer Assisted Intervention (MICCAI)*, LNCS vol. 5762, pp. 759–66, 2009.
- [180] R. H. Byrd, P. Lu, J. Nocedal, and C. Zhu, "A limited memory algorithm for bound constrained optimization," *SIAM Journal on Scientific Computing*, vol. 16, pp. 1190–208, 1995.
- [181] A. Guimond, J. Meunier, and J. P. Thirion, "Average brain models: A convergence study," *Computer Vision and Image Understanding*, vol. 77, pp. 192–210, 2000.
- [182] O. Commowick and S. K. Warfield, "A continuous STAPLE for scalar, vector, and tensor images: An application to DTI analysis," *IEEE Transactions on Medical Imaging*, vol. 28, pp. 838–46, 2009.
- [183] D. Rueckert, A. F. Frangi, and J. A. Schnabel, "Automatic construction of 3D statistical deformation models using non-rigid registration," *IEEE Transactions on Medical Imaging*, vol. 22, pp. 1014–25, 2003.
- [184] C. Hoogendoorn, T. Whitmarsh, N. Duchateau, F. M. Sukno, M. De Craene, and A. F. Frangi, "A groupwise mutual information metric for cost efficient selection of a suitable reference in cardiac computational atlas construction," in *Proc. SPIE International Conference on Medical Imaging*, p. 76231R, 2010.
- [185] L. W. Tu, *An Introduction to Manifolds*, ch. 14. Springer, 2007.
- [186] H. Hotelling, "The generalization of Student's ratio," *The Annals of Mathematical Statistics*, vol. 2, no. 3, pp. 360–78, 1931.
- [187] H. Feigenbaum, *Echocardiography*, ch. Echocardiographic measurements and normal values, pp. 658–95. Philadelphia: Lea and Febiger, 1994.
- [188] S. S. Shapiro and M. B. Wilk, "An analysis of variance test for normality (complete samples)," *Biometrika*, vol. 52, pp. 591–611, 1965.
- [189] H. Lilliefors, "On the Kolmogorov-Smirnov test for normality with mean and variance unknown," *Journal of the American Statistical Association*, vol. 62, pp. 399–402, 1967.
- [190] O. Camara, S. Oeltze, M. De Craene, R. Sebastian, E. Silva, D. Tamborero, L. Mont, M. Sitges, B. H. Bijnens, and A. F. Frangi, "Cardiac motion estimation from intracardiac electrical mapping data: Identifying a septal flash in heart failure," in *Proc. International Conference on Functional Imaging and Modeling of the Heart*, LNCS vol. 5528, pp. 21–9, 2009.
- [191] B. H. Bijnens, M. Cikes, P. Claus, and G. R. Sutherland, "Velocity and deformation imaging for the assessment of myocardial dysfunction," *European Journal of Echocardiography*, vol. 10, pp. 216–26, 2009.
- [192] O. I. I. Soliman, M. L. Geleijnse, D. A. M. J. Theuns, B. M. van Dalen, W. B. Vletter, L. J. Jordaens, A. K. Metawei, A. M. Al-Amin, and F. J. ten Cate, "Usefulness of left ventricular systolic dyssynchrony by real-time three-dimensional echocardiography to predict long-term response to cardiac resynchronization therapy," *American Journal of Cardiology*, vol. 103, pp. 1586–91, 2009.
- [193] B. Bijnens, P. Claus, C. Parsai, F. Weidemann, A. Marciniak, L. Anderson, and G. R. Sutherland, *Assessing cardiac function in dilated and failing hearts. In Doppler Myocardial Imaging, a textbook. Eds. G. R. Sutherland, L. Hatle, P. Claus, J. D'hooge and B. Bijnens*, ch. 11. BSWK, Hasselt, Belgium, 2006.

- [194] I. G. McDonald, "Echocardiographic demonstration of abnormal motion of the interventricular septum in left bundle branch block," *Circulation*, vol. 48, pp. 272–80, 1973.
- [195] J. C. Dillon, S. Chang, and H. Feigenbaum, "Echocardiographic manifestations of left-bundle branch-Block," *Circulation*, vol. 49, pp. 876–80, 1974.
- [196] W. C. Little, R. C. Reeves, J. Arciniegas, R. E. Katholi, and E. W. Rogers, "Mechanism of abnormal inter-ventricular septal motion during delayed left-ventricular activation," *Circulation*, vol. 65, pp. 1486–91, 1982.
- [197] C. L. Grines, T. M. Bashore, H. Boudoulas, S. Olson, P. Shafer, and C. F. Wooley, "Functional abnormalities in isolated left bundle branch block. the effect of interventricular asynchrony," *Circulation*, vol. 79, pp. 845–53, 1989.
- [198] S. G. Duckett, O. Camara, M. R. Ginks, J. Bostock, P. Chinchapatnam, M. Sermesant, A. Pashaei, P. D. Lambiase, J. S. Gill, G. S. Carr-White, A. F. Frangi, R. Razavi, B. H. Bijnens, and C. A. Rinaldi, "Relationship between endocardial activation sequences defined by high-density mapping to early septal contraction (septal flash) in patients with left bundle branch block undergoing cardiac resynchronization therapy," *Europace*, vol. 14, no. 1, pp. 99–106, 2012.
- [199] O. Gjesdal, E. W. Remme, A. Opdahl, H. Skulstad, K. Russell, E. Kongsgaard, T. Edvardsen, and O. A. Smiseth, "Mechanisms of abnormal systolic motion of the interventricular septum during left bundle-branch block," *Circulation Cardiovascular Imaging*, vol. 4, no. 3, pp. 264–73, 2011.
- [200] P. Lim, C. Bars, L. Mitchell-Heggs, C. Roiron, N. Elbaz, B. Hamdaoui, N. Lellouche, J.-L. Dubois-Randé, and P. Guéret, "Importance of contractile reserve for CRT," *Europace*, vol. 9, pp. 739–43, 2007.
- [201] J. M. Tolosana, A. Hernandez Madrid, J. Brugada, M. Sitges, I. Garcia Bolao, I. Fernandez Lozano, J. M. Ferrer, A. Quesada, A. Macias, W. Marin, J. M. Escudier, A. Alonso Gomez, M. Gimenez Alcala, D. Tamborero, A. Berruezo, L. Mont, and on behalf of the SPARE Investigators, "Comparison of benefits and mortality in cardiac resynchronization therapy in patients with atrial fibrillation versus patients in sinus rhythm (results of the Spanish Atrial Fibrillation and Resynchronization [SPARE] study)," *The American Journal of Cardiology*, vol. 102, pp. 444–9, 2008.
- [202] P. J. Cowburn and C. Leclercq, "How to improve outcomes with cardiac resynchronisation therapy: importance of lead positioning," *Heart Failure Reviews*, 2011. In press.
- [203] B. Vidal, V. Delgado, L. Mont, S. Poyatos, E. Silva, M. A. Castel, J. M. Tolosana, A. Berruezo, J. Brugada, and M. Sitges, "Decreased likelihood of response to cardiac resynchronization in patients with severe heart failure," *European Journal of Heart Failure*, vol. 12, pp. 283–7, 2010.
- [204] N. Duchateau, M. De Craene, G. Piella, and A. F. Frangi, "Characterizing pathological deviations from normality using constrained manifold-learning," in *Proc. International Conference on Medical Image Computing and Computer Assisted Intervention (MICCAI), LNCS vol. 6893*, pp. 256–63, 2011.
- [205] B. K. Fornwalt, W. W. Sprague, P. BeDell, J. D. Suever, B. Gerritse, J. D. Merlino, D. A. Fyfe, A. R. León, and J. N. Oshinski, "Agreement is poor among current criteria used to define response to cardiac resynchronization therapy," *Circulation*, vol. 121, pp. 1985–91, 2010.
- [206] J. G. Cleland and S. Ghio, "The determinants of clinical outcome and clinical response to CRT are not the same," *Heart Failure Reviews*, 2011. In press.
- [207] K.-H. Kim and S. Choi, "Neighbor search with global geometry: a minimax message passing algorithm," in *Proc. International Conference on Machine Learning (ICML)*, pp. 401–8, 2007.
- [208] S. Roweis and L. Saul, "Nonlinear dimensionality reduction by locally linear embedding," *Science*, vol. 290, no. 550, pp. 2323–6, 2000.
- [209] M. Belkin and P. Niyogi, "Laplacian eigenmaps for dimensionality reduction and data representation," *Neural Computation*, vol. 15, no. 6, pp. 1373–96, 2003.
- [210] B. Schölkopf, A. Smola, and K.-R. Müller, "Nonlinear component analysis as a kernel eigenvalue problem," *Neural Computation*, vol. 10, no. 5, pp. 1299–1319, 1998.
- [211] J. T.-Y. Kwok and I. W.-H. Tsang, "The pre-image problem in kernel methods," *IEEE Transactions on Neural Networks*, vol. 15, pp. 1517–25, 2004.
- [212] W. S. Zheng, J.-H. Lai, and P. C. Yuen, "Penalized preimage learning in kernel principal component analysis," *IEEE Transactions on Neural Networks*, vol. 21, pp. 551–70, 2010.
- [213] T. Hastie and W. Stuetzle, "Principal curves," *Journal of the American Statistical Association*, vol. 84, no. 406, pp. 502–16, 1989.

- [214] S. Gerber, T. Tasdizen, and R. Whitaker, "Dimensionality reduction and principal surfaces via kernel map manifolds," in *Proc. IEEE International Conference on Computer Vision*, pp. 529–36, 2009.
- [215] Y. Bengio, J.-F. Paiement, P. Vincent, O. Delalleau, N. Le Roux, and M. Ouimet, "Out-of-sample extensions for LLE, isomap, MDS, eigenmaps, and spectral clustering," *Advances in Neural Information Processing Systems*, vol. 16, pp. 177–84, 2004.
- [216] P. Meinicke, S. Klanke, R. Memisevic, and H. Ritter, "Principal curves from unsupervised kernel regression," *IEEE Transactions on Pattern Analysis and Machine Intelligence*, vol. 27, no. 9, pp. 1379–91, 2005.
- [217] S. Gerber, T. Tasdizen, P. T. Fletcher, S. Joshi, and R. Whitaker, "Manifold modeling for brain population analysis," *Medical Image Analysis*, vol. 14, pp. 643–53, 2010.
- [218] P. Etyngier, R. Keriven, and F. Segonne, "Projection onto a shape manifold for image segmentation with prior," in *Proc. IEEE International Conference on Image Processing (ICIP)*, pp. IV361–4, 2007.
- [219] N. Aronszajn, "Theory of reproducing kernels," *Transactions of the American Mathematical Society*, vol. 68, no. 3, pp. 337–404, 1950.
- [220] D. W. Scott, *Multivariate density estimation: theory, practice, and visualization (Wiley Series in Probability and Statistics)*. Wiley, 1992.
- [221] B. W. Silverman, *Density estimation for statistics and data analysis (Chapman & Hall / CRC Monographs on Statistics & Applied Probability)*. Chapman and Hall / CRC, 1986.
- [222] Z. Zhang, J. Wang, and H. Zha, "Adaptive manifold learning," *IEEE Transactions on Pattern Analysis and Machine Intelligence*, vol. 34, no. 2, pp. 253–65, 2012.
- [223] R. H. Davies, C. J. Twining, T. F. Cootes, and C. J. Taylor, "Building 3-D statistical shape models by direct optimization," *IEEE Transactions on Medical Imaging*, vol. 29, pp. 961–81, 2010.
- [224] J. B. Tenenbaum and J. C. Langford, "Response to letter "The Isomap Algorithm and Topological Stability" from Balasubramanian, M. and Schwartz, E.L.," *Science*, vol. 295, p. 7, 2002.
- [225] H. Choi and S. Choi, "Robust kernel isomap," *Pattern Recognition*, vol. 40, pp. 853–62, 2007.
- [226] F. Camastra, "Data dimensionality estimation methods: A survey," *Pattern Recognition*, vol. 36, pp. 2945–54, 2003.
- [227] F. Z. Khan, M. S. Virdee, P. A. Read, P. J. Pugh, D. O'Halloran, M. Fahey, M. Elsik, D. Begley, S. P. Fynn, and D. P. Dutka, "Effect of low-amplitude two-dimensional radial strain at left ventricular pacing sites on response to cardiac resynchronization therapy," *Journal of the American Society of Echocardiography*, vol. 23, pp. 1168–76, 2010.
- [228] M. De Craene, N. Duchateau, C. Tobon-Gomez, B. Ghafaryasl, G. Piella, K. S. Rhode, and A. F. Frangi, "SPM to the heart: Mapping of 4D continuous velocities for motion abnormality quantification," in *Proceedings IEEE International Symposium on Biomedical Imaging*, 2012. In press.
- [229] R. R. Coifman and S. Lafon, "Geometric harmonics: A novel tool for multiscale out-of-sample extension of empirical functions," *Applied and Computational Harmonic Analysis*, vol. 21, no. 1, pp. 31–52, 2006.
- [230] C. Tobon-Gomez, M. De Craene, A. Dahl, S. Kapetanakis, G. Carr-White, A. Lutz, V. Rasche, P. Etyngier, S. Kozerke, T. Schaffeter, C. Riccobene, Y. Martelli, O. Camara, A. F. Frangi, and K. S. Rhode, "A multimodal database for the first cardiac motion analysis challenge," in *Proc. Statistical Atlases and Computational Models of the Heart (STACOM), MICCAI'11 Workshop*, pp. 228–36, 2011.

---

## Institutional context

*Academic context.* This research work has been led within the Research Center for Computational Imaging and Simulation Technologies in Biomedicine (CISTIB)<sup>1</sup>, at the Department of Information and Communication Technologies (DTIC) at the Universitat Pompeu Fabra (UPF), Barcelona, Spain<sup>2</sup>. This group mainly focuses on computational analysis of medical images and cardiovascular system simulations, for applications in cardiology, angiology and osteopathy. It is currently directed by Prof. Alejandro F. Frangi. The thesis formed part of the image registration team at CISTIB, and was associated with the work of Dr. Gemma Piella and Dr. Mathieu De Craene.

Preliminary stages of this work were done as MSc internship within this research group, for the scholar year 2007-2008, as part of the “Mathématiques, Vision et Apprentissage” (MVA - Mathematics, Vision and Machine-learning) MSc cursus from the Ecole Normale Supérieure (ENS), Cachan, France<sup>3</sup>.

*Research projects.* The research work contributed to several multi-annual projects in the coordination of which the CISTIB research group is involved. Said projects are briefly listed below:

- **euHeart**

(Personalized & Integrated Cardiac Care: Patient-specific Cardiovascular Modelling and Simulation for In Silico Disease), supported by the European Union as part of FP7 package. FP7-ICT-2007-224495. 2008-2012.

- **cvREMOD**

(Convergencia de Tecnologías Médicas para la Gestión Integral del Remodelado Cardiovascular), supported by a CENIT grant from the Spanish Ministry of Industry, Tourism and Commerce. CEN-20091044. 2009-2012.

- **STIMATH**

(Análisis de imágenes de alto rendimiento mediante modelos estadísticos de forma, apariencia y deformación), supported by the Spanish Ministry of Science and Innovation, Plan E and FEDER. TIN2009-14536-C02-01. 2010-2013.

- **CDTeam**

---

<sup>1</sup><http://www.cistib.upf.edu/>

<sup>2</sup><http://www.upf.edu/dtic/>

<sup>3</sup><http://www.math.ens-cachan.fr/version-francaise/formations/master-mva/>

(Consortium para el Desarrollo de Tecnología Avanzada de imagen Médica), supported by a CENIT grant from the Spanish Ministry of Industry, Tourism and Commerce. 2006-2009.

*Clinical collaborations.* Access to clinical data and experience was guaranteed by the close collaboration with clinical partners of the research group. Specific steps of this work included collaborations with clinical practitioners (Dr. Marta Sitges, Dr. Adelina Doltra and Dr. Etelvino Silva, from the Hospital Clínic; Institut d'investigacions Biomèdiques August Pi i Sunyer; Universitat de Barcelona, Spain), and external researchers (Prof. Bart H. Bijnens, from the Institució Catalana de Recerca i Estudis Avançats; Universitat Pompeu Fabra, Barcelona, Spain).

---

# Publications

## *International Journal*

1. **N. Duchateau**, M. De Craene, G. Piella, E. Silva, A. Doltra, M. Sitges, B. H. Bijnens, and A. F. Frangi. A Spatiotemporal Statistical Atlas of Motion for the Quantification of Abnormalities in Myocardial Tissue Velocities. *Medical Image Analysis*, 15(3):316-28, 2011.
2. M. De Craene, G. Piella, O. Camara, **N. Duchateau**, E. Silva, A. Doltra, J. D'hooge, J. Brugada, M. Sitges, A. F. Frangi. Spatiotemporal Diffeomorphic Free-Form Deformation: Application to Motion and Strain Estimation from 3D Echocardiography. *Medical Image Analysis*, 16(2):427-50, 2012.
3. **N. Duchateau**, A. Doltra, E. Silva, M. De Craene, G. Piella, M. A. Castel, L. Mont, J. Brugada, A. F. Frangi, M. Sitges. Atlas-based Quantification of Myocardial Motion Abnormalities for the Understanding of Cardiac Resynchronization Therapy Outcome. 2012. Under review.
4. **N. Duchateau**, M. De Craene, G. Piella, A. F. Frangi. Constrained Manifold Learning for the Characterization of Pathological Deviations from Normality. 2012. Under review.
5. C. Hoogendoorn, **N. Duchateau**, D. Sanchez-Quintana, T. Whitmarsh, F. Sukno, M. De Craene, K. Lekadir, A. F. Frangi. A High-Resolution Atlas and Statistical Model of the Human Heart from Multislice CT. 2012. Under review.
6. C. Tobon-Gomez, **N. Duchateau**, R. Sebastian, S. Marchesseau, E. Donal, M. De Craene, A. Pashaei, J. Relan, M. Steghöfer, P. Lamata, O. Camara, H. Delingette, S. Duckett, M. Garreau, A. Hernandez, K. S. Rhode, M. Sermesant, N. Ayache, C. Leclercq, R. Razavi, N. Smith, A. F. Frangi. Cardiac Resynchronization Therapy Planning Platform. 2012. Under review.

## *Peer-reviewed International Conference*

1. **N. Duchateau**, M. D. Craene, E. Silva, M. Sitges, B. Bijnens, A. Frangi. Septal Flash Assessment on CRT Candidates based on Statistical Atlases of Motion. *Proc. International Conference on Medical Image Computing and Computer Assisted Intervention (MICCAI), LNCS*, 5762:759-66, 2009.
2. C. Hoogendoorn, T. Whitmarsh, **N. Duchateau**, F. M. Sukno, M. D. Craene, A. F. Frangi. A groupwise mutual information metric for cost efficient selection of a suitable reference in cardiac computational atlas construction. *Proc. SPIE Conference on Medical Imaging*, 76231R, 2010.
3. **N. Duchateau**, M. De Craene, G. Piella, C. Hoogendoorn, E. Silva, A. Doltra, L. Mont, M. A. Castel, J. Brugada, M. Sitges, A. F. Frangi. Atlas-based Quantification of myocardial motion abnormalities: Added-value for the understanding of CRT outcome? *Proc. Statistical Atlases and Computational Models of the Heart (STACOM), MICCAI'10 Workshop, LNCS*, 6364:65-74, 2010.
4. M. De Craene, F. M. Sukno, C. Tobon-Gomez, C. Butakoff, R. M. Figueras i Ventura, C. Hoogendoorn, G. Piella, **N. Duchateau**, E. Muoz-Moreno, R. Sebastin, O. Camara, A. F. Frangi. Atlas construction and image analysis using statistical cardiac models. *Proc. Statistical Atlases and Computational Models of the Heart (STACOM), MICCAI'10 Workshop, LNCS*, 6364:1-13, 2010. Invited talk.
5. M. De Craene, G. Piella, **N. Duchateau**, E. Silva, A. Doltra, J. D'Hooge, O. Camara, M. Sitges, A. F. Frangi. Temporal diffeomorphic free-form deformation for strain quantification in 3D-US images. *Proc. International Conference on Medical Image Computing and Computer Assisted Intervention (MICCAI), LNCS*, 6362:1-8, 2010.
6. **N. Duchateau**, M. De Craene, G. Piella, and A. F. Frangi. Characterizing Pathological Deviations from Normality using Constrained Manifold-Learning. *Proc. International Conference on Medical Image Computing and Computer Assisted Intervention (MICCAI), LNCS*, 6893:256-63, 2011.

7. M. De Craene, C. Tobon-Gomez, C. Butakoff, **N. Duchateau**, G. Piella, K. S. Rhode and A. F. Frangi. Temporal diffeomorphic Free Form Deformation (TDFFD) applied to motion and deformation quantification of tagged MRI sequences. *Proc. Statistical Atlases and Computational Models of the Heart (STACOM), MICCAI'11 Workshop, LNCS*, 7085:68-77, 2012.
8. M. De Craene, **N. Duchateau**, C. Tobon-Gomez, B. Ghafaryasl, G. Piella, K. S. Rhode, A. F. Frangi. SPM to the heart: Mapping of 4D continuous velocities for motion abnormality quantification. *Proc. IEEE International Symposium on Biomedical Imaging (ISBI'12)*. 2012. In press.

#### *International Journal Abstract*

1. **N. Duchateau**, M. De Craene, G. Piella, E. Silva, A. Doltra, M. Sitges, B. H. Bijnens, A. F. Frangi. Quantification of septal motion abnormalities in CRT candidates using a statistical atlas based-approach. *European Heart Journal, Abstracts from the European Society of Cardiology (ESC) Annual Congress*, 31(S1):875-6, 2010.
2. **N. Duchateau**, A. Doltra, E. Silva, M. De Craene, G. Piella, L. Mont, M. A. Castel, J. Brugada, M. Sitges, A. F. Frangi. Added value of a statistical atlas-based quantification of motion abnormalities for the prediction of CRT response. *European Journal of Echocardiography, Abstracts from the European Association of Echocardiography Annual Congress (EuroEcho)*, 11(S2):ii80, 2010. Young Investigators Award.

#### *International Conference Abstract*

1. **N. Duchateau**, A. Doltra, E. Silva, M. De Craene, G. Piella, L. Mont, M. A. Castel, J. Brugada, M. Sitges, A. F. Frangi. Added value of a statistical atlas-based quantification of motion abnormalities for the prediction of CRT response. *American Society of Echocardiography (ASE) Scientific Sessions*, 2011. Invited Poster.



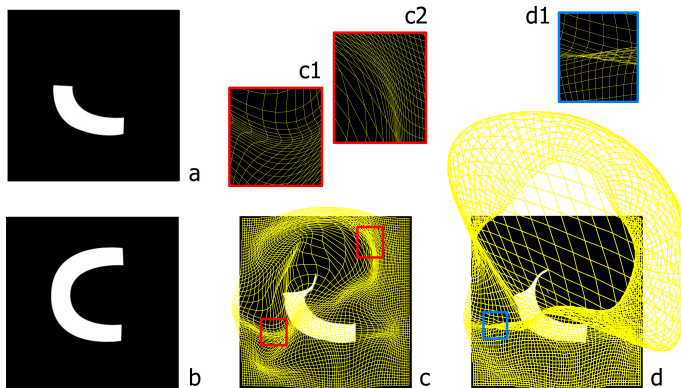
---

## Curriculum Vitae

Nicolas Duchateau received his Engineering degree in Optics from the Institut d'Optique, Palaiseau, France, in 2007, and his MSc degree in Mathematics, Vision and Machine-learning from the Ecole Normale Supérieure de Cachan, France, in 2008. He joined the Center for Computational Imaging & Simulation Technologies in Biomedicine (CISTIB) at the Universitat Pompeu Fabra (UPF), Barcelona, Spain, in 2008 as PhD student to work under the supervision of Mathieu De Craene and Alejandro Frangi. His main research interests are in the use of image registration and statistical atlases for the quantification of heart motion and deformation, part of which is summarized in this PhD thesis. He now works with the Fundació Clínic, Barcelona, Spain, within the Arrhythmia, Resynchronization and Cardiac Imaging unit, under the supervision of Dr. Marta Sitges.

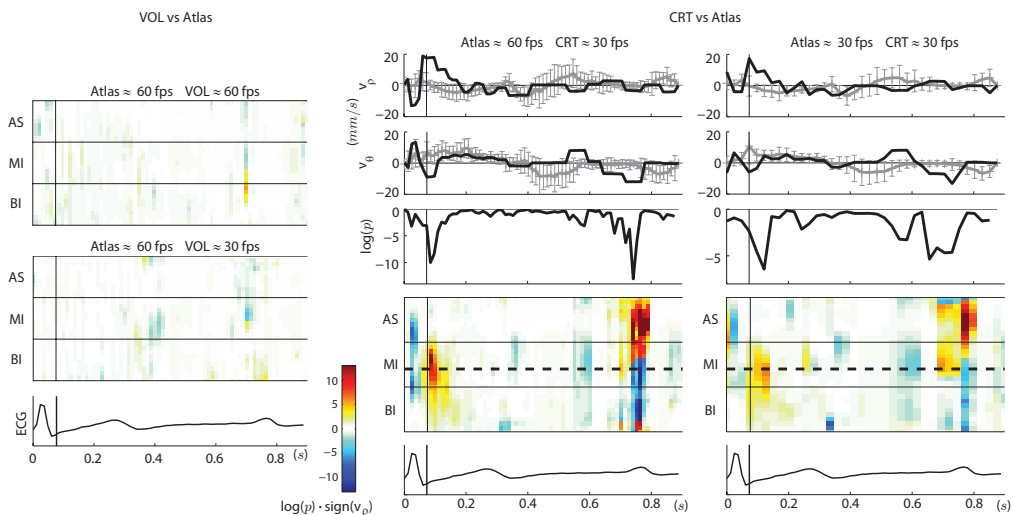
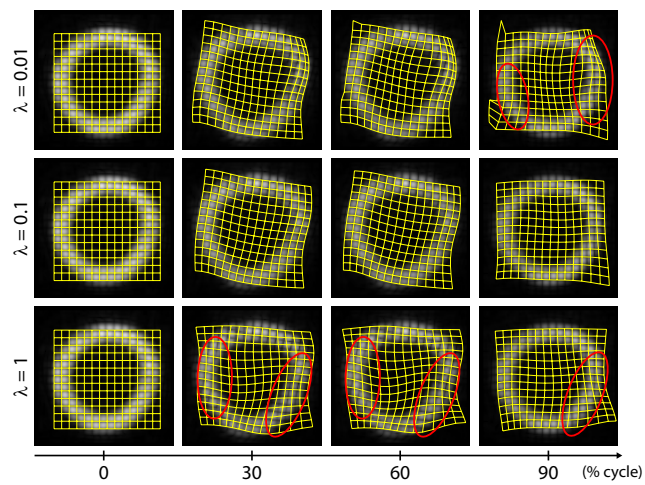




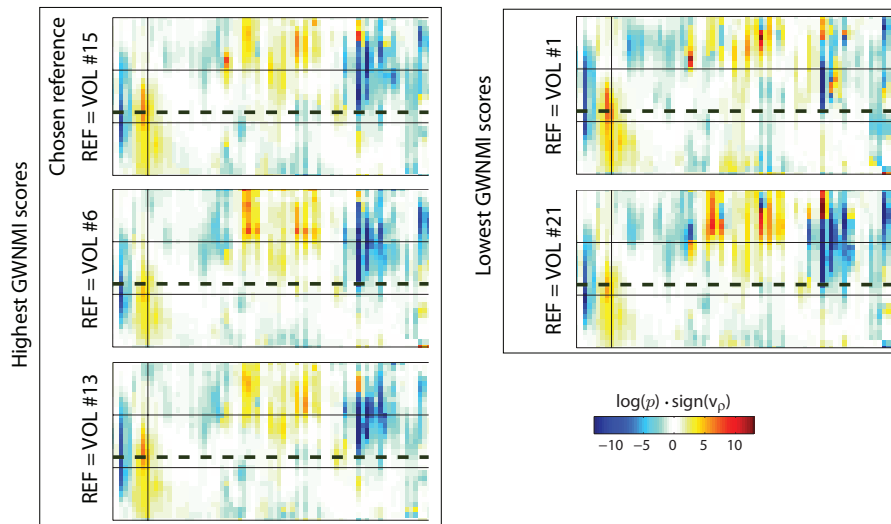


**Figure 2.1, page 10:** Illustration of folding artifacts on large transforms, with FFD as registration method. (a) fixed image, (b) moving image, (c) diffeomorphic transform, and (d) non-diffeomorphic transform.

**Figure 2.3, page 13:** Propagation of a synthetic grid using the TDDFD tracking. Results for three different weights  $\lambda$  of the image similarity metrics (comparison frame-to-frame and to the reference image). Drift errors (top row) and tag jumps (bottom row) are pointed out by the red ellipses. Image taken from [104] with the permission of the authors.

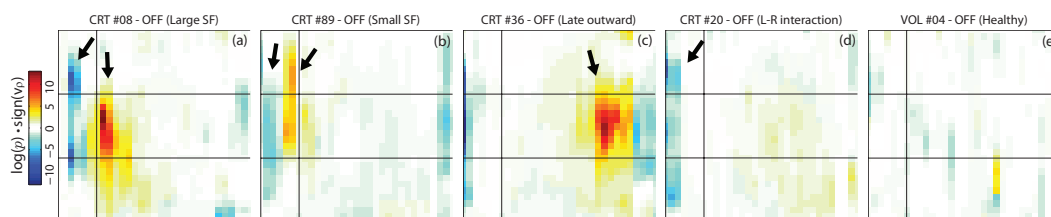
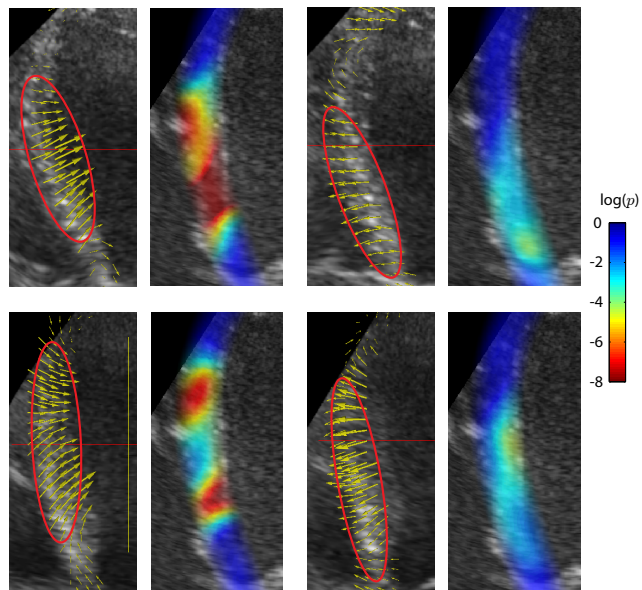


**Figure 3.9, page 31:** Left: Effect of a lower frame rate (volunteer to compare) on the  $p$ -value maps. Top: original frame rate (atlas  $\approx$  60 fps, volunteer to compare  $\approx$  60 fps). Bottom: lower volunteer frame rate ( $\approx$  30 fps). Right: Effect of a lower frame rate (atlas population) on the  $p$ -value maps. First column: original frame rate (atlas  $\approx$  60 fps, CRT candidates  $\approx$  30 fps). Second column: lower atlas frame rate (atlas and CRT candidates  $\approx$  30 fps). Vertical line indicates the end of the IVC period.

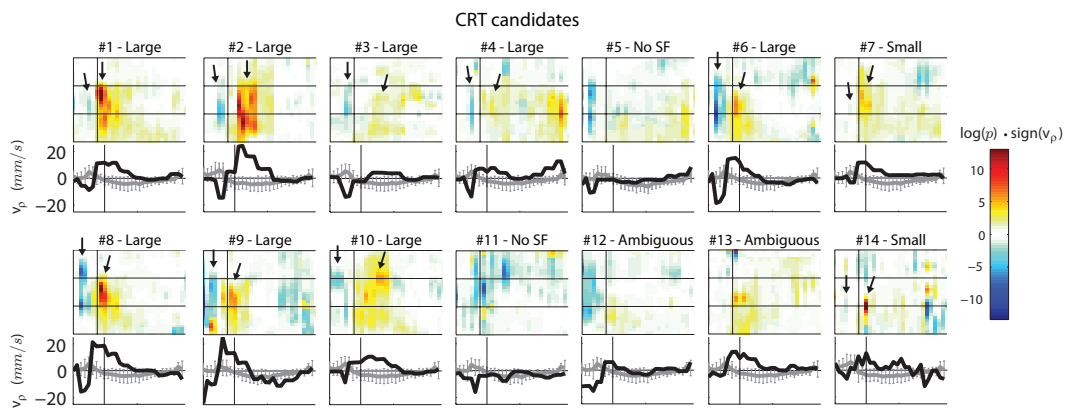


**Figure 3.10, page 33:** Influence of the reference choice on the  $p$ -value maps. VOL #15 is the reference used in the rest of the paper, VOL #6 and #1 are the subjects with the two other best GWNMI scores, and VOL #13 and #21 the subjects with the two worst ones.

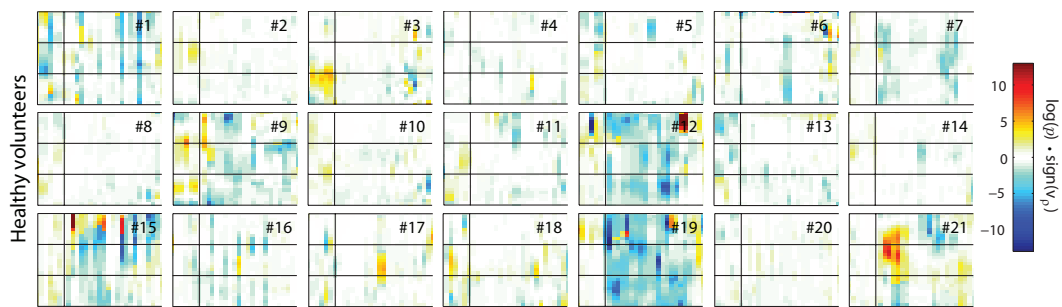
**Figure 3.12, page 35:** Comparison of two CRT candidates with SF with respect to the atlas. Spatial localization of abnormality along the septum, at inward and outward events. In contrast, the LV of healthy subjects would mainly contract in the longitudinal direction. For each block: velocity field in the anatomy of patient  $k$ , and corresponding  $p$ -value map, defined in the reference anatomy. Arrows have been scaled by a global factor for optimal visibility. Warmer colors on the  $p$ -value maps indicate regions of higher abnormality.



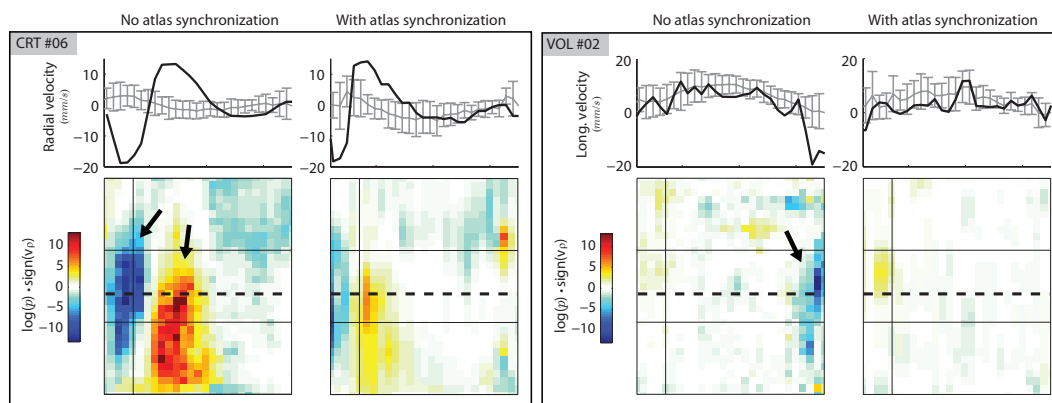
**Figure 4.2, page 45:** Variety of the patterns observed on the motion abnormality maps.



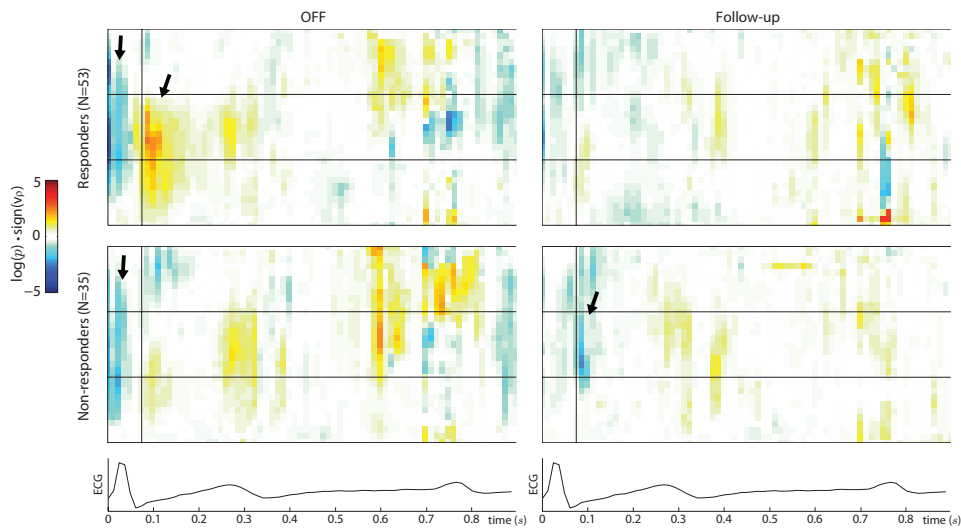
**Figure 3.14, page 37:** Motion abnormality maps and radial velocity profiles at the level of the septum with highest abnormality, during systole, for the whole set of CRT candidates. Black arrows point out the inward and outward motion during SF events, when present.



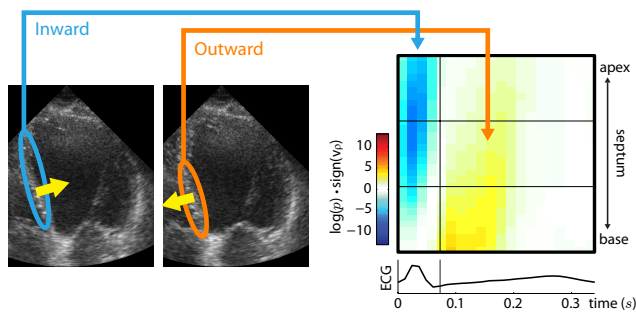
**Figure 3.15, page 38:** Motion abnormality maps during systole, for the set of volunteers.



**Figure 4.3, page 45:** Radial velocity and motion abnormality map for one patient and one healthy volunteer without and with the atlas spatiotemporal synchronization.

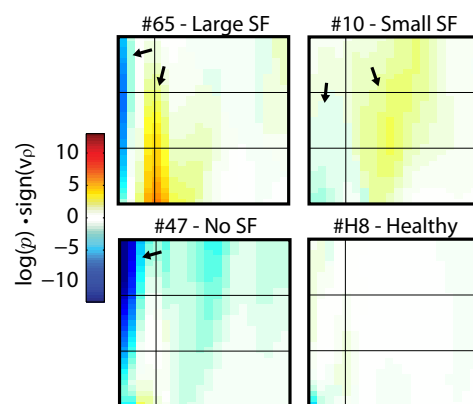


**Figure 4.4, page 46:** Average abnormality map for the set of volume responders and non-responders, at baseline and follow-up.

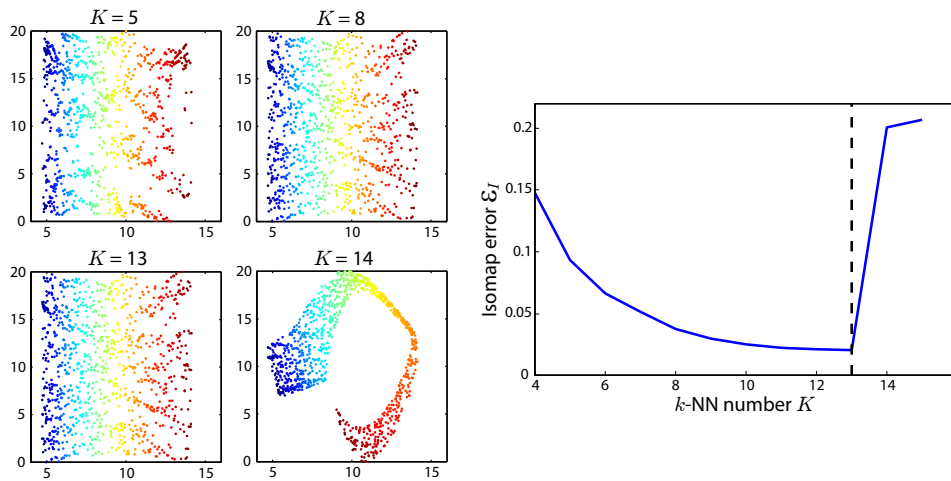
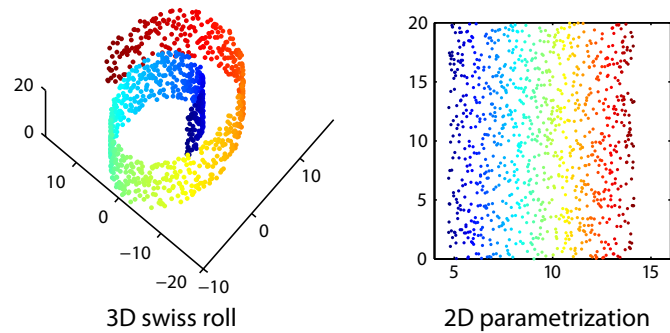


**Figure 5.3, page 56:** Map of septal motion abnormalities during systole, for one CRT candidate with SF. The color-scale encodes abnormality ( $p$ -value) in a logarithmic scale, multiplied by the sign of the radial velocity  $v_\rho$  to highlight the inward and outward events of SF.

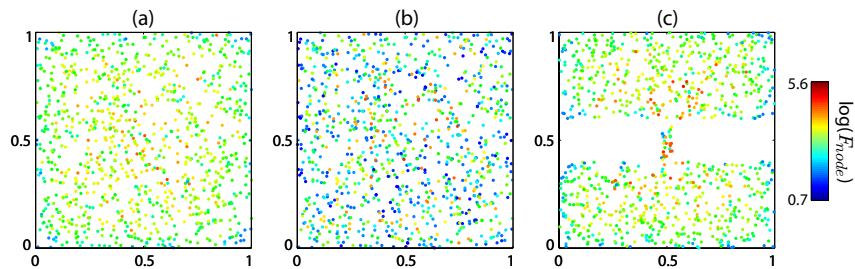
**Figure 5.4, page 56:** Abnormality maps for four different subjects: two with SF (top row, arrows indicate the inward and outward events of SF), one with left-right interaction (bottom left), a type of inter-ventricular dyssynchrony [8] where the septum moves passively inward, as indicated by the black arrow, and one healthy volunteer (bottom right).



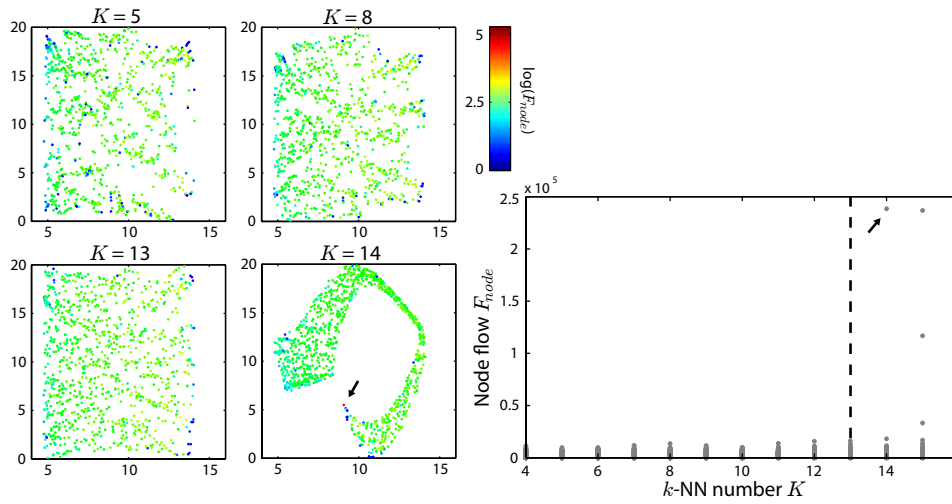
**Figure 5.7, page 63:** 3D swiss roll and 2D random distribution of points used as 2D parametrization for its construction.



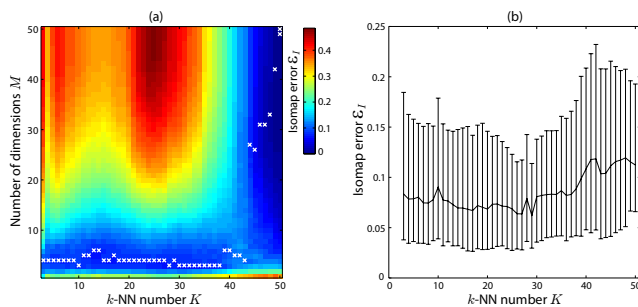
**Figure 5.8, page 64:** Influence of the number of  $k$ -NN on the isomap output, for the 3D swiss roll data. Top: isomap output for  $K = \{5, 8, 13, 14\}$ . Bottom: evolution of the isomap error  $\epsilon_I$  (Eq. 5.25) with the number of  $k$ -NN. Mean error over all the pairs  $(\mathbf{x}_i, \mathbf{x}_j) \in \mathcal{X}^2$ . A jump is present on this curve for  $K = 14$ , reflecting the apparition of a short-circuit in the  $k$ -NN graph.



**Figure 5.9, page 65:** Influence of the graph number of  $k$ -NN and the spatial arrangement of the graph nodes on the the node flow distribution. Synthetic dataset of 1000 points within a given spatial domain. (a) Initial spatial domain with  $K = 20$ . (b) Same spatial domain with  $K = 5$ . Large local variations of the node flow are locally observed, reflecting a too low connectivity within the graph. (c) Modified spatial domain with  $K = 20$ . Node flow is higher where the spatial domain is narrow, reflecting that a large number of shortest paths along the graph pass within this region.

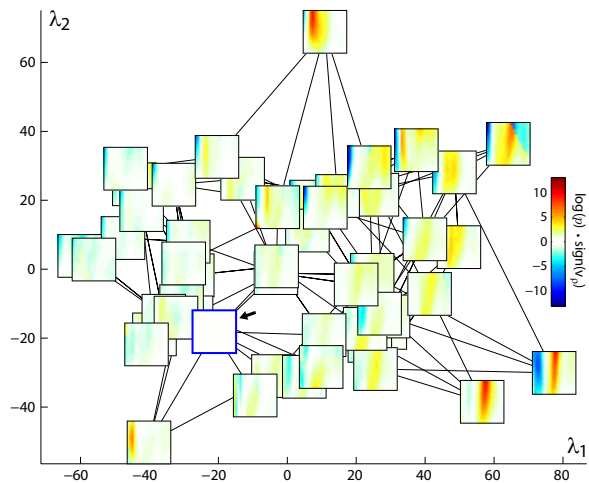


**Figure 5.10, page 65:** Influence of the number of  $k$ -NN on the node flow, for the 3D swiss roll data. Top: isomap output for  $K = \{5, 8, 13, 14\}$ , where each node is colored according to its flow (Eq. 5.26). For all points, the variability of the flow distribution is low when  $K \leq 13$ , while the apparition of a short-circuit for  $K = 14$  makes one specific point having almost the highest flow possible (black arrow). Bottom: evolution of the node flow distribution with the number of  $k$ -NN. Black arrow indicates the value of the node flow for the point where the short-circuit appears.



**Figure 5.14, page 68:** (a) Evolution of the isomap error  $\epsilon_I$  with the dimensionality  $M$  and the number of  $k$ -NN, for the training set of CRT candidates with SF. White crosses indicate the minimum value of  $\epsilon_I$  for each value of  $k$ -NN. (b) Evolution of the isomap error  $\epsilon_I$  with the number of  $k$ -NN, for  $M = 4$ .

**Figure 5.15, page 69:** 2D embedding of the manifold of SF  $p$ -value maps (output of isomap) according to its two first dimensions. The black arrow indicates the origin image used to constrain the manifold, representing a normal motion pattern.





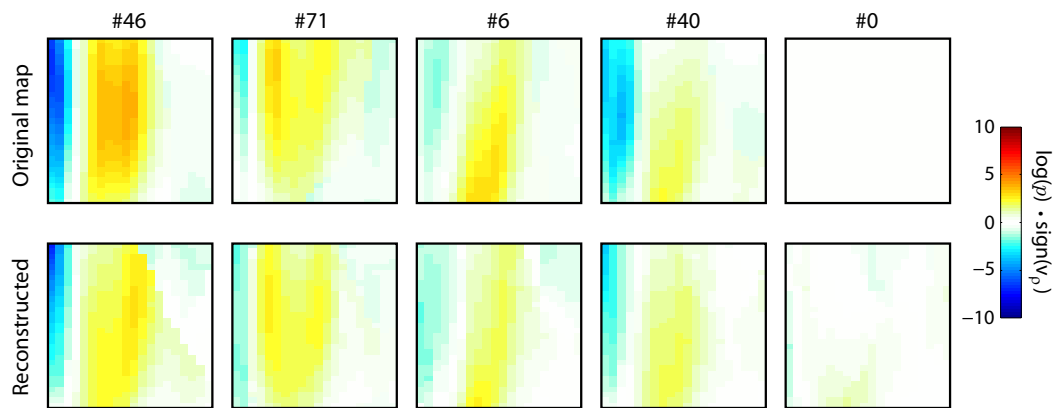


**Figure 5.18, page 71:** Reconstruction of five patients from the training set of CRT candidates with SF (using leave-one-out), for the optimal values of  $\gamma_f$  and  $\gamma_g$ .

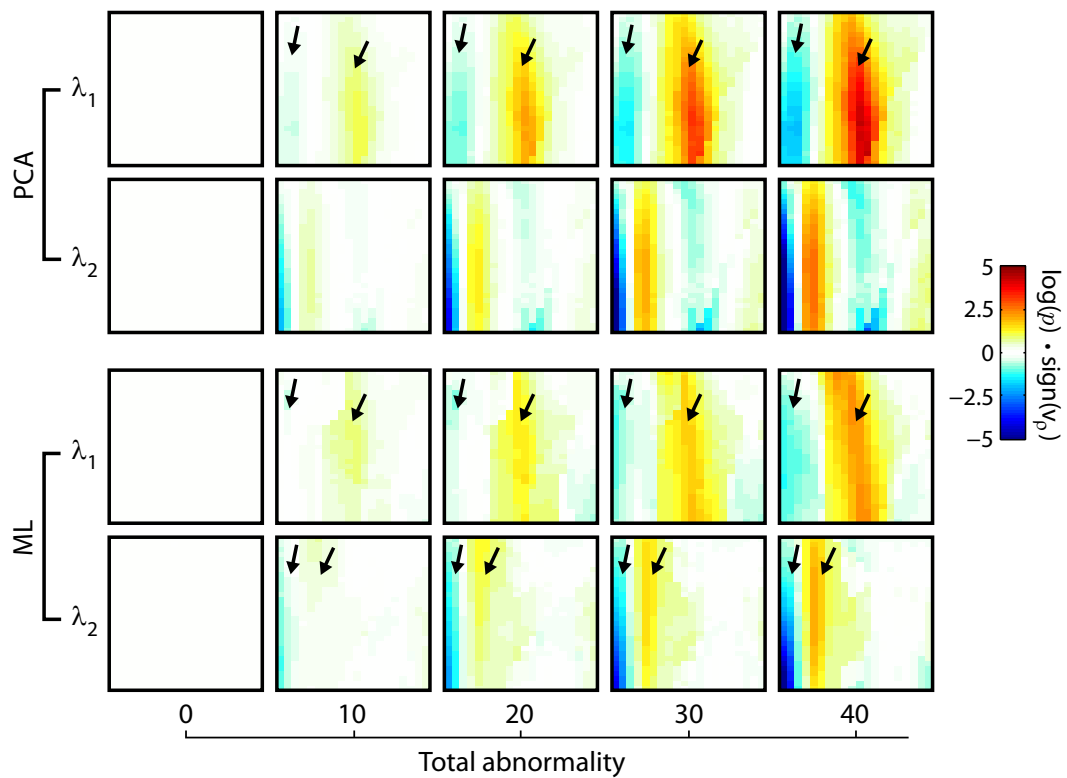


**Figure 5.22, page 74:** Progressive deviations from the map used as origin for normality  $\mathbf{I}_0$ , along the two first principal directions of the manifold dataset  $\mathcal{I}$ , obtained using either PCA or manifold learning (ML). Arrows indicate the characteristic inward and outward motion events of SF. Total abnormality is defined as  $S_{\mathcal{A}}(\mathbf{I}, \mathbf{I}_0)$  (Sec. 5.2.6).

**Figure 5.23, page 75:** Normalized evolution of the distances  $d_M$  and  $d_P$  for each subject of each tested population, versus the size of the training population (number of SF patients). Error bars represent the standard deviation over 100 random combinations of  $N_s < N$  subjects.

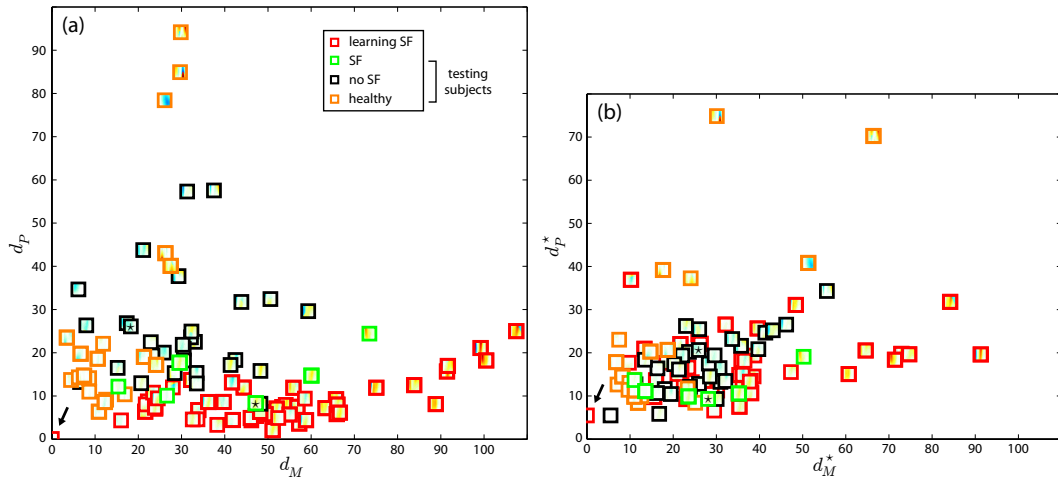
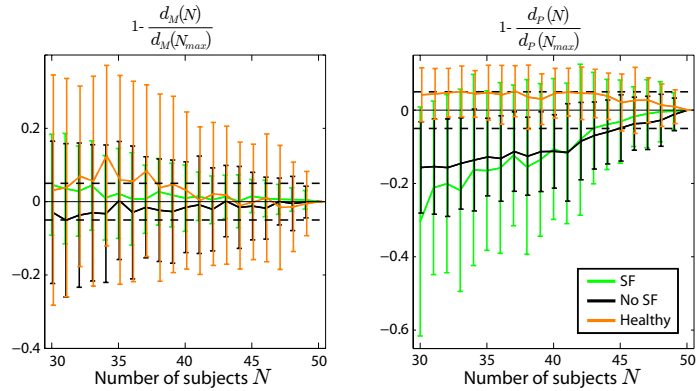


**Figure 5.24, page 76:** (a) Subject ordering according to  $d_M$  and  $d_P$  (Sec. 5.2.6), used as horizontal and vertical axis, respectively. (b) Subject ordering according to  $d_M^*$  and  $d_P^*$  (Eq. 5.29), used as horizontal and vertical axis, respectively. The black arrow indicates the image used to constrain the manifold, representing a normal motion pattern, and used as origin. Asterisk-marked miniatures refer to two subjects with the same amount of total abnormality, but belonging to different populations (cf. App. C).

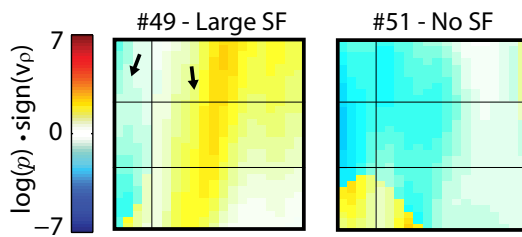


**Figure 5.27, page 82:** Example of two patients having the same amount of total abnormality  $S_A(\mathbf{I}, \mathbf{I}_0)$ , but different patterns (presence and absence of SF, respectively). These subjects are clearly discriminated by the use of the proposed distances  $d_M$  and  $d_P$  (cf. asterisks-marked miniatures on Fig. 5.24).



